Double Point Contact Single Molecule Absorption Spectroscopy

A Thesis
Presented to
The Academic Faculty

by

John Brooks Howard

In Partial Fulfillment
of the Requirements for the Degree
Doctor of Philosophy

School of Physics
Georgia Institute of Technology
December 2009

Double Point Contact Single Molecule Absorption Spectroscopy

Approved by:

Professor Mei-Yin Chou
School of Physics
Georgia Institute of Technology, Chair

Professor William D. Hunt
School of Electrical Engineering
Georgia Institute of Technology

Professor Alexei Marchenkov
School of Physics
Georgia Institute of Technology, Adviser

Professor Dragomir Davidovic
School of Physics
Georgia Institute of Technology

Professor James Gole
School of Physics
Georgia Institute of Technology

Professor Elisa Riedo
School of Physics
Georgia Institute of Technology

Date Approved: March, 29, 2006

To John and Linda Howard,

my parents,

for making me stick with school in '94.

ACKNOWLEDGEMENTS

First I want to thank the most patient thesis advisor to ever walk this earth, Professor Alexei Marchenkov, for dealing with my less than stellar work ethic. Without his unconditional motivation I never would have finished. My admiration for him is rivaled only by that which I have for our graduate coordinator, Professor Andrew Zangwill. He not only pointed me to Professor Marchenkov's group, but also made electricity and magnetism come alive. My most heart felt thanks is extended to these men.

I thank every one who passed through our group (Sang, Bret, Ting, Josh, Brandon, Sanjay, and Dan) for keeping the day-to-day grind of being a graduate student interesting to say the least. I wish them all the best in their future endeavors.

To those who were not a part of our research group but nevertheless played an important part in my stay at Georgia Tech (James, Kristin, Alexis, Pat, Radford, Joanna and Soo) I extend a warm thank you. They helped me keep my sanity while trying to claw my way out of one of the many holes that I dug for myself. If they utilize just a fraction of the talent that they have, their futures will be as bright as something (I'm at a loss for a simile).

As I correct all of the grammatical errors throughout this thesis, I would be remiss if I did not thank Judy Melton for the painstaking work of proofreading each chapter (I never knew equations needed punctuation at the end of them). Last, but certainly not least, my music buddy Kevin, thanks for the lessons on gospel music, and don't think I don't remember that you still have my Aretha Franklin CD.

TABLE OF CONTENTS

LIST OF FIGURES

SUMMARY

Our primary objective with the presentation of this thesis is to utilize superconducting transport through microscopic objects to both excite and analyze the vibrational degrees of freedom of various molecules of a biological nature. The technique stems from a Josephson junction's ability to generate radiation that falls in the terahertz gap (≈ 10 THz) and consequently can be used to excite vibrational modes of simple and complex molecules. Analysis of the change in IV characteristics coupled with the differential conductance ($\frac{dI}{dV}$) allows determination of both the absorption spectra and the vibrational modes of biological molecules.

Presented here are both the theoretical foundations of superconductivity relevant to our experimental technique and the fabrication process of our samples. Comparisons between our technique and that of other absorption spectroscopy techniques are included as a means of providing a reference upon which to judge the merits of our novel procedure. This technique is meant to improve not only our understanding of the vibrational degrees of freedom of useful biological molecules, but also these molecule's structural, electronic and mechanical properties.

CHAPTER I

SUPERCONDUCTIVITY IN NANOWIRES

1.1 Introduction

As was mentioned in the summary section, our primary objective is to introduce a new technique of absorption spectroscopy that utilizes the Josephson effect that occurs in atomic point contacts. This technique allows observation of the absorption spectrum of a single molecule in the lower terahertz band. Since it is difficult to find satisfactory sources to generate radiation in the lower terahertz gap and because these frequencies correspond to vibrational modes of various molecules one can see the immediate applicability of this technique.

Since this technique involves the use of the Josephson effect, which is a superconducting phenomena, we felt it prudent to begin with a brief survey of superconductivity. Thus the primary purpose of chapter 1 is to introduce key concepts in superconductivity, namely quasi-particles, Cooper-pairs, Andreev reflection, and the sub-gap structure.

Due to the reliance of any spectroscopic technique on radiation, our second chapter details the effects of external radiation on the Josephson effect. Noting these external effects allows the reader to observe how previously introduced phenomena are altered by the introduction of external radiation (the sub-gap structure in particular). This alteration is directly related to the spectrum of the radiation and, as a result, is the key to our spectroscopic technique. Thus chapter 2 concludes with the relation between the incident radiation and the change in the sub-gap structure of a given contact.

Chapters 1 and 2 used experimental data that was obtained in order to verify the validity of the developed theories or to help give explanation of the physical effect of a previously obtained relation. No mention was made as to how this experimental data was obtained. Chapter 3 thus details the experimental techniques used by our group in order to obtain the previously presented results along with results to be presented in subsequent chapters.

The techniques of sample fabrication, measurement, and cryogenic setup are outlined in this chapter, along with computer simulations of the process and pictures of the actual samples.

Our final chapter introduces the spectroscopic technique to be used, along with the fabrication process and an SEM image of the sample. Before covering this technique we briefly review various spectroscopic techniques used in biology and highlight their advantages and disadvantages (noise being a recurrent concern). Chapter 4 also presents a means of determining the vibrational modes of the sample under investigation.

1.2 Fermi Liquid Theory

Although the observed phenomena of superconductivity is not as ubiquitous to the average reader as, say, magnetism or universal gravity, the concept is much easier to grasp than some of the more exotic physical phenomena (try explaining relativity to an 11 year old). With this in mind we felt it prudent to introduce the reader to superconductivity via its physical characteristics as opposed to its theoretical foundation.

Although superconductivity is marked by the abrupt vanishing of resistance at some critical temperature (T_c)[148, 149, 150], as illustrated, we must be cognizant from the outset that superconductivity is a thermodynamic phenomena, characterized not only by zero resistivity, but similarly zero permeability[1, 2]. This property, namely $\boldsymbol{B} = \mathbf{0}$ inside a superconducting material, is known as the Meissner effect[135].

A familiar analog to this phenomenon should readily come to mind for readers who have taken an introductory level electricity and magnetism course. If a perfect conductor is placed in an external electric field, the charges on the surface of the conductor will arrange themselves in such a way as to ensure that the electric field everywhere inside the conductor is zero, thus shielding the conductor. As would be expected, the mechanism for shielding the superconductor is facilitated by current on the surface of the superconductor.

An article on superconductivity whose initial focus rests upon the Meissner effect may appear to be somewhat misdirected. For if this aspect of superconductivity is of prime importance, would not the name of the phenomena at least hint at its existence (i.e., superconductivity/perfect diamagnetism)? Our reasoning for this apparent *faux pas* is that

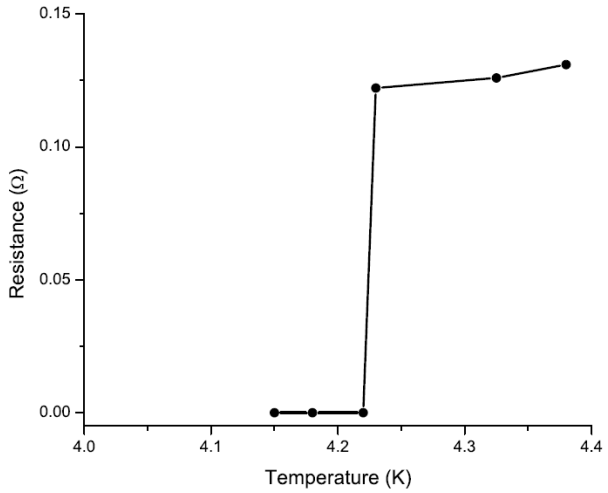

Figure 1: Superconducting transition temperature of mercury as determined by Kamerlingh-Onnes. Note the abrupt decrease in resistance to zero at the critical temperature (T_c), which is the primary characteristic of superconductors. Normal metals would continue to have a finite resistance even after absolute zero has been reached.

superconductors are classified based on the breaking down of the Meissner effect.

Superconductors may be classified as either type I or type II superconductors; their classification rests solely on either the abrupt or gradual breaking down of the Meissner effect. Our primary metal of interest, niobium, is a type II superconductor. Hence all subsequent references to superconductors will refer to type II superconductors unless otherwise stated.

Endeavoring to cover all aspects of the theoretical foundations of superconductivity in a single chapter is an ambitious undertaking. Although the ability to accomplish this feat is well within the author's capabilities, the focus of this thesis may inadvertently be blurred by such a detailed treatise. The primary purpose of this chapter is to equip the reader with enough of a foundation in superconductivity to make our detailed treatment of the response of a Josephson Junction to electromagnetic radiation less of a quantum leap and more of a gradual progression.

As might be anticipated, our starting point for analyzing a superconducting solid is the Hamiltonian. The general form of the Hamiltonian is:

$$H = \sum_{i=1}^{n} \frac{p_i^2}{2m_i} + \sum_{i<j}^{n} U_c(\mathrm{r}_i - \mathrm{r}_j) + \sum_{i=1}^{N} \frac{P_i^2}{2M_i} + \sum_{i<j}^{N} U_c(\mathrm{R}_i - \mathrm{R}_j) + \sum_{i=1}^{n}\sum_{k=1}^{N} U_c(\mathrm{R}_k - \mathrm{r}_i), \quad (1)$$

where the first two terms take into account the kinetic energy of the electrons and the

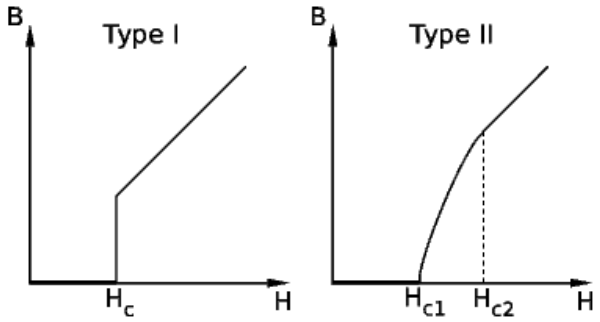

Figure 2: The left panel shows the behavior of a Type I superconductor as it switches abruptly from the Meissner state to the normal state. The right panel shows the behavior of a Type II superconductor as it transitions from the Meissner state to the mixed state to the normal state. The ability of Type II superconductors to exist in a mixed state contributes to most of the practical uses of superconductors.

potential energy between electrons, the next two are the kinetic energy of the ions and the potential energy between the ions, and the final term accounts for the potential energy between ions and electrons.

To describe the system, we will make a prudent simplifying assumption, which in essence turns off some of the aforementioned interactions. First it must be noted that the presence of the fourth term identifies an equilibrium position for the heavy ions (lattice points). As a consequence the fourth term merely acts to provide a periodic potential for the electrons to move about. The first simplifying assumption is that electrons do not interact with one another, essentially turning off the second term. With this model (independent electron) in place, the electrons are found in what are called Bloch states[15].

Although delving deeper into the characteristics of these states could fill an entire chapter of a solid state textbook[97], that would detract from this section's primary purpose and will be avoided. We must note that since electrons are Fermions (i.e., spin = $\frac{1}{2}$), they cannot all occupy the same energy level. For this reason in the ground state of the solid, these electrons fill up consecutively higher energy levels. Once every electron is in place, the highest occupied energy level is called the Fermi level. In the ground state, all energy levels below the Fermi level are filled, and all energy levels above the Fermi level are empty.

The energy of each constituent electron is not unique, thus describing the system in terms of energy will not suffice, but the electrons can be described in terms of the wave

vector $\boldsymbol{K}$. The relation between the energy and the wave vector is:

$$\varepsilon = \frac{\hbar}{2m}(k_x^2 + k_y^2 + k_z^2) \tag{2}$$

where k_x, k_y, and k_z are the various components of the wave vector $\boldsymbol{K}$. Thus in the ground state, all $\boldsymbol{K}$-states inside the Fermi sphere are filled, and all of those outside of the Fermi surface are empty.

At this point we wish to look at the situation from a slightly different perspective, which may seem a less intrinsic and more abstract approach to arrive at the same conclusion, it will serve as our guiding model when dealing with the more complex picture of incorporating interactions between electrons. We introduce the single particle propagator $G_0(\boldsymbol{K}, \boldsymbol{K'}, t)$, which gives us the probability that an electron in the state $\boldsymbol{K}$ will be in the state $\boldsymbol{K'}$ after some time t[5, 75, 143]. For our purpose, we will look at the Fourier transform of the single particle propagator:

$$G_0(\boldsymbol{K}, \omega) = \int_{-\infty}^{+\infty} dt G_0(\boldsymbol{K}, t) e^{i\omega t} \tag{3}$$

$$= \frac{1}{\omega - \varepsilon_k + i\delta_k}, \tag{4}$$

where δ is an infinitesimal positive quantity. To determine the momentum density distribution, $n(\boldsymbol{K})$, of the system, we must integrate the imaginary part of G_0 over all frequencies. Upon integration a heavy side function results whose interpretation is that all energy levels below the Fermi level ε_f are filled, whereas those above the Fermi level are empty, as illustrated in fig. 3. Thus we arrive at our previous conclusion.

Now interaction between electrons (*i.e.* taking into account the second term of the Hamiltonian) must be introduced. By allowing for the interaction between electrons our Fourier transform of the single particle propagator takes on the form:

$$G(\boldsymbol{K}, \omega) = \frac{G_0(\boldsymbol{K}, \omega)}{1 - G_0(\boldsymbol{K}, \omega)\Sigma(\boldsymbol{K}, \omega)}, \tag{5}$$

$$= \frac{1}{\omega - \varepsilon_K - \Sigma(\boldsymbol{K}, \omega)}, \tag{6}$$

where $\Sigma(\boldsymbol{K}, \omega)$ is the one particle irreducible energy.

Our aim is for this expression to be in a form similar to that of equation (4) so that the imaginary part may be integrated in order to obtain the momentum distribution $n(\boldsymbol{K})$

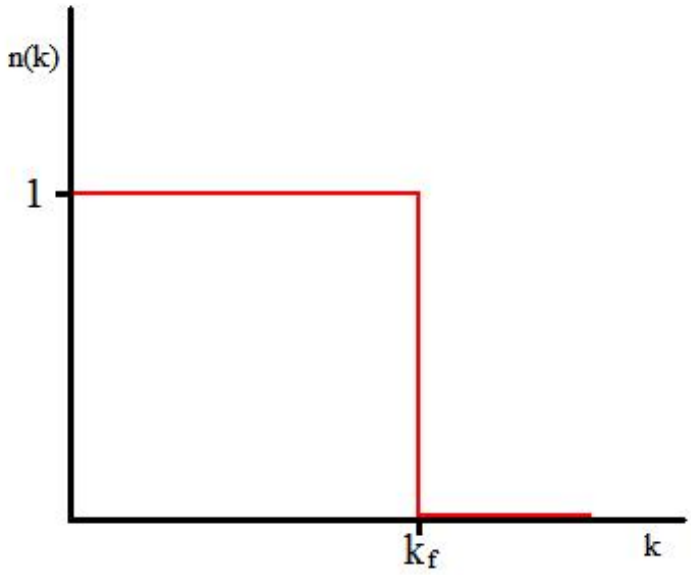

Figure 3: The wave state density is plotted assuming the electrons do not interact with one another. Note the discontinuity at the Fermi energy is 1, which is the residue of the single particle propagator. This plot implies that when the system is in its ground state, all energy levels below the Fermi level are occupied, whereas those above the Fermi level are empty.

of the system. By performing a Taylor expansion of the one particle irreducible self-energy about $\omega = \frac{\widetilde{\varepsilon}_K}{\hbar} = \frac{\varepsilon_K + \Sigma_r(\boldsymbol{K},\omega)}{\hbar}$, we obtain the expression:

$$G_0 = \frac{\boldsymbol{z}_K}{\omega - \varepsilon_k + \frac{i}{\tau_K}} \tag{7}$$

where

$$\tau_K = -\frac{1 - \frac{\partial \Sigma_r}{\partial \omega}}{\Sigma(\boldsymbol{K}, \varepsilon_K)} \tag{8}$$

$$\boldsymbol{z}_K = \frac{1}{1 - \frac{\partial \Sigma_r}{\partial \omega}} \tag{9}$$

By integrating this expression over all frequencies, we obtain the distribution illustrated in fig. 4.

Although this approach has illustrated the ground state distribution of our system when incorporating electron-electron interaction, it yielded an unforseen concept. We note that far below the Fermi level, the density is 1. As we approach the Fermi surface, the density decreases. These electrons have apparently lost a bit of their "character", and as a result,

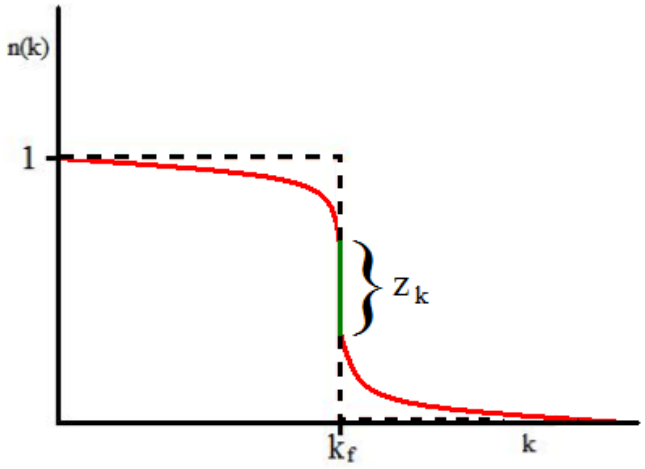

Figure 4: The wave state density is plotted allowing for interactions between electrons. Note the discontinuity at the Fermi energy is z_k that is the residue of the single particle propagator. Particles, whose energy lies close to the Fermi level, occupy a wave state whose density is neither 0 nor 1 but lies between these two values. The particles are called quasi-particles. By allowing for interaction between particles, these quasi-particles are created.

particles whose momentum falls close to the Fermi surface are called "quasi-particles"[107, 108]. A system made up of quasi-particles is called a Fermi liquid. The existence of quasi-particles is not exclusive to superconducting metals.

1.3 Cooper Pairs

Assuming electrons interact with one another and a periodic potential due to the ion's equilibrium position, the momentum distribution has been determine and another level of complexity must be added to the system. As previously mentioned, the interaction between ions acts to define an equilibrium position for the ions (lattice points). For a truly accurate description, we must account for the movement of the ions about this equilibrium position.

The vibration of the ions about their equilibrium position can be described in terms of modes. These modes couple with the motion of the electrons and thereby alter the results of the previous section. As opposed to describing the interaction in terms of coupled modes, the picture of momentum transfer between ions and electrons via phonons will be used. This is similar to describing the Coulombic force acting between electrons in terms of momentum transfer via photons.

A typical occurrence in a metal would be for an electron to pass by an ion and excite one of the vibrational modes of the ion. This situation will be described as the electron emitting a phonon and thus transferring momentum $\boldsymbol{q}$ to the ion (the electron loses momentum $\boldsymbol{q}$ as a result). Now, a likely occurrence is that another electron will pass by this ion; it will emit a phonon and transfer momentum $\boldsymbol{q}$ to the new electron.

Thus for all intents and purposes, what has happened is, the first electron transferred momentum $\boldsymbol{q}$ to the second electron using the ion as an intermediary. This is called phonon mediated interaction. This interaction is weaker than the direct Coulombic (photon mediated) interaction because the attraction between the ions and the electrons is more akin to a dipole interaction than that of two point charges.

To investigate this situation we must once again look at the Hamiltonian of our system. This time we will use the language of second quantization. The Hamiltonian will be of the form[75]:

$$H = \sum_{k,\sigma} \varepsilon_k c^\dagger_{k,\sigma} c_{k,\sigma} + \sum_{k,k',q,\sigma,\sigma'} \frac{1}{4\pi\epsilon_0} \frac{2\pi e^2}{q^2} c^\dagger_{k+q,\sigma} c^\dagger_{k'-q,\sigma'} c_{k,\sigma} c_{k',\sigma'} + \sum_{k,k',q,\sigma,\sigma'} \boldsymbol{V}_q c^\dagger_{k+q,\sigma} c^\dagger_{k'-q,\sigma'} c_{k,\sigma} c_{k',\sigma'} \tag{10}$$

where $c^\dagger_{k,\sigma}$ is the creation operator placing an electron in the state $|k,\sigma>$, and $c_{k,\sigma}$ is the annihilation operator that takes an electron out of the state $|k,\sigma>$. The fact that electrons are Fermions means that the anti-commutation relation ($c^\dagger_{k,\sigma} c_{k',\sigma'} + c_{k',\sigma'} c^\dagger_{k,\sigma} = \delta_{k,k'}\delta_{\sigma,\sigma'}$) must hold true. We note that $c^\dagger_{k,\sigma} c_{k,\sigma}$ is the number operator, telling us how many electrons are in the state $|k,\sigma>$.

Thus the first term of the Hamiltonian gives us the total non-interacting energy due the the energy levels that the electrons occupy. The second term deals with the Coulombic interaction between electrons, describing the event where electrons in the initial states $|k,\sigma>$ and $|k',\sigma'>$ interact with one another via the Coulombic force and are changed to the states $|k+q,\sigma>$ and $|k'-q,\sigma'>$, respectively, where $\boldsymbol{q}$ is the momentum transferred during the interaction.

The final, as yet to be determined, term represents the similar characteristic interaction as above with the exception of the mode of interaction being phonon mediated as opposed

to Coulombic. To determine the form of this operator, it is noted that the free phonon propagator has the form[75]:

$$B_0(\boldsymbol{q},\omega) = \frac{2\hbar\omega_q}{\hbar(\omega^2-\omega_q^2)+i\hbar}, \tag{11}$$

where ω_q is the eigenvalue of the phonon in the plane wave state $|\boldsymbol{q}>$. This implies that our expression for V is[75]

$$\boldsymbol{V}_q = \frac{2 \mid \boldsymbol{M}_q \mid^2 \hbar\omega_q}{\omega^2-\omega_q^2}, \tag{12}$$

where $|\boldsymbol{M}_q|$ is a matrix element including the coupling between electrons and phonons. The magnitude of this quantity is not important for the present discussion. ω_q is the frequency of the typical ionic vibration, which is usually in the terahertz range.

From equation (12) it is seen that for all frequencies below ω_q the phonon mediated potential will be negative. This implies that at energies which deviate from the Fermi energy an amount $h\omega < h\omega_q$, the interaction between electrons will be attractive. For all electrons whose energy deviates from the Fermi energy an amount greater than $h\omega_q$, the interaction is repulsive, and these terms may be placed in with the Coulombic terms. These terms may slightly alter the graph from fig. 2, increasing the number of quasi-particles, but there will be no fundamental difference.

1.3.1 Attractive Interaction

We now wish to determine the effect an attractive force between electrons would have on the system. The somewhat artificial system to serve as our model is that of an inert Fermi sea of electrons inside of the Fermi surface. Two electrons will be added, which by necessity must be outside of the Fermi surface. From the advantageous position of knowing the result, it will be assumed the two electrons have opposite momentum and spin (*i.e.*, $|k,\sigma>$ and $|-k,-\sigma>$). These electrons will interact with one another via an attractive potential V. When there is no interaction between the electrons, the eigenvalue equation

$$H_0|k,\sigma,-k,-\sigma>= 2\varepsilon_0|k,\sigma,-k,-\sigma> \tag{13}$$

is obtained. By adding the attractive interaction to the system (*i.e.*, $H = H_0 + V$) a new eigenvalue equation results:

$$H|1,2>= E|1,2> . \tag{14}$$

By representing the state $|1,2>$ in terms of the basis set $|k,-k>$ and multiplying by the bra $< k',-k'|$ we obtain the equation

$$a_k[2\varepsilon_k - E] = \sum_{k'} a_{k'} < k',-k'|V|k,-k >, \tag{15}$$

where a_k is the coefficient of the basis set when expressing $|1,2>$ in terms of $|k,-k>$.

We now make use of the fact that the force was attractive for energies that deviated from the Fermi energy by an amount $h\omega < h\omega_q$. For typical ionic vibrations this amount is extremely small compared to the Fermi energy. As a result we may assume that the potential in this shell is constant. Hence we obtain

$$a_k[2\varepsilon_k - E] = V \sum_{k'} a_{k'} \Theta(\varepsilon_{k'} - \varepsilon_f)(\hbar\omega_0 - |\varepsilon_{k'} - \varepsilon_f|), \tag{16}$$

which may be expressed in terms of the continuous density function in energy space since the number of particles in a typical metal is of the order of Avogadro's number. Thus equation (16) may be expressed as

$$a(\varepsilon)[2\varepsilon - E] = V \int d\varepsilon' D(\varepsilon') a(\varepsilon'). \tag{17}$$

Since the right hand side has no a(ε) dependence, we see that a(ε) must be proportional to $\frac{1}{2\varepsilon - E}$. This implies

$$V \int_{\varepsilon_f}^{\varepsilon_f + \hbar\omega_0} \frac{d\varepsilon' D(\varepsilon')}{2\varepsilon' - E} = 1. \tag{18}$$

Since the shell in which the potential is attractive is small, we may assume the density of state is constant (and equal to the density at the Fermi surface), and by letting $VD(\varepsilon_f) = \lambda$ we obtain the expression

$$\lambda \int_{\varepsilon_f}^{\varepsilon_f + \hbar\omega_0} \frac{d\varepsilon'}{2\varepsilon' - E} = 1, \tag{19}$$

which implies

$$\frac{\lambda}{2} \ln[\frac{2(\varepsilon_f + \hbar\omega_0) - E}{2\varepsilon_f - E}] = 1. \tag{20}$$

This leads to

$$\frac{2}{\lambda} = \ln[1 + \frac{2\hbar\omega_0}{2\varepsilon_f - E}]. \tag{21}$$

Since the left side is positive, this implies $2\varepsilon_f - E > 0$. But this energy is forbidden since the energy levels below the Fermi surface are filled. Thus by allowing an attractive force between electrons, they are able to occupy energy levels that are forbidden in Fermi statistics. This apparent catastrophe can be remedied if we look at the 2 electrons not as separate entities but as a pair. The spin of this pair, due to our prudent choice of electrons, is zero. Therefore this *Cooper pair*[46] is not subject to Fermi statistics and may therefore have energy beneath the Fermi level. The electrons whose energy falls within the region $h\omega < h\omega_q$ about the Fermi surface will likely form Cooper pairs since it is advantageous from an energy perspective.

1.3.2 Josephson Effect

We note that for the quasi-particles, which constitute the Fermi sea, restrictions due to Fermi statistics prohibit the quasi-particle from having the same wave function. Thus these constituent particles tend to differ in phase. Most bulk properties that arise from quasi-particles are predicted by taking a statistical average of the system, but due to the random orientation of the phase, the average tends to conceal all effects due to the phase[118].

Cooper pairs, on the other hand, may occupy the same energy level, and therefore description by the same wave function is not forbidden. The typical wave function has a volume whose radius is much larger than the typical separation between adjacent Cooper Pairs. As a consequence there is an enormous overlap of these wave functions. It becomes advantageous, from an energy perspective, for the phases of these Cooper pairs to lock up. Therefore we can describe the entire system of Cooper pairs with the wave function:

$$\psi = \rho_s^{\frac{1}{2}} e^{i\phi}, \tag{22}$$

where ρ_s is the density of Cooper pairs, and ϕ is the phase of the system of Cooper pairs.

A brief look at the effects of having two superconductors in close enough proximity to where the phases interact with one another, but don't lock up, will shed some light on the

mechanism of superconductivity. The respective wave functions of superconductors 1 and 2 may be written as:

$$\psi_1 = \rho_{1s}^{\frac{1}{2}} e^{i\phi_1} \tag{23}$$

and

$$\psi_2 = \rho_{2s}^{\frac{1}{2}} e^{i\phi_2}. \tag{24}$$

The assumption that the systems interact with one another will be accounted for by expressing Schrodinger's time dependent equation for superconductors 1 and 2, respectively, as[70]:

$$i\hbar\dot{\psi}_1 = eV\psi_1 + K\psi_2 \tag{25}$$

and

$$i\hbar\dot{\psi}_2 = -eV\psi_2 + K\psi_1, \tag{26}$$

where V is the potential difference between the two superconductors, and K is a coupling constant that takes into account the strength of overlap between the two superconductors' wave functions.

By expanding the exponential in equations (23) and (24), the wave functions may be written as:

$$\psi_1 = \rho_{1s}^{\frac{1}{2}}(\cos(\phi_1) + i\sin(\phi_1)); \tag{27}$$

$$\psi_2 = \rho_{2s}^{\frac{1}{2}}(\cos(\phi_2) + i\sin(\phi_2)). \tag{28}$$

By placing these two expressions into equations (25) and (26) we obtain:

$$\dot{\phi_1} = -\frac{K}{\hbar}(\frac{\rho_2}{\rho_1})^{\frac{1}{2}}\cos(\delta) - \frac{eV}{\hbar}; \tag{29}$$

$$\dot{\phi_2} = -\frac{K}{\hbar}(\frac{\rho_1}{\rho_2})^{\frac{1}{2}}\cos(\delta) + \frac{eV}{\hbar}; \tag{30}$$

$$\dot{\rho_1} = \frac{2K}{\hbar}(\rho_1\rho_2)^{\frac{1}{2}}\sin(\delta); \tag{31}$$

$$\dot{\rho_2} = -\frac{2K}{\hbar}(\rho_1\rho_2)^{\frac{1}{2}}\sin(\delta), \tag{32}$$

where the difference in phases of the two superconductors is expressed as:

$$\delta = \phi_1 - \phi_2. \tag{33}$$

The current density between the two superconductors must be equal to the product of the change in density of Cooper pairs and the corresponding charge of a Cooper pair of either of the superconductors. Thus

$$J = -2e\dot{\rho_1} = \frac{4Ke}{\hbar}(\rho_1\rho_2)^{\frac{1}{2}}\sin(\delta), \tag{34}$$

which is the DC Josephson effect[11, 93]:

$$J = J_0\sin(\delta). \tag{35}$$

The rate of change of the phase difference between the superconductors is seen from equations (29) and (30) to be:

$$\dot{\delta} = \frac{2e}{\hbar}V, \tag{36}$$

which is the Josephson phase-voltage relation. These two relations, which are crucial to our later investigation of Josephson radiation, hint that superconducting current is not the result of individual Cooper pairs, but but rather of a coherent superconducting condensate.

Since the primary purpose for this section is to introduce superconductivity, concentration will be placed on those properties of a system responsible for superconductivity. In this vain, returning to the language of second quantization, the Hamiltonian may be expressed in BCS (**B**ardeen, **C**ooper, and **S**chrieffer) reduced form as:

$$H = \sum_{k,\sigma}\varepsilon_k c^\dagger_{k,\sigma}c_{k,\sigma} + \sum_{k,k',q,\sigma}\boldsymbol{V}_{k,k'}c^\dagger_{k,\sigma}c^\dagger_{-k,-\sigma}c_{-k',-\sigma}c_{k',\sigma}, \tag{37}$$

where V is the attractive potential due to phonon mediated interaction. Note that the first term is, once again, the non-interacting energy due to the energy levels the electrons occupy. The second term represents two electrons in states $|-k',-\sigma>$ and $|k',\sigma>$ interacting via the potential V and being scattered into the states $|-k,-\sigma>$ and $|k,\sigma>$. This BCS reduced Hamiltonian will act as the starting point for BCS theory.

1.4 BCS Theory

In describing superconductivity the previous section's primary objective was to introduce the reader to the "role players" of the phenomena, namely quasi-particles and Cooper pairs. Now we must alter our objective and pursue an analysis of the system based primarily on excitation energy considerations. We concluded the previous section with what will serve as this section's point of departure, namely the BCS reduced Hamiltonian[18, 19]:

$$H = \sum_{k,\sigma} \varepsilon_k c^\dagger_{k,\sigma} c_{k,\sigma} + \sum_{k,k',q,\sigma} \boldsymbol{V}_{k,k'} c^\dagger_{k,\sigma} c^\dagger_{-k,-\sigma} c_{-k',-\sigma} c_{k',\sigma}. \tag{38}$$

A first step in the analysis of a superconducting system would be to express the BCS reduced Hamiltonian in a basis that, although less conducive to physical interpretation, allows much easier determination of the superconductor's energy spectrum[18]. This can be accomplished by diagonalizing the Hamiltonian. By introducing the operators[34, 178]:

$$\gamma^*_{\boldsymbol{k},0} = u^*_{\boldsymbol{k}} c^\dagger_{\boldsymbol{k},\uparrow} - v^*_{\boldsymbol{k}} c^\dagger_{-\boldsymbol{k},\downarrow} \tag{39}$$

and

$$\gamma^*_{\boldsymbol{k},1} = u^*_{\boldsymbol{k}} c^\dagger_{-\boldsymbol{k},\downarrow} + v^*_{\boldsymbol{k}} c^\dagger_{\boldsymbol{k},\uparrow}. \tag{40}$$

The Hamiltonian may be written as:

$$H = H_{s,0} + \sum_k E_{\boldsymbol{k}} (\gamma^*_{\boldsymbol{k},0} \gamma_{\boldsymbol{k},0} + \gamma^*_{\boldsymbol{k},1} \gamma_{\boldsymbol{k},1}). \tag{41}$$

Before giving an interpretation of the above expressions, a review of the interpretation of the BCS reduced Hamiltonian would be prudent. The first term of the BCS reduced Hamiltonian was introduced as being the non-interacting energy of the system (*i.e.*, the energy that resulted from the independent electron picture); whereas the second term accounted for the attractive interaction between electrons.

The formation of Cooper pairs that results from this interaction acts to lower the energy of the system. The first term in our new Hamiltonian represents the energy of the system after this condensation has occurred and is thus lower than the non-interacting energy in the BCS reduced Hamiltonian.

The second term of the new Hamiltonian accounts for excitations that may occur. By way of practical example, we may look at the reaction of an arbitrary Cooper pair to the addition of a large amount of energy to the system. The result is similar to that of a diatomic molecule that has been excited. The molecule (H_2 for example) breaks apart into its constituent atoms. The Cooper pair, likewise, splits into its constituent parts, which, due to the close proximity of these electrons to the Fermi surface, are by definition quasi-particles. Thus the second term of the Hamiltonian represents the energy associated with quasi-particle excitation. This point is reinforced by the similarity of the operator $\gamma^*_{\boldsymbol{k},0}\gamma_{\boldsymbol{k},0}$ and the number operator $c^\dagger_{k,\sigma}c_{k,\sigma}$ that revealed the number of electrons in the state $\boldsymbol{k}$. The operators $\gamma_{\boldsymbol{k},0}$ and $\gamma_{\boldsymbol{k},1}$ are called bogolliubons.

The coefficients $u^*_{\boldsymbol{k}}$ and $v^*_{\boldsymbol{k}}$ can be interpreted, due to their positioning in equations (39) and (40), as the degree to which a quasi-particle excitation is "electron-like" and "hole-like" respectively. This is verified to a greater extent by noting that $u^2_{\boldsymbol{k}} + v^2_{\boldsymbol{k}} = 1$. The excitation energies of the diagonalized Hamiltonian are

$$E_{\boldsymbol{k}} = (\Delta^2_{\boldsymbol{k}} + \xi^2_{\boldsymbol{k}})^{\frac{1}{2}} \tag{42}$$

where $\xi_{\boldsymbol{k}}$ is the energy of the quasi-particle relative to the Fermi level. The term $\Delta_{\boldsymbol{k}}$ is seen to be an energy gap of order 1meV. (This is its physical interpretation, mathematically (See Appendix A.) it is a variable that arises from minimization of the ground state energy and must be solved self-consistently.)

The graph of energy as a function of momentum $\boldsymbol{K}$ is illustrated in fig. 5. This explains the experimentally observed condition, that there is a minimum amount of energy Δ needed in order to excite a superconductor. Henceforth, the energy Δ will be referred to as the gap energy. It must be noted that there are no available states in the superconductor for charges with energies that fall within the region of Δ above or below the Fermi energy. This result will be crucial for our investigation of charge transport in nanowires.

The developed theory thus far has not given explicit mention as to what makes given materials superconducting and other materials not. The exact value of the potential that was introduced in the Hamiltonian describing the phonon mediated interaction is dependent

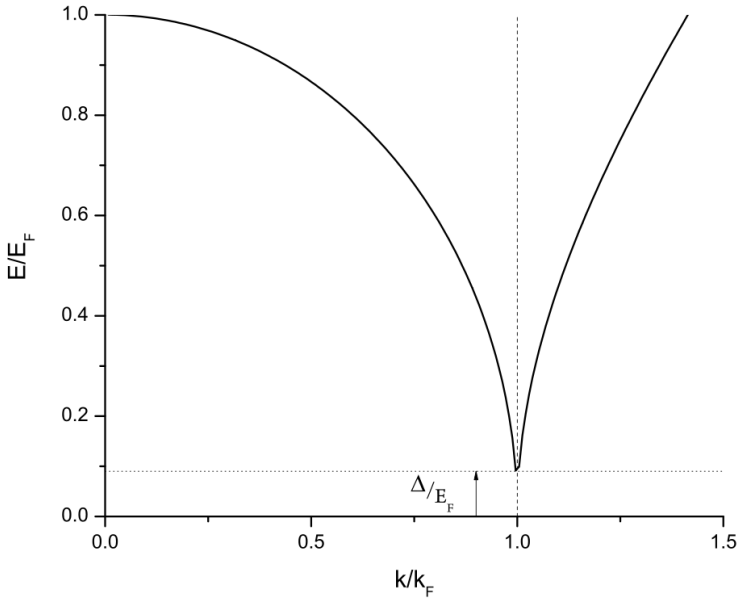

Figure 5: The superconductor's energy spectrum is in agreement with the experimentally verified behavior of a minimum energy Δ needed in order to take a superconductor out of its ground state. Note that quasi-particles, whose individual energy would fall into this gap region, will form Cooper pairs. This gap energy can be seen as the energy required to split a Cooper pair and thus remove the superconductor from its ground state.

on the material median. This potential "theoretically" contains all the information as to whether given metals will find forming superconducting condensates energetically advantageous. From this potential function the critical temperature should be able to be calculated, but this function depends on the specific characteristics of the metal and is thus beyond the scope of first principles calculation. Thus experimental measurements must be made in order to determine whether a given material will be superconducting.

Just as the inductance, capacitance, and resistance of a given material are not only dependent on the material (*i.e.*, the dielectric between the capacitor plates or whether the inductor has an iron filling), but also on the geometry of the circuit element in question, the properties of a given superconductor are dependent on the specific material and on the dimensions of the material. The dimensions of a superconductor have characteristic effects on the transport of charge and may thus be used for experimental calculations. The next section will cover the effects that dimensions have on the transport properties of superconductors.

1.5 Mesoscopic Superconductivity

Thus far the properties of a metal that have been discussed are those arising from the general interaction between electrons and heavy ions and those properties arising from the specific metal. No mention has been made to the dimensions (length and width) of the material being considered. That this should play an important role in our description should come as no surprise to those with any experience in quantum mechanics or optics.

To take a practical example from optics, recall that if the dimensions of a material coming into contact with light are of the same order as the wavelength of the light, then physical optics must be used. Phenomena such as diffraction and interference are thus observed. If the dimensions of the material are much greater than that of the light's wavelength, geometric optics may be used to analyze the system. An analog to this occurs when delving into the transport properties of superconducting nanowires. For if the dimensions of the transport region are comparable to that of the Fermi wavelength, a scattering approach must be used for the investigation and prediction of resultant phenomena.

We may categorize physical phenomena as falling into one of three categories: macroscopic, microscopic, and mesoscopic. Physical behavior that is common experience generally falls into the category of macroscopic. In this region, the laws of classical mechanics hold true. The interaction of a single electron interacting with an atom would fall into the realm of microscopic, in which case quantum mechanics is needed.

The region between both of these extremes, in which investigations of numerous charge carriers in a metal on the scale of micrometers is carried out, is termed mesoscopic[21]. In this region a purely quantum mechanical calculation would be impossible, but an ensemble technique is still needed. Unless otherwise stated, all future references to superconductivity will be made with reference to mesoscopic superconductivity.

The category of mesoscopic superconductivity can be broken down further when considering the transport of charge carriers[22]. These categories are: diffusive, ballistic, and quantum point contact. The diffusive region is when the dimensions of the restriction are such that the charge carrier will have many collisions before passing through the junction (*i.e.*, the mean free path of the particle is much shorter than the length of the junction).

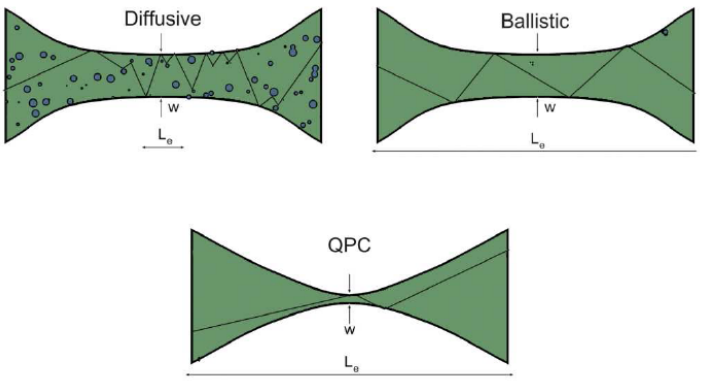

Figure 6: The three charge transport regimes are: (a) the diffusive regime marked by small mean free path in comparison to all dimensions of the metal resulting in Ohm's law holding true, (b) the ballistic regime in which the mean free path is of the order of the contact's width, and (c) the quantum point contact (QPC) regime in which the length of the junction is of the order of the mean free path, and the width is of the order of the Fermi wavelength. Our experiments are conducted in the quantum point contact regime.

In the ballistic region both the length and width of the junction are small compared to the mean free path of the charge carrier.

A Quantum point contact's defining characteristic is that both the length and width of the restrictive region are small in comparison to the mean free path of the charge carrier, but the width is of the order of the Fermi wavelength[23]. To investigate phenomena that fall within this region, we must use the Landauer scattering approach.

1.5.1 Landauer Scattering

The Landauer scattering formalism[109] allows us to describe the transport of charge carriers through a quantum coherent conductor in terms of electron waves transmitting through individual channels. It must be noted that this formalism is not exclusive to transport in superconducting media. The assumption that the dimensions of the junction are much smaller than the mean free path of the charge carrier is a prerequisite for this formalism. This is indicated by the formalism's tacit assumption that the independent electron picture is valid. As a result the charge carriers are non-interacting quasi-particles.

The system is modeled as two separate reservoirs, each connected to the scattering center by several leads. Electrons emitted from the reservoir can either be reflected from

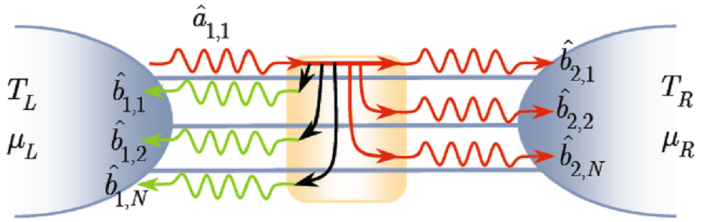

Figure 7: Pictured is a model of the Landauer scattering formalism's reservoirs and scattering center. The modes of the electron waves are mixed, and thus the scattering matrix has yet to be diagnolized. Note that a wave from the left reservoir can be reflected at the scattering center and return to the left reservoir along any of the N modes, or the wave can be transmitted through the scattering center and reach the right reservoir along any of the N modes.

the scattering center or transmitted through the scattering center.

A specific example will illustrate the point. We will assume that each reservoir (R_L and R_R) has a single lead to the coherent scatterer. The electron waves that are present in the leads can occupy one of four modes. If an electron in mode 1 is emitted from R_L, the electron can either be reflected from the scattering center and travel back to R_L in one of the four modes allowed in the lead connecting R_L to the scattering center. Or, the electron can be transmitted and travel toward R_R in one of the four modes allowed in the lead connecting R_R to the scattering center. Thus there are 8 ($= 4+4$) possible options for the electron in mode 1.

For a system in which the reservoirs are connected to the scattering center by a single lead that allows N possible modes, there are $2N$ possible options for an electron emitted from a reservoir occupying a given mode, as illustrated in fig. 7. The scattering formalism finds an alternative basis such that an electron, emitted from a reservoir through a given *channel* (replacing the aforementioned mode), has only two options: be reflected back through the same channel, or to be transmitted through a single corresponding channel, as illustrated in fig. 8. Consequently there is no mode mixing after the Landauer scattering formalism has been implemented.

In order to represent the electron modes incident to the scattering center from the left, we will introduce the creation and annihilation operators $a^\dagger_{1,i}(E)$ and $a_{1,i}(E)$, respectively, and $b^\dagger_{1,i}(E)$ and $b_{1,i}(E)$ to represent outgoing (from the scattering center and towards the

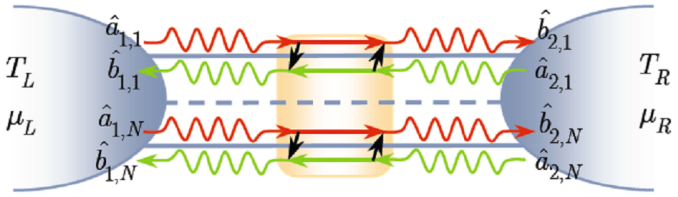

Figure 8: Pictured is a model of the Landauer scattering formalism's reservoirs and scattering center. The modes of the electron waves are uncoupled and hence the scattering matrix has been diagnolized. The total current passing through the junction is the sum of the current through each channel. Note that a wave from the left reservoir can either be reflected at the scattering center and return to the left reservoir along a single channel (mode) or the wave can be transmitted through the scattering center and reach the right reservoir along a single channel (mode).

left reservoir) electron modes. Electron modes incident on the scattering center from the right will require the additional creation and annihilation operators $a^{\dagger}_{2,i}(E)$ and $a_{2,i}(E)$, respectively, and $b^{\dagger}_{2,i}(E)$ and $b_{2,i}(E)$ to represent outgoing electron modes.

These operators are not independent, but are related to one another via the scattering matrix S, which, due to charge conservation, must be unitary. The relation is

$$\begin{pmatrix} \boldsymbol{b}_1 \\ \boldsymbol{b}_2 \end{pmatrix} = S \begin{pmatrix} \boldsymbol{a}_1 \\ \boldsymbol{a}_2 \end{pmatrix}, \tag{43}$$

where $\boldsymbol{b}_1$ and $\boldsymbol{b}_2$ are the $N \times 1$ column matrices containing the outgoing annihilation operators for modes 1 through N, and $\boldsymbol{a}_1$ and $\boldsymbol{a}_2$ are the $N \times 1$ column matrices containing the incident annihilation operators for modes 1 through N. When the modes are mixed, as in fig. 7, the scattering matrix S is in no particularly useful form. Noting that S is unitary, we may decompose the matrix into four square $N \times N$ blocks:

$$S = \begin{pmatrix} s_{11} & s_{12} \\ s_{21} & s_{22} \end{pmatrix}, \tag{44}$$

where the off diagonal matrices are called transmission matrices, because they contain all information about the probability of transmission of the electron waves. The diagonal matrices are labeled the reflection matrices due to their containing all information about the probability of reflection of the electron waves.

Although the transmission and reflection matrices contain all information about the probability of transmission and reflection, in order to obtain this information we must diagonalize these matrices. This is tantamount to finding a new basis (similar to the technique used in our creation of bogolliubons in the BCS theory) in which to represent the scattering problem. Once diagonalized, the resulting scattering matrix S' is

$$S' = \begin{pmatrix} -iR^{\frac{1}{2}} & T^{\frac{1}{2}} \\ T^{\frac{1}{2}} & -iR^{\frac{1}{2}} \end{pmatrix}. \tag{45}$$

The coefficients of the matrices T and R are the probability of transmission and reflection through each individual conduction channel. Thus we have succeeded in representing the problem in a basis where there is no mixing of modes.

As will be seen, the total current passing through the junction can be determined by knowing the coefficients of the matrices T and R, but an added benefit has emerged. The transmission coefficients of the matrices T and R are the eigenvalues of the transmission and reflection matrices. Since these values are unique for a given matrix, this implies the transmission coefficients can serve as a way of identifying a given system. If we label the transmission coefficients τ_i, then the collection of coefficients $(\tau_1, \tau_2, ..., \tau_N)$ will be referred to as the mesoscopic PIN code of the system.

In order to determine the current, we note that similar to our interpretation of the combination of operators $c^\dagger_{k,\sigma} c_{k,\sigma}$ being the number operator, the combination of operators $\langle a^\dagger_{\alpha,i}(E) a_{\alpha,i}(E)\rangle$ and $\langle b^\dagger_{\alpha,i}(E) b_{\alpha,i}(E)\rangle$ indicate the mean value of mode occupancy. By allowing the reservoirs to be a perfect source and sink (*i.e.*, no scattering at the lead-reservoir interface), the mean value of mode occupancy is determined by the temperature and chemical potential of the reservoir. Therefore the mean value of mode occupancy is given by the Fermi function:

$$f_\alpha(E) = \langle a^\dagger_{\alpha,i}(E) a_{\alpha,i}(E)\rangle = \langle b^\dagger_{\alpha,i}(E) b_{\alpha,i}(E)\rangle, \tag{46}$$

where

$$f_\alpha(E) = \frac{1}{1 + e^{(E-\mu_0)/k_B T_\alpha}}. \tag{47}$$

The current passing through the junction (see Appendix B) may be expressed as[42]:

$$I(t) = \frac{e}{h} \iint dE dE' (a^{\dagger}_{\alpha,i}(E) a_{\alpha,i}(E) - b^{\dagger}_{\alpha,i}(E) b_{\alpha,i}(E)) e^{i(E-E')t/\hbar}. \tag{48}$$

Since the incident and outgoing operators are not independent, we may eliminate $b^{\dagger}_{\alpha,i}(E)$ and $b_{\alpha,i}(E)$ by expressing them in terms of $a^{\dagger}_{\alpha,i}(E)$ and $a_{\alpha,i}(E)$. By introducing the operator $A_{\alpha\beta} = \delta_{\alpha 1}\delta_{\beta 1} - s^{*}_{1\alpha} s_{1\beta}$, we obtain the relation:

$$a^{\dagger}_{\alpha,i}(E) a_{\alpha,i}(E) - b^{\dagger}_{\alpha,i}(E) b_{\alpha,i}(E) = \sum_{\alpha,\beta=1,2} A_{\alpha\beta} a^{\dagger}_{\alpha}(E) a_{\beta}(E). \tag{49}$$

Thus the current can be expressed as:

$$I(t) = \frac{e}{h} \sum_{\alpha,\beta=1,2} \iint dE dE' A_{\alpha\beta} (a^{\dagger}_{\alpha}(E) a_{\beta}(E)) e^{i(E-E')t/\hbar}. \tag{50}$$

The average current then may be written as:

$$\langle I(t) \rangle = \frac{e}{h} \sum_{\alpha,\beta=1,2} \iint dE dE' A_{\alpha\beta} \langle a^{\dagger}_{\alpha}(E) a_{\beta}(E) \rangle e^{i(E-E')t/\hbar}. \tag{51}$$

Combining this with the Fermi function results in:

$$\langle I(t) \rangle = \frac{e}{h} \int dE \sum_{\alpha=1,2} A_{\alpha\alpha} f_{\alpha}(E), \tag{52}$$

where we have used the relation $\langle a^{\dagger}_{\alpha}(E) a_{\beta}(E) \rangle = \delta_{\alpha\beta} f_{\alpha}(E) \delta(E - E')$, which is a consequence of equation (46). The sum of the diagonal elements of the A matrix are the transmission coefficients. Consequently the current can be expressed as:

$$\langle I(t) \rangle = \frac{e\boldsymbol{\tau}}{2\pi\hbar} \int dE (f_1(E) - f_2(E)), \tag{53}$$

where $\boldsymbol{\tau}$ is the sum of the transmission coefficients. Thus the current may be written as:

$$\langle I(t) \rangle = \frac{e^2}{h} 2\boldsymbol{\tau} V \tag{54}$$

if spin degeneracy is taken into account.

This looks strikingly similar to Ohms Law ($I = VG$, where G is conductance (R^{-1})), and implies

$$G = \frac{2e^2}{h} \tau. \tag{55}$$

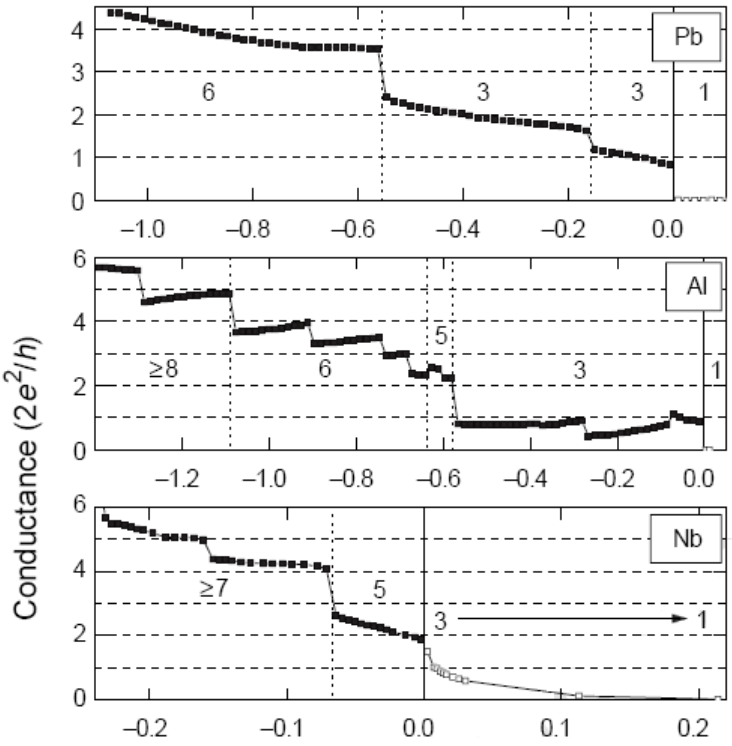

Figure 9: The conductance (measured in G_0) across an atomic point contact is plotted as a function of tip separation (measured in nanometers) for lead, aluminum, and niobium. Note the quantized conductance until the tips have completely separated at which point an exponential decrease in current results as predicted from quantum mechanics. The numbers on the plot indicate the number of conduction channels except where $\geq$ appears, which indicates that only a lower bound could be determined due to deviations from theory as a result of modified quasi-particle densities or scattering[161].

The expression $\frac{2e^2}{h}$ is called the conductance quantum and thus labeled G_0. Therefore the current through the restriction may be expressed as:

$$\langle I(t) \rangle = (G_0 \boldsymbol{\tau}) V. \tag{56}$$

That the conductance in a nanowire is quantized can be seen from the experimental results of conductance verses contact separation[160]. Figure 9 illustrates the conductance through lead, aluminum, and niobium nanowires. It is noted that the conductance decreases in a step-like fashion until complete separation between the contacts occurs. After the contact has been broken the conductance decreases exponentially as predicted by quantum mechanics (*i.e.* tunneling).

This illustrates that we may experimentally determine $\boldsymbol{\tau}$, but $\boldsymbol{\tau}$ is the sum of the transmission coefficients. Moreover the conductance verses contact separation graph does not tell us the mesoscopic PIN code. By noting that the number of conductance channels is equal to the valence of the atom that makes up the nanowire, we may be tempted to assume that conductance immediately before complete separation is due to complete transmission ($\tau_i = 1$) of one of the channels and complete reflection ($\tau_j = 0$) in all other channels. This can be neither verified nor disproved by the current experimental results.

In order to determine the PIN code unambiguously, we must investigate the IV(current vs. voltage) characteristics of the contact. Before endeavoring this task, we must introduce a phenomena specific to superconductors known as Andreev reflection, which explains a peculiarity in the IV characteristics of the contact. The results of Andreev reflection can be correlated to the specific transmission coefficients of a given sample and may be used to determine the mesoscopic PIN code.

1.5.2 Andreev Reflection

In order to analyze the IV (current vs. voltage) characteristics of our contact, we must first be cognizant of what conditions must be satisfied in order for current to flow between the contacts. As was shown for a superconductor at the end of the BCS section, in its ground state all electrons near the Fermi level are paired, and there is an energy gap Δ for the creation of quasi-particle excitation.

In order for current to flow between the contacts, two quasi-particles must be created (one for each electrode). Therefore the energy supplied to the system should exceed 2Δ if current is expected to be observed passing between the contacts. Since an electron acquires an amount of energy eV when traversing the junction, we would expect for no current to flow for voltages less than $\frac{2\Delta}{e}$, as illustrated in the left panel of fig. 10.

The IV graph that is actually obtained is that in the right panel of fig. 10. In order to explain this apparently contradictory phenomena, we must once again resort to a simple model for our system. The system will be modeled as a superconducting-normal-superconducting (SNS) interface. The region between the contacts of the superconductors

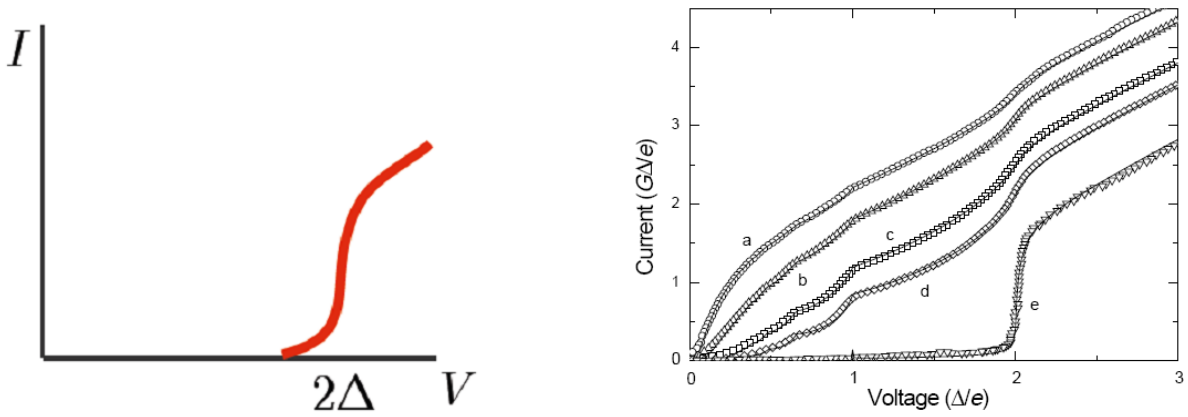

Figure 10: The left panel simulates the IV curve assuming an energy of 2Δ must be supplied by the voltage source in order for current to flow across the junction. The right panel illustrates the experimental IV curve in reduced units, leading to the impetus for a charge transport mechanism to be created in order to explain the experimental observation. Note that each curve (a-d) consists of four conduction channels with a different distribution of transmission coefficients (*i.e.*, PIN codes). Curve e consists of one channel of whose transmission coefficient makes the system fall into the tunneling regime, hence the radical difference from curves a-d[161].

is considered the normal metal region.

In order to explain the current that develops for voltages less than $\frac{2\Delta}{e}$, we must investigate the behavior of the electrons at the interface between the normal metal and the superconducting metal. In considering the NS interface, we note charges that reach the interface with energy that falls within the energy gap region ($E < 2\Delta$) will not be able to enter the superconductor, due to the absence in availability of energy states in the superconductor. From common experience we would expect this to lead to reflection of the charge carrier back into the normal metal as illustrated in the first panel of fig. 11.

With Andreev reflection[12], when an electron whose energy (E_e) is above the Fermi level yet still less than the gap energy (2Δ) reaches the NS interface, the electron is reflected back into the normal metal as a hole whose energy is E_e less than the Fermi energy (E_f). In order for charge to be conserved in this process, two electrons must appear in the superconductor. These two electrons form a Cooper pair whose total energy is $2E_f$[23]. Since the two electrons form a Cooper pair and are not individual quasi-particles, they are allowed to occupy the energy region that was prohibited to the electron. This is an example of a

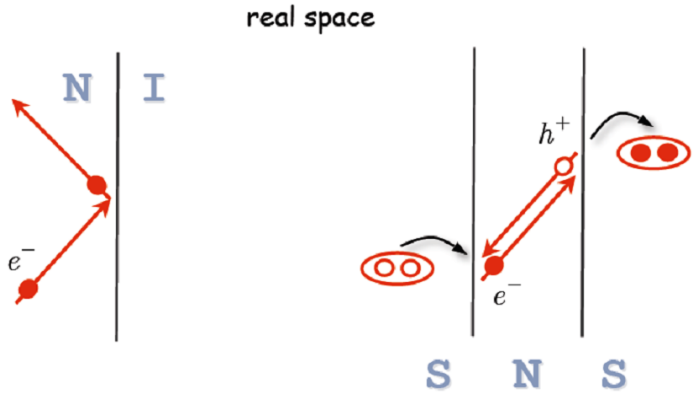

Figure 11: The left panel illustrates the normal reflection of an electron at a normal-insulating interface. The electron not having enough energy to penetrate the potential barrier created by the insulator must be reflected back into the normal metal as an electron. The right panel illustrates Andreev reflection at the interface between the normal metal and the superconductor. In this diagram the electron not having enough energy to penetrate the potential barrier at the interface is reflected as a hole back into the normal metal. In order for charge to be conserved, two electrons must be present in the superconductor.

single Andreev reflection. A similar result occurs if we consider an SNS system in which a potential V, that is less than $\frac{2\Delta}{e}$ yet greater than $\frac{\Delta}{e}$, is applied across the superconductors.

If, on the other hand, the potential applied across the superconductors is less than $\frac{\Delta}{e}$, we would expect for a Cooper pair to be created in the right superconductor and a hole to be reflected into the metal. As the hole moves towards the left superconductor, it will gain energy equal to eV (as opposed to an electron that was reflected which would lose an equivalent amount of energy). If the energy of the hole that strikes the left superconductor is less than $\frac{2\Delta}{e}$ then Andreev reflection will occur at this interface. This will result in a Cooper pair whose constituent particles are holes. Meanwhile back in the normal metal, an electron will be reflected and gain an amount of energy eV as it approaches the right superconductor. This process will be continued until the energy of the charge that reaches the right superconductor has an energy that is permitted in the superconductor (*i.e.*, $E > \frac{2\Delta}{e}$).

We note that every time the electron (or hole) traverses the normal metal, an amount of energy eV is gained. Therefore the number of trips (n) required for an electron (or hole) to gain enough energy to enter the superconductor must satisfy the expression $neV = 2\Delta$.

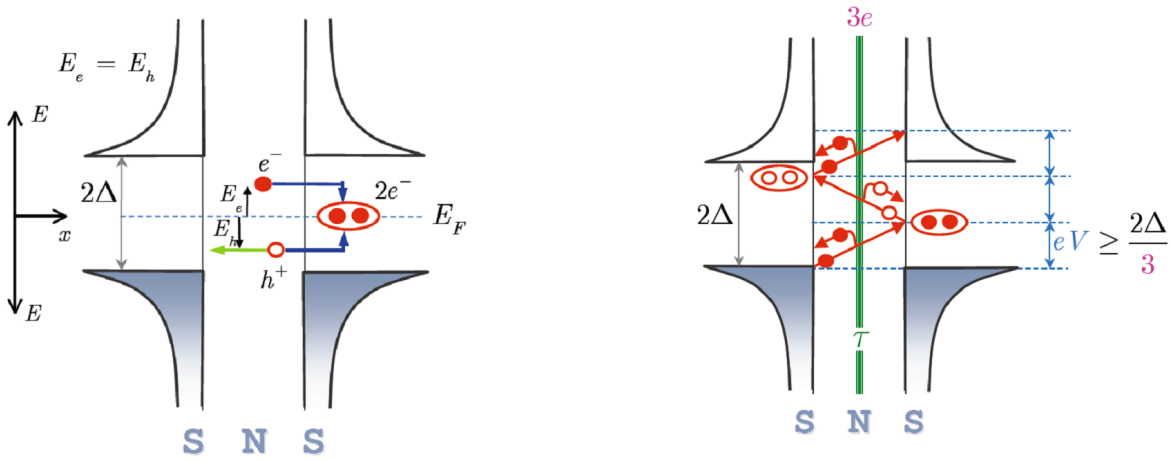

Figure 12: The left panel illustrates a single Andreev reflection. The electron, which has an energy E that is greater than the Fermi energy but less than the gap energy Δ, is Andreev reflected at the surface. A Cooper pair is formed in the superconductor and a hole having an energy E below the Fermi level is reflected back into the normal metal. The diagram on the left panel illustrates multiple Andreev reflection allowing for an electron of initial inadequate energy to traverse the energy gap 2Δ. Since the electrons' initial energy is lass than that of the Fermi level, this charge will need to be reflected multiple times before gaining enough energy to enter the superconductor. This explains the periodic ($V = \frac{2\Delta}{ne}$, where n corresponds to the number of trips across the normal region the charge made before entering the superconductor) steps that create the junctions subgap structure.

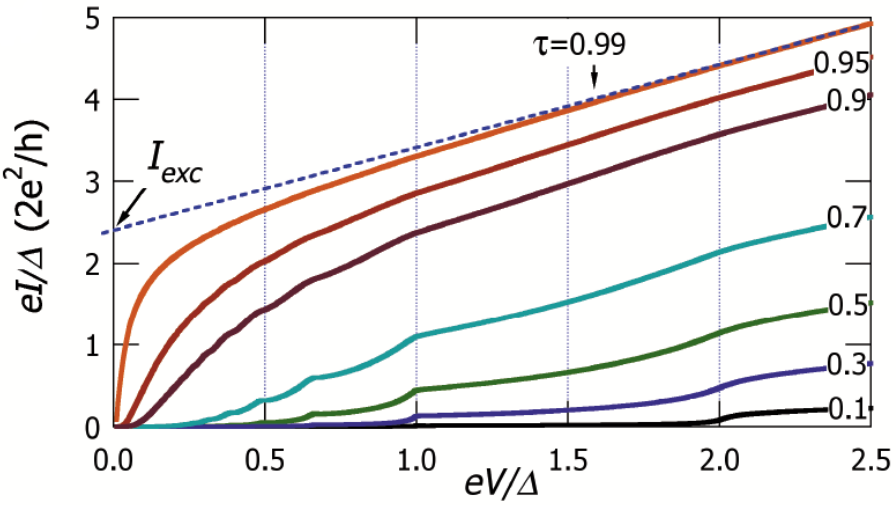

Figure 13: A computer simulation of the IV characteristics of a junction for various transmission coefficients of a single channel are plotted. As the transmission coefficient increases, the junction's character begins to resemble that of the ballistic regime, as can be seen by its approach to the dotted line.

As a result we would expect to see increases in the current at intervals of $V = \frac{2\Delta}{ne}$. We call the non-linearities in the IV graph that results from these steps the *subgap structure* [145].

1.5.3 Mesoscopic PIN Code

The nonlinearity present in the subgap structure may be used in order to determine the mesoscopic PIN code of a sample[162]. As mentioned earlier, the number of channels of a sample corresponds to the valence of the atom used to make up the contact material[160]. Hence the periodic table may be used to determine the number of channels present in a specific sample.

After determining the number of channels (5 for niobium) for the sample, computer simulations may be made using a FORTRAN code created by Ake Ingerman and John Lantz at Chalmers University, which uses a model created by Bratus', Shumeiko and Wendin for a BCS superconductor. Simulations for all possible combinations of 5 transmission coefficients, ranging from $\tau_i = 0.001$ to $\tau_i = 0.999$ in intervals of 0.001 (*i.e.*, 1000 possible values for a single transmission coefficient) may be performed.

Simulated IV characteristics for an individual channel with transmission coefficients ranging from 0.1 to .99 are illustrated in fig. 13. In order to compare experimental results

with those obtained from the FORTRAN simulations, the current and voltages must be expressed in the dimensionless form used in the simulations. Thus the experimental voltages must be scaled by a factor of $\frac{e}{\Delta}$ and the current by a factor of $\frac{e}{G_0\Delta}$ as illustrated in fig. 14.

In order to determine the value of Δ, the BCS expression $\Delta = 1.76k_bT_c$[174] may be used, where T_c is the critical temperature of the sample. Using the FORTRAN code the IV characteristics may be simulated at different temperatures in order to minimize the effects of thermal broadening on the subgap structure. Once the computer simulated results are generated, a best fit plot may be performed in order to determine which simulated mesoscopic PIN code best fit the experimental results[63].

Now that the experimental subgap strucure of a contact may be used in order to unambiguously determine the mesoscopic PIN code of a sample, the effects of electromagnetic radiation on the contact must be considered. This will lead us into the crux of our research, namely Josephson radiation and single molecule spectroscopy.

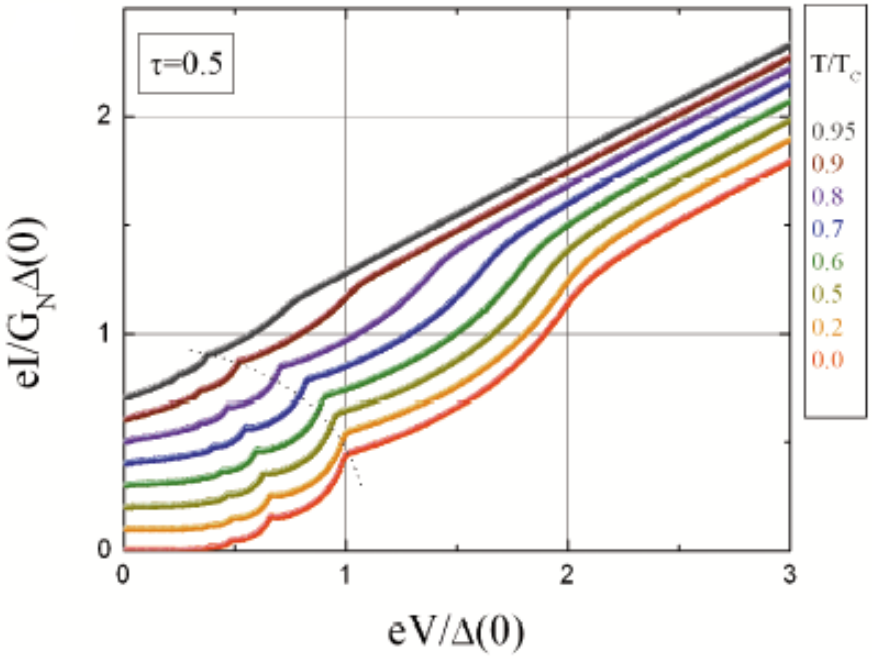

Figure 14: A computer simulation of the IV characteristics of a junction for various transmission coefficients of a single channel are plotted along with their temperature dependence. At the low temperatures the non-linear characteristics are dominate, but as the critical temperature is approached (T_c) the plot approaches that of an ohmic material, signifying that the superconducting effects are negligible.

CHAPTER II

JOSEPHSON RADIATION

Before investigating the response of the subgap structure to external electromagnetic radiation, we must revisit the Josephson effect. It was introduced in the previous chapter as a means of showing that superconducting current is a result of a coherent superconducting condensate, as opposed to individual Cooper pairs.

The DC Josephson effect, which related the current density across the Josephson junction to the phase difference between the two superconductors, can be expressed in terms of current (as opposed to current density) as:

$$I = I_c \sin(\delta), \tag{57}$$

where I is the superconducting current, and I_c is the critical current ($I_c \approx 0.15mA$) of the DC Josephson effect. This implies that if the current measured through the junction is less than the critical current (I_c), charge is being transferred exclusively by the superconducting current (*i.e.*, Cooper pairs) as opposed to quasi-particles. As a result of this, the voltage across the junction does not drop until the current passing through exceeds the critical current.

The Josephson phase-voltage relation:

$$\dot{\delta} = \frac{2e}{\hbar} V, \tag{58}$$

implies that by applying a voltage (V) across the junction, a change in the relative phases of the two superconductors will result. This change in relative phase between the two superconductors will alter the current as a consequence of the validity of equations (57) and (58).

If a constant voltage V is applied across the junction, the Josephson phase-voltage

relation may be expressed as:

$$d\delta = \frac{2e}{\hbar} V dt, \tag{59}$$

which implies:

$$\delta = \omega_J t, \tag{60}$$

where ω_J ($= \frac{2eV}{\hbar}$) is the Josepshson frequency. Thus the superconducting current can be expressed as:

$$I = I_c \sin(\omega_J t), \tag{61}$$

when a constant voltage V is applied across the junction. This implies the current across the junction oscillates with a frequency ω_J, which will normally fall in the gigahertz range due to the small value of Planck's constant.

As is true with any active circuit element carrying an oscillating current, a corresponding radiation will be emitted. The emission ability of active elements implies that a Josephson junction may be used as a source of electromagnetic radiation that falls in the gigahertz range. An ideal microwave source is an application for which many Josephson junctions are used[24].

While the current passing through the junction effects the radiation emitted by the junction, an astute reader may ask whether radiation absorbed by the junction will in turn effect the current and moreover the IV characteristics of the junction. If the radiation does effect the subgap structure of the junction, can we relate this effect to any characteristic of the radiation?

2.1 Shapiro Steps

The zero-voltage current (I_c) of the Josephson junction is a characteristic of a given material. This, as previously mentioned, is the maximum current that can pass between the contacts without causing a potential difference to develop between the contacts. We attribute this current to Cooper pairs, as opposed to quasi-particles. Once this current is exceeded, a potential difference will develop between the contacts and charge transport, thus, cannot be exclusively attributed to Cooper pairs.

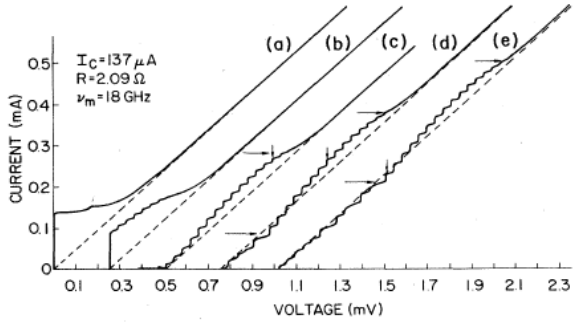

Figure 15: Experimental IV curves at 4.2K for increasing microwave powers. The dotted lines represent solutions to the RSJ model with currents (a) $I_c = 0$, (b) $I_c = 0.5$, (c) $I_c = 1.0$, (d) $I_c = 1.5$, and (e) $I_c = 2.0$. Dashed lines represent ohmic lines[183].

A similar, but not identical, analogy between the zero-voltage current of a Josephson junction and the work-function (Φ) of a metal may be contemplated. This picture may allow us to anticipate the response of the Josephson junction to external radiation. For charge to escape a given metal, a potential V must be applied such that $eV = \Phi$ (*i.e.*, $V > \frac{\Phi}{e}$). For potentials less than V, no charge will escape the metal.

The photoelectric effect showed that by shining light on the metal (*i.e.*, allowing the metal to absorb radiation) the potential needed to free electrons decreased. The difference in potential was related to the frequency of the given light and independent of that light's intensity.

Similarly we find, as illustrated in fig. 15, that the zero-voltage current of a Josephson junction decreases upon exposure to radiation. The radiation that the Josephson junction is exposed to falls in the microwave range for reasons that will be explained later. Unlike the photoelectric effect, the change in zero-voltage current is dependent on the power of the radiation.

It must be noted that two primary features of the IV characteristics of the junction change upon exposure to radiation. The first, as previously mentioned, is the decrease in the zero-voltage current. The second is the appearance of steps in the IV graph after the zero-voltage current has been exceeded. These nonlinear effects are called *Shapiro steps*.

From fig. 15e we note that there are three distinct regions of the curve after radiation of sufficient power has been applied. The first region is for large current bias and in this region,

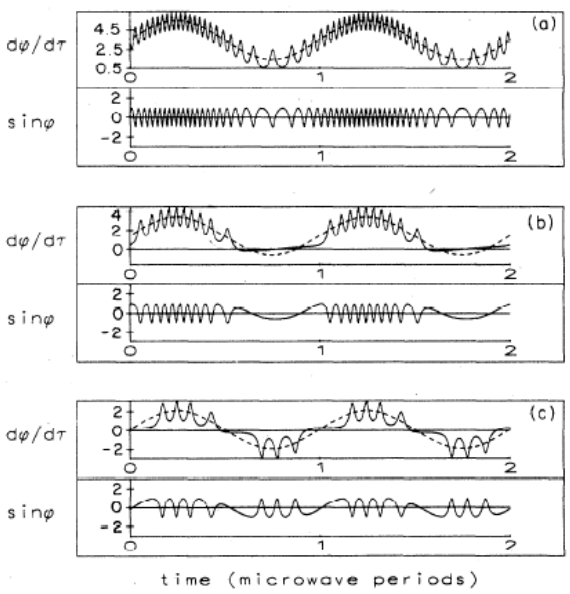

Figure 16: Time dependence of the current due to Cooper pairs ($\sin\varphi$) and the current due to some as yet to be defined source ($\dot{\varphi}$). (a) high current bias region (b) moderate current bias region and (c) low current bias region. Dotted lines represent the total current [183].

the IV curve approaches the ohmic dashed line. This portion of the graph implies that for large voltages, the system is behaving as an ohmic metal, independent of the radiation[183].

The second region, in which there is moderate current bias, contains Shapiro steps of equal magnitude. In this region the curve deviates substantially from the ohmic line and appears to be a bump in the plot. The third, low biased current, region also has Shapiro steps but, unlike the second region, these steps are aligned with the ohmic line and have differing magnitudes.

For a physical interpretation of the appearance of the three regions on the curve we resort to an adiabatic argument[2]. As was previously mentioned, currents below the zero-voltage current may be attributed to Cooper pairs. When the total current exceeds the zero-voltage current, we can be assured that the charge transport is not due exclusively to Cooper pairs. Therefore we may express the total current passing through the junction as:

$$I = I_o + I_c \sin(\delta), \tag{62}$$

where I_o is the current that is not due to Cooper pairs. It is plausible to assume that, due to the approaching of the curve to the ohmic line at large bias currents, this current should

be proportional to the voltage that develops between the contacts $V(=\frac{\hbar}{2e}\dot{\delta})$.

Figure 16 illustrates $\sin\delta$ and $\dot{\delta}$ as a functions of time, over two microwave cycles. The Cooper pair current is proportional to $\sin\delta$, and the remainder of the total current, whose source is as yet to be determined, is proportional to $\dot{\delta}$. The dashed line represents the total current passing through the junction.

We first note that as the total current increases, the wavelength of the $\sin\delta$ and $\dot{\delta}$ oscillations decreases. These oscillations are dependent on the Josephson frequency of the junction. This was defined previously as $\omega_J(=\frac{2e}{\hbar}V)$. Thus, as the voltage across the junction increases, the frequency of these oscillations also increases, resulting in the wavelength decreasing for larger total currents.

Figure 16a represents the first, large current bias, region. Since the total current never drops below the zero-voltage current in this region, contributions from both sources are made to the total current. Figures 16(b) and (c) represent moderate current bias (region II) and the low current bias (region III), respectively. It will be noted that when the total current falls below the zero-voltage current, $\dot{\delta}$ drops to zero, and the total current curve is identical to the $\sin\delta$ curve. This is in agreement with our initial assertion that the entire current, when less than the zero-voltage current, is due to Cooper pairs.

The physical interpretation of the three distinct regions of the IV graph stems from the solution of the differential equation that results from equation 62:

$$I = I_v\dot{\delta} + I_c\sin(\delta), \tag{63}$$

where I_v is the proportionality constant between I_o and the potential across the contacts. The solution of this equation will be covered in detail in section 2.3, but for the time being we merely appeal to the general properties of the equation in order to develop a picture of what forces are at work that result in the IV characteristics of the junction.

In region I the current never drops below the zero-voltage current. This implies that the voltage across the contacts is changing continuously, and there are no boundary values for our differential equation in this region. Consequently the current varies continuously (and linearly) with the voltage. This is analogous to the particle in a box where the box

has infinite width. As a result all wave solutions are permitted and the energy spectrum is continuous.

In regions II and III, the total current falls below the zero-voltage current. Therefore a boundary value condition results, namely $\dot{\delta} = 0$ for $I < I_c$. This results in only certain solutions being permitted in a given voltage range, hence the appearance of steps. This is similar to the particle in a box of finite dimension. Only waves of select wavelengths are permitted, resulting in a quantized energy spectrum.

To explain the uniformity of Shapiro steps size in region II and the lack thereof in region III, it will be noted that the $\dot{\delta}$ and $\sin\delta$ curves are out of phase by π radians. As a consequence the graph gives the impression of two current sources working against one another. This is similar to an inductor in a circuit trying to counter the electromotive force causing the current to change.

Every complete wavelength of the superconducting current curve ($\sin\delta$) corresponds to a 2π rotation of the phase difference between the two superconductors. When the total current is above the zero-voltage current, there are many such rotations, but when the total current falls below the zero-voltage current a complete 2π rotation is never experienced. The order of the Shapiro step is the number of oscillations of the superconducting current that occur during a complete wavelength of the total current. This results in the Shapiro steps having equal magnitude in region II.

In region III the total current falls below $-I_c$ and as a consequence causes the phase difference between the superconductors to experience a rotation of 2π in the opposite direction. Therefore the order of the Shapiro step is the difference between the positive and negative rotations and as a result causes the magnitude of the Shapiro steps to be non-uniform.

2.2 Fiske Effect

In the opening of Chapter 1 we mention that superconductivity is a thermodynamic phenomena characterized not only by zero resistivity but also by zero permeability. This, coupled with the results of the previous section, may cause the reader to raise the question as to the effects of an applied magnetic field on the IV characteristics of a Josephson

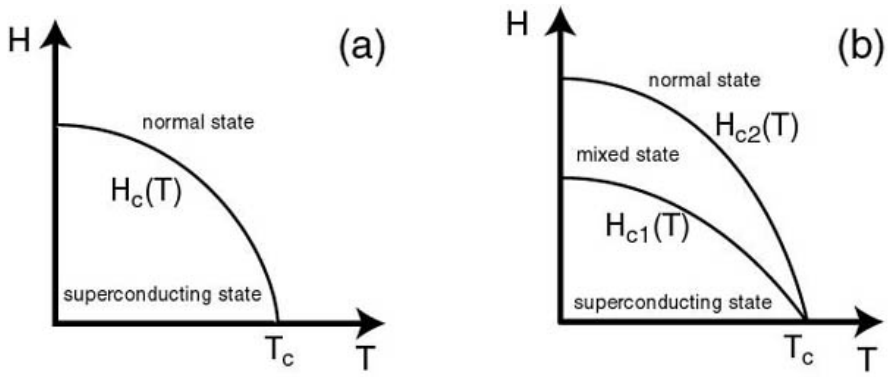

Figure 17: (a) A phase diagram of a Type I superconductor. Note how the Type I superconductor switches abruptly from the Meissner state to the normal state. (b) A phase diagram of a Type II superconductor. Note the transition from the Meissner state to the mixed state at (H_{c1}) and from the mixed state to the normal state at (H_{c2}).

junction.

Before covering the effects of an applied magnetic field on the IV characteristics of a Josephson junction, we felt it prudent to look at the effects of an applied magnetic field on an isolated superconductor in more detail. This will lead to the conclusion that a superconductor may exist not only in the normal state or the Meissner state, but also in a state that is a hybrid of the two.

2.2.1 Meissner Effect

When we first mentioned the Meissner effect (*i.e.*, the complete expulsion of magnetic flux from a superconducting metal), we neglected to mention that there is a temperature dependence. Whereas the critical temperature (T_c) was defined as the temperature at which the resistance of a metal abruptly drops to zero, the magnetic field's critical value (H_c) is the value of the applied field that will, independent of temperature, cause the Meissner effect to break down and as a result enable magnetic flux lines of sufficient magnitude to penetrate the superconductor. As the temperature of the superconductor falls below the critical temperature, the magnitude of the applied magnetic field needed to break down the Meissner effect increases, as illustrated.

We noted previously that superconductors may be divided into two groups, Type I and Type II. A Type I superconductor was characterized by an abrupt change (at the critical

temperature T_c) from the normal state in which magnetic flux was allowed to penetrate the superconductor, to the Meissner (superconducting) state in which no magnetic flux was allowed to penetrate. A Type II superconductor was characterized by a gradual change from the normal state to the Meissner state, as illustrated in fig. 2. H_{c1} is the critical value of the magnetic field that allows flux to begin to penetrate the superconductor while H_{c2} is the critical value of the magnetic field at which point the Meissner effect has collapsed resulting in complete penetration of magnetic flux through the superconductor.

Our characterization of a Type I superconductor was based on the ideal case in which the material had a demagnetization factor of zero ($n = 0$). In the case in which the material has a non-zero demagnetization, there is less of an abrupt change from the Meissner state, but rather a period of increased magnetic flux penetration until the Meissner state completely collapses. Although this phenomena would appear to blur the distinction between Type I and Type II superconductors, there is still a marked difference in the way the flux penetrates the superconductor between the normal state and the Meissner state of the two types of superconductors.

The flux penetration in Type I superconductors takes place in alternating layers. Moreover if we imagined that we had a cylindrical shaped superconductor in this hybrid state, a cross sectional view of the superconductor may look something like a clock. Where the minute divisions would be the normal regions in which magnetic flux was allowed to penetrate. Everywhere else would be the superconducting region in which no magnetic flux lines were allowed to penetrate. As the applied magnetic field is increased, we would notice the minute divisions growing longer and broader until they covered the entire clock, at that point the Meissner state will have completely collapsed.

The flux penetration in a Type II superconductor is somewhat different from that of a Type I superconductor of non-zero demagnetization. The magnetic flux penetrating a Type II superconductor is quantized, and therefore a cross sectional view would appear to contain rain drops as opposed to minute divisions[75]. Where the road to the normal state was characterized by the broadening of the minute divisions in a Type I superconductor, the path taken by a Type II superconductor would appear to be characterized by an increase in the

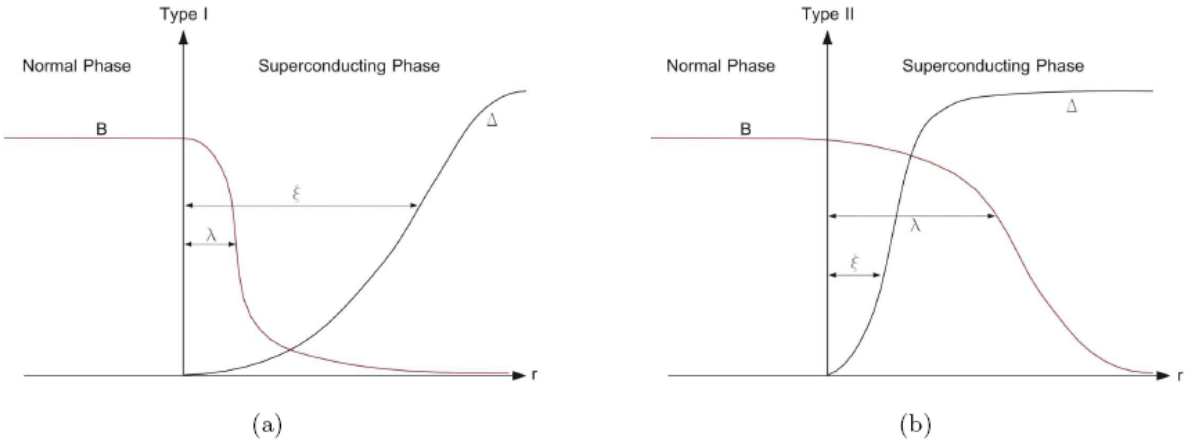

Figure 18: (a) In a Type I superconductor the magnetic field cannot penetrate deeply as indicated by the relatively small size of λ, which results in the abrupt transition to the Meissner state. (b) For Type II superconductors the penetration depth (λ) is large in comparison to (ξ) which leads to interaction with the order parameter Δ. This leads not to complete expulsion of the magnetic field in a Type II conductor, but rather to vortices in which superconductivity is suppressed.

number of rain drops, as opposed to the expansion of already existing drops. The quantum of magnetic flux (Φ_0) is $\frac{hc}{2e}$ and necessitates the introduction of two new variables, namely the penetration length λ and the length over which a magnetic field destroys superconductivity ξ.

The ratio of these two variables $(\frac{\lambda}{\xi})$ determines the extent to which a given material is a Type I or Type II superconductor. If the ratio is small (< 1), meaning that the penetration length is small in comparison to the length over which a magnetic field can suppress superconductivity, the superconductor is Type I. Consequently once the critical magnetic field has been applied, the Meissner effect completely collapses due to the large value ξ relative to the penetration length. On the other hand, if the ratio is large (> 1), then the only way change from the superconducting state to the normal state can be brought about is by increasing the magnetic field even after the onset of magnetic flux penetration.

In anticipation of analyzing the effects that an applied magnetic field has on the IV characteristics of a Josephson junction, we must investigate the effects that the ratio of penetration length to ξ has at the surface of a NS (normal-superconducting) interface. In

chapter 1 the Josephson effect was attributed to the overlap of the wave function of two superconductors in close proximity to one another. If the superconductors were too close to one another, the phases of the superconductors would lock, and the system would behave as a single superconductor. If the superconductors were too far apart, there would be no overlap of the wave functions and thus no Josephson current.

For the interface of a Type I superconductor with a normal metal, ξ is an indicator of how long it takes the order parameter Δ to reach the value it would have were the superconductor isolated. For this interface the penetration depth (λ) is small while ξ is comparatively large. This means that there is little overlap at the interface, as illustrated in fig.18 At the interface of a Type II superconductor and a normal metal, the penetration length is relatively large while ξ is comparatively small. This leads to a large overlap at the interface.

To interpret these results we must think in terms of energy. A given amount of energy (E_λ) is needed to expel the applied magnetic field over a distance λ, and an amount of energy (E_ξ) is needed to break up Cooper pairs over a distance ξ. Since E_λ is smaller than E_ξ in a Type I metal, it is energetically advantageous for a Type I superconductor to expel flux from the inside of the superconductor.

For a Type II metal, in which E_λ is larger than E_ξ, expulsion of the entire magnetic flux is not possible. Since the magnetic flux is quantized, small regions develop inside of the metal in which magnetic flux is allowed to penetrate. The density of Cooper pairs is reduced in this region and becomes zero at the very center of these *vortices*, as illustrated in fig.19.

These vortices form a triangular lattice when the Type II superconductor is in the mixed state. The transition to the normal state is accelerated by the movement of these vortices throughout the superconductor, while impurities in the superconductor act to limit the movement of these vortices and thus limit the speed of transition. This effect may also be minimized by a thermally assisted flux flow, which allows the vortices to bypass the impurities and travel somewhat unrestricted.

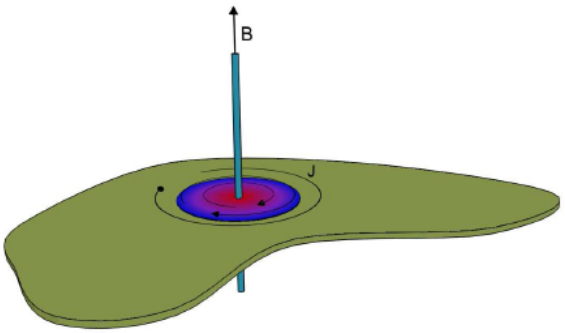

Figure 19: Schematic of the vortex that arises in a Type II superconductor after H_{c1} has been exceeded. These vortices occur when the superconductor is in the mixed state in which partial magnetic penetration takes place resulting in vortices of current.

2.2.2 Josephson Current Resonance

Having examined the effects of the magnetic field on a single superconductor and a NS (normal-superconducting) interface, we may proceed with an investigation of the effects of the magnetic field on the junction. The IV characteristics may be attributed to the interaction of the Josephson current-density waves with the electromagnetic fields inside the junction acting as a resonator.

Due to the heavy inductive loading caused by the magnetic field penetration, the electromagnetic wave is slowed between the superconducting contacts[74]. The ratio of the waves velocity to that of light is given by[170]:

$$\frac{v}{c} = (\frac{l}{\epsilon}(2\lambda + l))^{\frac{1}{2}}, \tag{64}$$

where l is the junction thickness, and ϵ is the dielectric constant.

We must note that the height of each step on the IV curve varies with the field and has the same period as the zero-voltage Josephson current. That the maximum current in a step diminishes as we pass Δ, half the the energy gap, should not come as a surprise. This is attributed to the dampening of the AC modes when the frequency becomes high enough to raise single electrons above the energy gap.

To explain these effects we must couple our previous Josephson equations with:

$$\nabla\delta = \frac{2e(2\lambda + l)}{\hbar c}(\boldsymbol{H} \times \boldsymbol{n}), \tag{65}$$

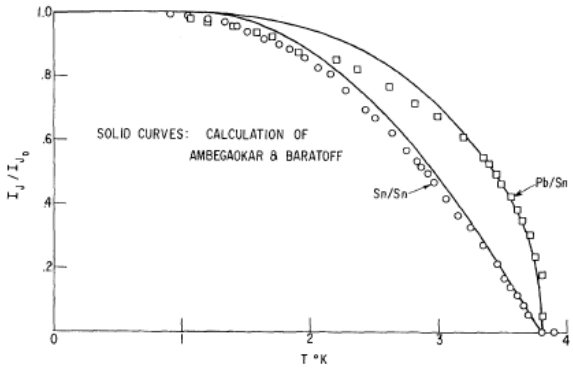

Figure 20: Temperature dependence of zero-voltage current. The circles are experimentally determined measurements of Sn/Sn and Pb/Sn zero-voltage current's temperature dependence. The solid lines represent the calculations based on Ambegaokar and Baratoff[73].

where $\boldsymbol{n}$ is the unit vector normal to the junction plane. The $\boldsymbol{H}$ can be expressed as:

$$H = H_0 + \sum_{i=1}^{\infty} H_n \sin(\frac{n\pi}{l} z) \sin(\omega_n t + \theta_n), \tag{66}$$

where ω_n is the resonant frequencies and θ_n the phases.

If the DC voltage corresponds to the resonant frequencies then multiples of the resonant frequencies will be produced by the frequency modulating effect of the Josephson's equations. If this is coupled with the boundary value conditions then an analytic solution for both the phase and DC peak current can be obtained. The actual solution would inadvertently deter us from our desired objective and will be avoided. What is important to note is the picture of the junction behaving as an open-ended resonator with modes excited by the AC Josephson effect.

2.2.3 Temperature Dependence

We noted in the previous section that the zero-voltage current is effected by the application of radiation to the junction. As evidenced from fig. 15, as the power of the radiation is increased the zero-voltage current decreases and eventually reaches zero. Similar to the magnetic field (H_c) required to completely collapse the Meissner effect, the zero-voltage current has a temperature dependence.

That this is the case is apparent by noting that the zero-voltage current is due exclusively to Cooper pairs. The density of Cooper pairs will definitely have a temperature

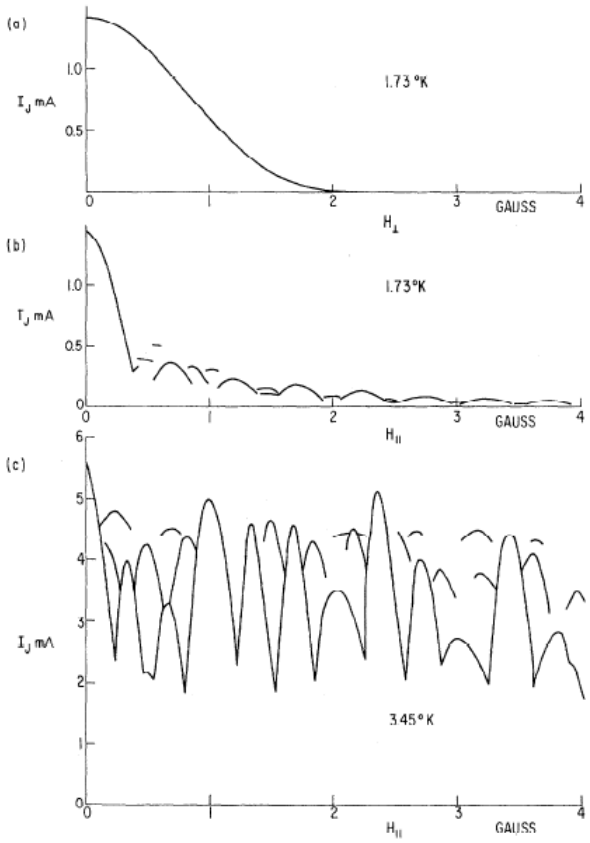

Figure 21: Zero-voltage current through superposed, parallel-strip junctions as a function of applied magnetic field in the planes of films. (a) The applied magnetic field is perpendicular to the Sn/Sn strip. (b) The applied magnetic field is parallel to the strip. (c) The applied magnetic field is parallel to the strip, and the two superconductors making up the Josephson junction are not of the same material (Pb/Sn). This results in the multi-step tunneling character of the experimental curves[73].

dependence, because increased thermal energy will cause many Cooper pairs to break into their constituent quasi-particles. This would decrease the density of Cooper pairs and therefore decrease the zero-voltage current. As a result we would expect a decrease in zero voltage current with a rise in temperature, as fig.20 illustrates.

Whereas the zero-voltage current's temperature dependence may have been anticipated, the dependence of the penetration length on temperature ($\lambda \approx \frac{1}{[1-(\frac{T}{Tc})^4]}$) may be somewhat less obvious[73]. Noting that the area of a junction is the product of twice the penetration length (λ) and the width of the strip (w), we see that there must be a temperature dependence of the area of the junction.

As was noted previously, the magnetic flux penetrating a Type II superconductor is quantized. This implies the product of the area of the junction and the applied magnetic field (ΔH) may not assume independent and arbitrary values. This lack of independence becomes more crucial when we note the periodic dependence of the zero-voltage current on the applied magnetic field, as illustrated in fig.21(b).

The magnetic flux passing through the junction is found to be temperature independent, thus we would expect for the the area under adjacent minima (ΔH) to be dependent on temperature, as illustrated in fig22. This dependence allows us the freedom of varying the cross section of the junction by altering the temperature. The magnetic flux, which is independent of temperature, may be determined by using the plot in fig.22.

2.3 Hilbert Transform Spectroscopy

Having shown the plausibility, both experimentally and from physical arguments, of external radiation effecting the IV characteristics of a Josephson junction, our aim is now to determine the relation between the external radiation and the change in IV characteristics of the junction. Our technique will involve solving the differential equation arising from the resistive-shunted junction model for our system, which allows us to relate the current across the junction to the spectrum of the absorbed radiation. The predictions made by this model allow for computer simulations which are in excellent agreement with experimental results.

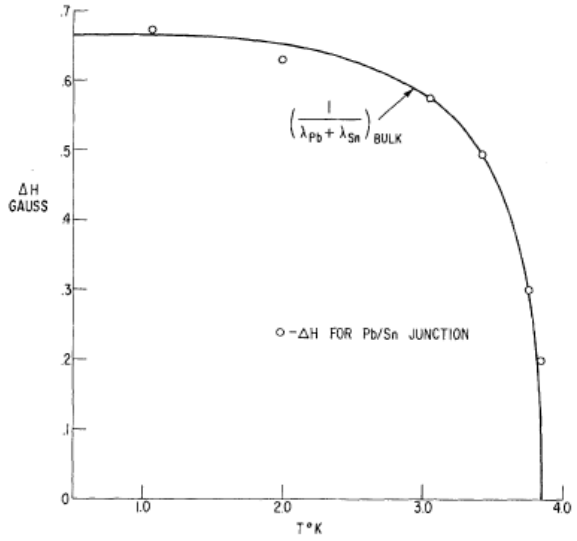

Figure 22: Temperature dependence of magnetic field intervals ΔH between maximum zero-voltage current. The magnetic flux passing through the junction is found to be temperature independent, which, when coupled with the relation of flux to magnetic field an area, implies (ΔH) should have a temperature dependence[73].

2.3.1 Current Components

As was mentioned previously, if the voltage drop across the contacts of a Josephson junction remains at zero, then we can be assured that the current passing though the contacts is due, exclusively, to superconducting current (*i.e.*, Cooper pairs). The same can be said if the temperature of the Josephson junction is kept at absolute zero.

If, on the other hand, either of these requirements is not met, we must attribute the current passing through the contacts to sources other than just Cooper pairs. These sources should be familiar to the reader, for they are not exclusive to superconductivity, but arise in normal metals as well.

2.3.1.1 Normal Current

If the temperature of the system is above absolute zero, yet less than the critical temperature (T_c) of the material, then some of the Cooper pairs will break into their constituent quasi-particles. This is due to the thermal motion of the charge carriers, whose energy is $k_B T$. These quasi-particles make up what is known as the normal current (I_n).

If the temperature of the system is close to the critical temperature of the material,

then the vast majority of the Cooper pairs will split into quasi-particles, resulting in the majority of the charge transfer being due to normal current as opposed to superconducting current. This is due to the large value of $k_B T_c$ in comparisons to the energy gap (2Δ) of the material.

If this occurs the IV characteristics of the material will resemble that of a normal ohmic metal. As a consequence we obtain a straight line, whose slope is equal to the normal conductance, for the IV graph, since the material now obeys Ohm's Law. The normal current may thus be expressed as:

$$I_n = \frac{V}{R}. \tag{67}$$

The same effect, regardless of the temperature of the system, is observed if the voltage applied across the contacts is greater than $\frac{2\Delta}{e}$. In this case, a Cooper pair in one superconductor is separated, and one of the resulting charges travels across the contacts. A straight line for our IV graph is obtained as before.

2.3.1.2 Displacement Current

If the voltage (V) across the junction is changing with respect to time, we would expect the electric field between the contacts to be changing as well. This changing electric field causes what Maxwell termed a displacement current (I_d).

The displacement current will be proportional to the change in voltage across the contacts. We call this proportionality constant the capacitance of the junction. Therefore the displacement current may be expressed as:

$$I_d = C\dot{V}. \tag{68}$$

If the frequency at which the system is driven is less than the plasma frequency ω_p ($= \frac{2eI_c}{\hbar C}^{\frac{1}{2}}$), then the displacement current is less than the superconducting current[118]. If the frequency at which the system is driven is less than $\frac{1}{RC}$, then the displacement current will be less than the normal current.

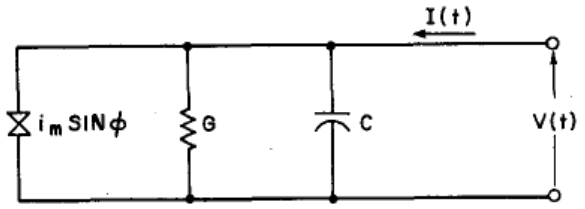

Figure 23: Equivalent circuit of a weak-link device. The junction is loaded by a shunt capacitance such as might by found in a shunted mechanically controlled break junction. The circuit is driven by a current source with a high AC impedance[132].

2.3.1.3 Fluctuation Current

The final component of current results from the "noise" that is present in all circuits. This is accounted for by the addition of the fluctuation current (I_f).

This term accounts for noise resulting from external agencies such as radio and television broadcast, electric power lines, *etc.* The fluctuation current also takes into account internal noise arising from the normal current. Since the normal current is dissipative, unlike the superconducting and displacement currents, thermal noise and shot noise are a necessary consequence.

Having introduced all the components of current present in a Josephson junction, we must now investigate the basic equations of a Josephson junction. These equations coupled with a model of the system will allow us to develop a vivid picture of the Josephson junction and its interaction with electromagnetic radiation.

2.3.2 Resistive-Shunted Junction Model

As was previously mentioned, the current across a Josephson junction can be attributed to superconducting current (Cooper pairs), normal current (quasi-particles) and displacement current. In order to properly investigate the junction, we employ the resistive-shunted junction model, as illustrated in fig.23. Note that this model is valid only in a small temperature range below the critical temperature. The displacement current will be neglected due to our exclusive use of point-contact junctions which, as a consequence, have a low contact capacitance[3]. Even though the current may be driven at high frequencies, the combined effect (*i.e.*, displacement current) is negligible (see Appendix C). Our basic equations for a

Josephson junction are:

$$\frac{d\delta}{dt} = \frac{2e}{\hbar}V, \tag{69}$$

and

$$I + I_f = I_c \sin(\delta) + I_n. \tag{70}$$

The previous equation may be expressed as:

$$I + I_f = I_c \sin(\delta) + \frac{V}{R}, \tag{71}$$

where R is the resistance of the junction in the normal (non-superconducting) state. Note that the latter equation accounts for the superconducting current (I_c), the normal current ($\frac{V}{R}$), and the fluctuation current (I_f). A simulation of the IV characteristics based on this model is illustrated in fig.24.

These relations are better expressed in a dimensionless form by introducing the the variables:

$$i = \frac{I}{I_c}, \tag{72}$$

$$\xi = \frac{V}{V_c}, \tag{73}$$

$$\tau = \omega_c t, \tag{74}$$

where V_c ($= I_c R$) is the characteristic voltage, whose maximum value is 3mV for typical superconductors, and ω_c ($= \frac{2eV_c}{\hbar}$) is the characteristic frequency. Our first primary relation may now be expressed in the dimensionless form:

$$\frac{d\delta}{d\tau} = \xi. \tag{75}$$

This relation, coupled with our dimensionless variables, allows us to express our second primary relation as:

$$i + i_f = \sin(\delta) + \xi. \tag{76}$$

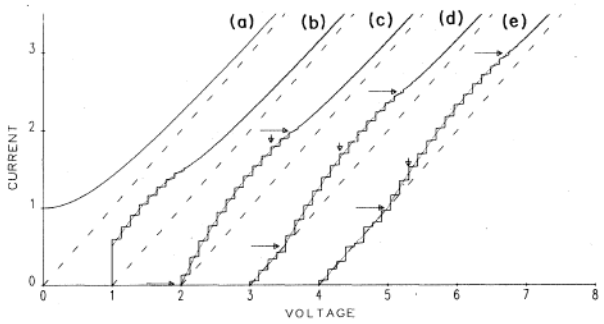

Figure 24: Numerical IV curves for increasing microwave currents. Solid lines represent solutions of the RSJ model whereas dotted lines represent adiabatic approximation solutions. Dashed lines represent ohmic lines. $(a)I_c = 0$ $(b)I_c = 0.5$ $(c)I_c = 1$ $(d)I_c = 1.5$ $(e)I_c = 2$. The large arrows indicate the DC current boundaries while the small arrows highlight the decrease of the DC current position of a stable step[183].

If our system is operated in the current-driven mode (*i.e.*, direct current through the junction is ensured), then the solution for our primary equations is[132]:

$$\bar{i} = sgn\bar{\xi}\sqrt{\bar{\xi}^2 + 1}, \tag{77}$$

where $\bar{\xi}$ is the time averaged biased voltage. This results in an IV graph with nonlinear characteristics, as illustrated[95].

The plausibility of an external radiation source causing a change in the time averaged current ($\bar{i}$) is hinted at in this chapter's introduction, and a physical interpretation is introduced in the subsequent section. Our question as to the relation of this change in current and the radiation will require a technique of reverse engineering (*i.e.*, by looking at the response we will determine the cause).

We will first assume that an additional monochromatic external current $\widetilde{i}(\tau)$ at a frequency of ω is supplied to the junction. The change in current that results from this addition is given by:

$$\Delta\bar{i}(\xi,\omega) = \frac{\widetilde{i}^2}{8\widetilde{i}\widetilde{\xi}}[\frac{\widetilde{\xi}+\omega}{(\widetilde{\xi}+\omega)^2+\gamma^2} + \frac{\widetilde{\xi}-\omega}{(\widetilde{\xi}-\omega)^2+\gamma^2}], \tag{78}$$

where γ is the fluctuation induced line width of the Josephson oscillation[166]. If as opposed to a monochromatic external current, we apply an ac current with a spectral density $H_i(\omega)$, the current response will be:

$$\Delta\bar{i}(\xi) = \int_0^\infty d\omega\Delta\bar{i}(\xi,\omega), \tag{79}$$

which as a result of our previous equation may be written as:

$$\Delta\bar{i}(\xi) = \int_0^\infty d\omega \frac{\widetilde{i^2}}{8\widetilde{i}\widetilde{\xi}}[\frac{\widetilde{\xi}+\omega}{(\widetilde{\xi}+\omega)^2+\gamma^2} + \frac{\widetilde{\xi}-\omega}{(\widetilde{\xi}-\omega)^2+\gamma^2}]. \tag{80}$$

This may be readily expressed in a more convenient form as:

$$\Delta\bar{i}(\xi) = \frac{\pi}{8\widetilde{i}\widetilde{\xi}}[-\frac{1}{\pi}\int_{-\infty}^{\infty} d\omega H_i(\omega)\frac{\omega-\widetilde{\xi}}{(\omega-\widetilde{\xi})^2+\gamma^2}], \tag{81}$$

where we make note of the fact that the term in brackets (as $\gamma \to 0$) is the Hilbert transform of the spectral density $H_i(\omega)$.

This implies that by applying a reverse Hilbert transformation on the change in current we can determine the spectral density of the ac current. If we allow for the introduction of the function $u(\xi)$ such that:

$$u(\xi) = \frac{8}{\pi}\widetilde{i}\widetilde{\xi}\Delta\bar{i}(\xi), \tag{82}$$

we may express the spectral density of the ac current as:

$$H_i(\omega) = \frac{1}{\pi}P.V.\int_{-\infty}^{\infty} d\xi \frac{u(\xi)}{\xi-\omega}, \tag{83}$$

therefore obtaining the spectral density of the ac current by performing a Hilbert transformation on the function $u(\xi)$, which is related to the IV response of the circuit to ac current[166].

For coupling of external radiation with a Josephson junction, antennas usually are employed. If the transfer function of the antenna is $K(\omega)$, then the relation between the ac current spectral density $H_i(\omega)$ and the spectrum of the electromagnetic radiation $S(\omega)$ is:

$$H_i(\omega) = |K(\omega)|^2 S(\omega). \tag{84}$$

Thus we can relate the spectrum of the absorbed electromagnetic radiation to the change in current of the Josephson junction, by the relation:

$$S(\omega) = \frac{1}{|K(\omega)|^2}\frac{1}{\pi}P.V.\int_{-\infty}^{\infty} d\xi \frac{u(\xi)}{\xi-\omega}. \tag{85}$$

Although the previous equation sheds much light on the apparently complicated procedure of recovering the spectrum of electromagnetic radiation from the subgap response of

a Josephson junction, we felt it may be advantageous to sum up the procedure in words. The technique used would be to (a) determine experimentally the IV plot of the Josephson junction in the absence of external radiation, (b) allow the junction to absorb radiation and determine the new IV plot, (c) plot the difference between the IV curves, (d) perform a Hilbert transformation on the plot from part (c) to determine the spectral density of the current, and finally (e) divide the resultant spectral density by the transfer function squared of the antenna in order to determine the spectrum of electromagnetic radiation.

CHAPTER III

EXPERIMENTAL ENVIRONMENT

To this point we have covered the theoretical foundations of superconductivity, the Josephson effect, and Hilbert spectroscopy. That these theories were valid was shown by giving experimental results along with explanations as to how these results verify, or could be explained by, the previously developed theory. No mention, as of yet, has been made as to how these experimental results were obtained. This chapter seeks to remedy this discrepancy.

The results that have been presented thus far have been in the form of plot curves. Either conductance vs. contact elongation, current vs. voltage (IV), current vs. temperature, *etc.* For each of these experiments a means of maintaining a mechanically steady separation between the tips is paramount. For example, in fig. 9 the separation between contacts is measured in nanometers. Any technique used to carry out the conductance measurement must be able to keep this separation between contacts stable to within at least a tenth of a nanometer.

That we are investigating superconducting phenomena implies that these experiments must also be conducted in an environment that is below our metal-of-interest's critical temperature ($T_c = 9.3$K for niobium). We must be able to make measurements of conductance (or similarly resistivity) and voltage. Although not yet mentioned, differential conductance ($\frac{dI}{dV}$) along with the second derivative ($\frac{d^2I}{dV^2}$)[28] must be measured in the previously described experimental environment. The latter due to its being directly proportional to the Eliashberg's[92] form of electron-phonon interaction therefore allows a measurement of the phenomena discussed in chapter 1 that was responsible for Cooper pairs.

The stability requirement is fulfilled by using a mechanically controllable break junction (MCBJ). This coupled with a measuring technique termed a four contact point, will allow us to fulfil the other requirements. Thus we start this chapter with a description of the mechanically controllable break junction[138, 141].

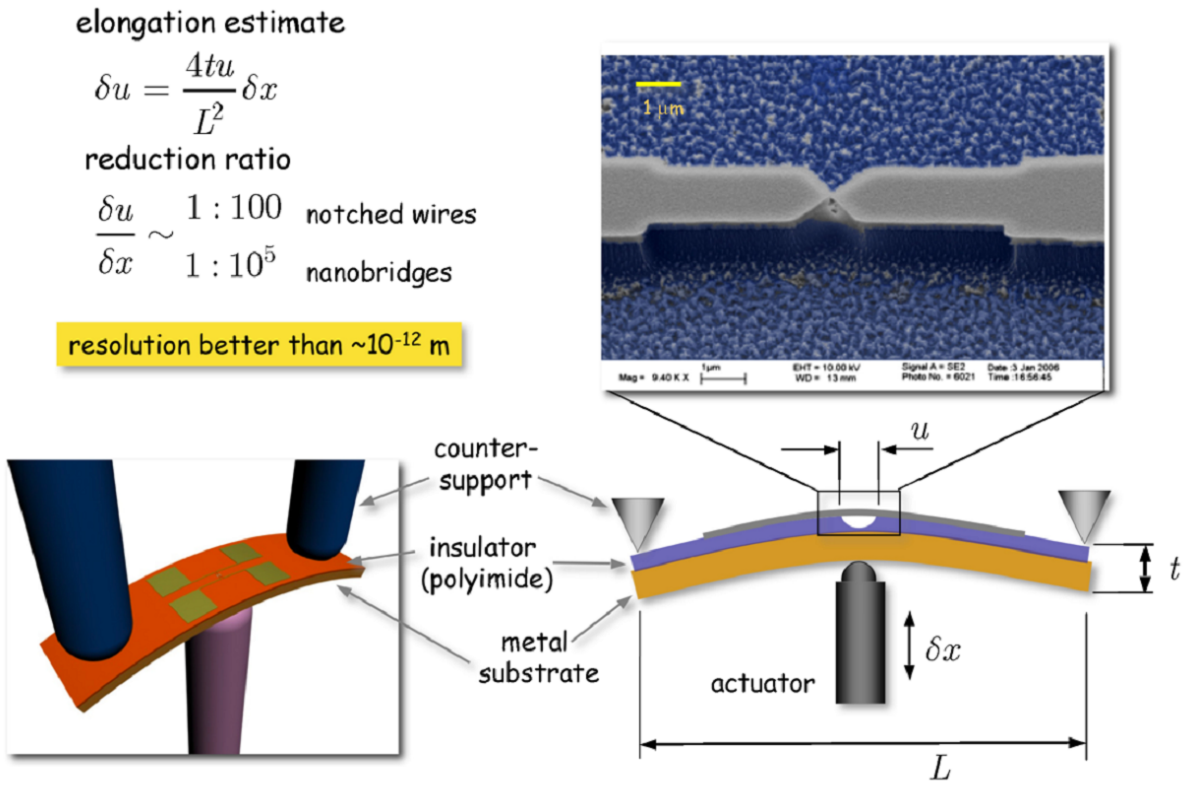

Figure 25: A schematic setup of a mechanically controllable break junction along with a colorized electron micrograph of a fabricated sample is illustrated. The flexible substrate is placed in a three point contact. The point contact is elongated upon actuating the piezo. The elongation estimate gives an approximate relation between the elongation of the piezo and the contact separation.

3.1 Mechanically Controllable Break Junction

A myriad of techniques have been developed to create atomic point contacts (*i.e.*, scanning tunneling microscope, chemical anodization of notched wires, spear-anvil technique, *etc.*). However due to reasons such as lack of mechanical rigidity or sample contamination all of the these techniques have proved inadequate to make reproducible measurements of the IV characteristics of the contact for an extended period of time.

The technique most adequately fitting for our experimental requirements, mechanical rigidity being paramount, is that of a mechanically controllable break junction. This technique consist of a metallic bridge clamped to an elastic substrate that is suspended over a ravine that is a few micrometers in depth and across, as illustrated in figure 25. The

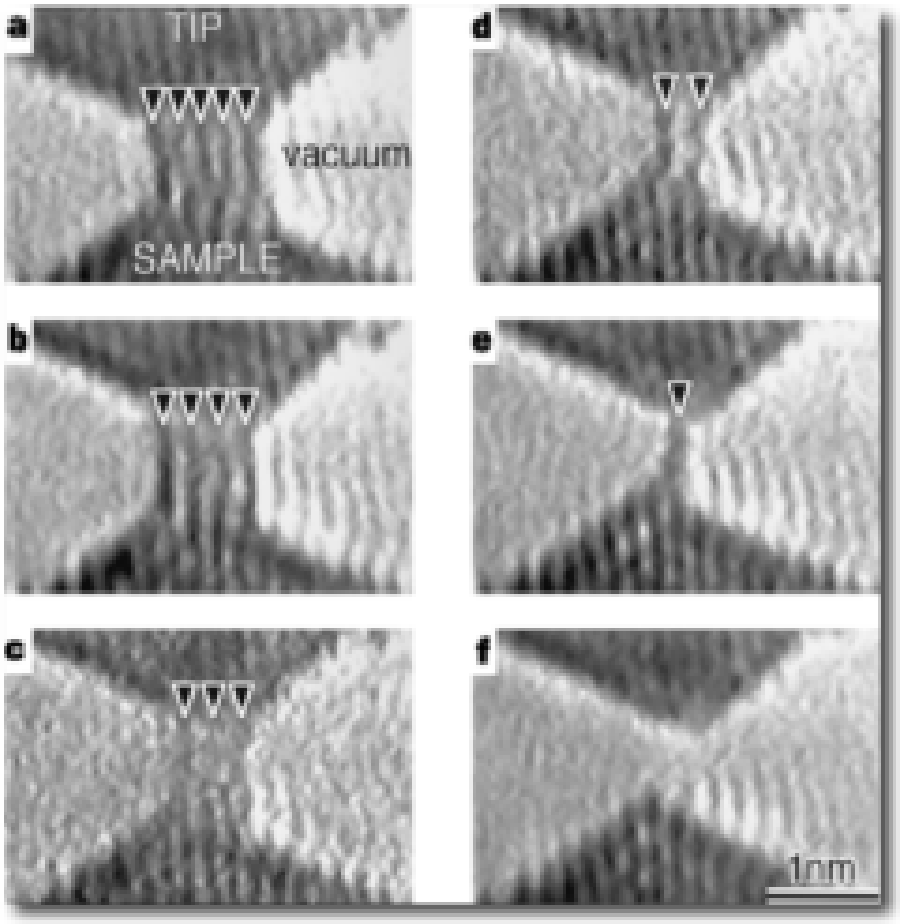

Figure 26: Direct high-resolution transmission electron microscope image of a niobium tip pulling away from a gold substrate. The image illustrates the thinning of the nanowire starting from 5 linear threads of gold until the contact is completely broken[146].

constriction at the center has a diameter of approximately 100nm.

In order to obtain the point contacts so essential to our experiments, the substrate is bent. Initially many atoms may be clustered together between the contacts, but as the substrate is bent continuously, the point will be reached where a single atom is between the contacts. This is similar to fig. 26, which is a high resolution transmission microscope image of the thinning of a nanowire courtesy of Professor Landman[111].

Many times the experiments are conducted in a reverse order in which the contact is broken and slowly brought back together until there is (a) a single atom between the contacts and (b) the contacts are close enough to one another for the Josephson effect to be observed. When the contact between the two electrodes is broken, the conductance vs.

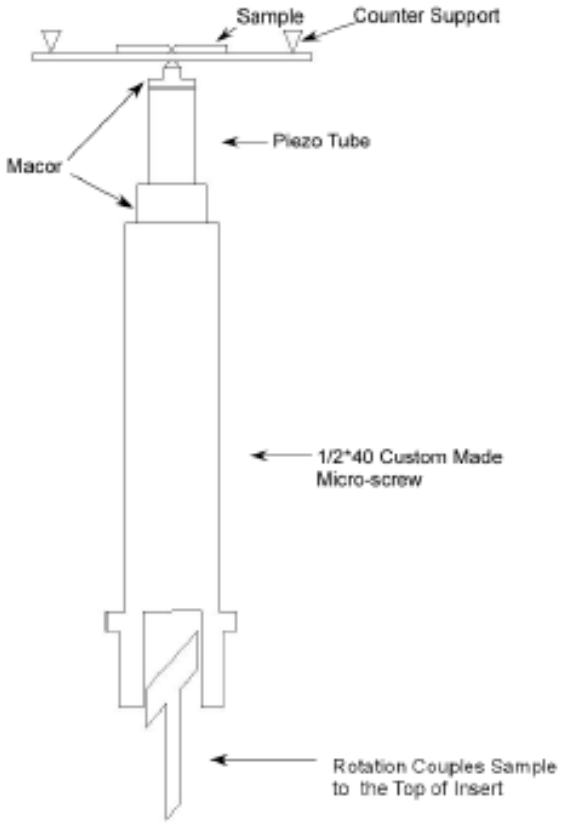

Figure 27: Schematic (sideview) of the bending system. Inside of the vacuum chamber the sample can be adjusted by the 1/2"40 custom made microscrew. In order to insure that the actuator does not jam after cryogenic temperatures have been reached the screw is brass while the nut is stainless steel. The piezo tube is used in order to insure that the bending of the substrate is not only exceedingly small, but also reproducible and controllable.

elongation plot indicates tunneling occurs, as would be expected from quantum mechanics. These results are obtained whether the experiment is conducted in the traditional order or in reverse.

A piezo actuator is used in order to insure that the bending of the substrate is not only exceedingly small, but is also reproducible and controllable[47]. The actuator allows the contact to transition from the bulk point contact regime to that of an atomic point contact, and once contact is broken, into that of the tunneling regime.

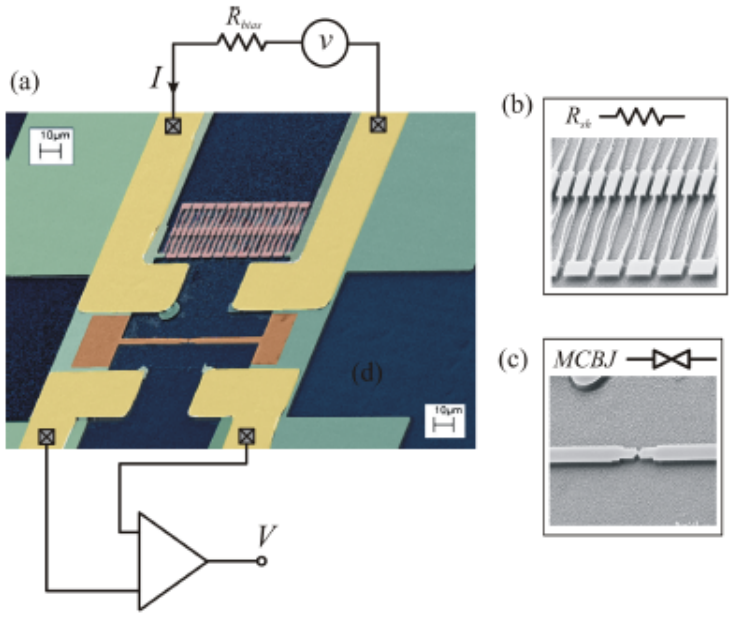

Figure 28: (a) Top view SEM image of a Ta shunted Nb mechanically controllable break junction with augmented measurement setup. The dark blue color represents the insulating thin polyimide film, the green indicates tantalum and niobium films, the brown shows the niobium contacts, while the red is the tantalum shunt. (b) Isolated Ta shunt. (c) Isolated Na junction.

3.1.1 Shunted Mechanically Controllable Break Junction

The mechanism responsible for the Josephson current was the phase difference ($\Delta\varphi$) between the two superconductors, but a direct measurement of this phase difference is not possible using a mechanically controllable break junction. In order to determine the current phase relationship, a resistive shunt must be added to the junction as illustrated in fig. 28.

The presence of the shunt allows measurement of the current phase relationship of the junction, but it does not leave the IV characteristics of the junction unaffected. The spectrum of multiple Andreev reflections was affected and resulted in a shifting in the voltages of the sub gap structure[52, 50]. Despite these effects, useful measurements were still able to be made.

In order for the resistive shunt to function properly, it must be made of a material different from that of the junction. Tantalum was used for the shunt because of its ability to satisfy a dual purpose. If the temperature is kept lower than the critical temperature of

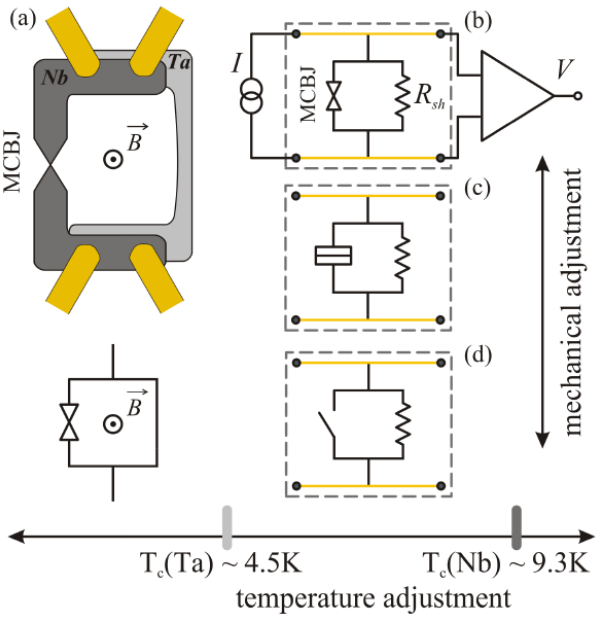

Figure 29: Schematics and operating principle of the circuit. (a) The device is made of two superconducting materials with different transition temperatures. (b) Resistively shunted junction configuration with the mechanically controllable break junction in contact mode and the shunting segment in the normal state. (c) Stretched mechanically controllable break junction in tunneling mode allows measurement of the superconducting gap of the junction material. (d) Further stretching yields the broken junction.

niobium, but higher than that of tantalum, then the tantalum will act as a shunt allowing measurement to be made of the phase current relation of the junction.

If, on the other, the temperature is below the critical temperature of niobium and tantalum, then the system behaves like that of an RF SQUID. This can be seen by comparing fig. 29 with the resistor shorted to fig. 30 of a DC SQUID. Coupling the single junction to an inductor produces an RF SQUID.

(Brief note: SQUID is an acronym for a Superconducting QUantum Interference Device. The RF SQUID consists of a single junction interrupting a superconducting loop, coupled to the inductor of an LC-tank circuit. The period of oscillation of the circuit is equal to that of the magnetic flux through the superconducting loop, which must be quantized as discussed in previous chapters.)

Having discussed the functioning of a mechanically controllable break junction and its shunted counterpart, the next step is describing how these junctions are created. It must

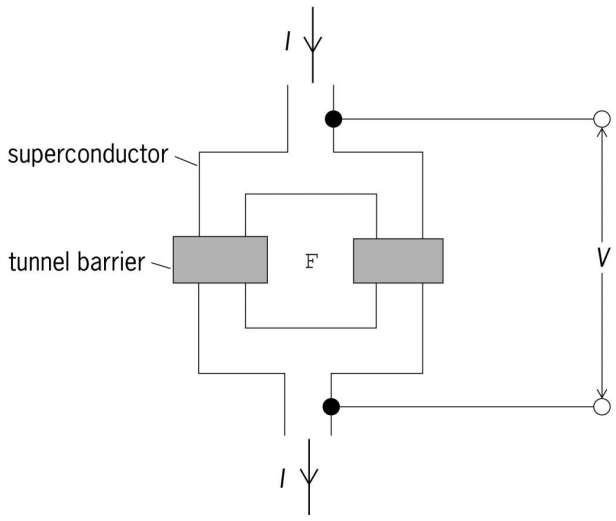

Figure 30: DC SQUID with an inclosed magnetic flux. The DC SQUID consists of a junction interrupting a superconducting loop. The circuit in figure 29 acts as an RF-SQUID when the temperature of the sample is below the critical temperature of both niobium and tantalum.

be noted that the design and fabrication of the samples is as much an art as it is a science. Therefore strict adherence to the following steps will inevitably produce samples of sub par quality initially. This may be due to sample contamination, overexposure, or a number of any of the steps that may not go perfectly.

3.2 Fabrication Of MCBJ

In the fabrication of the mechanically controllable break junction, bronze is used as the substrate material. This choice is due to the flexibility of bronze over that of silicon.

Starting with a 25μm thick by 50mm diameter phosphor bronze disc, an insulating layer was added in order to separate the ground plane from the device layer and to planarize the surface. This was accomplished by spinning a coat of VM652 adhesion promoter onto the wafer followed by spinning and curing a 2μ layer of polyimide (PI2610).

Next, a 150 nm layer of niobium is magnetron sputtered onto the sample using an *in situ* cold trap to reduce the amount of contaminants, including water, in the vacuum chamber. Evaporation was avoided due to the high melting point of niobium as well as sputtering's ability to limit the amount of radiation incident on the oxide layer.

After sputtering, Shipley 1813 photoresist was spun onto the sample, baked, and then

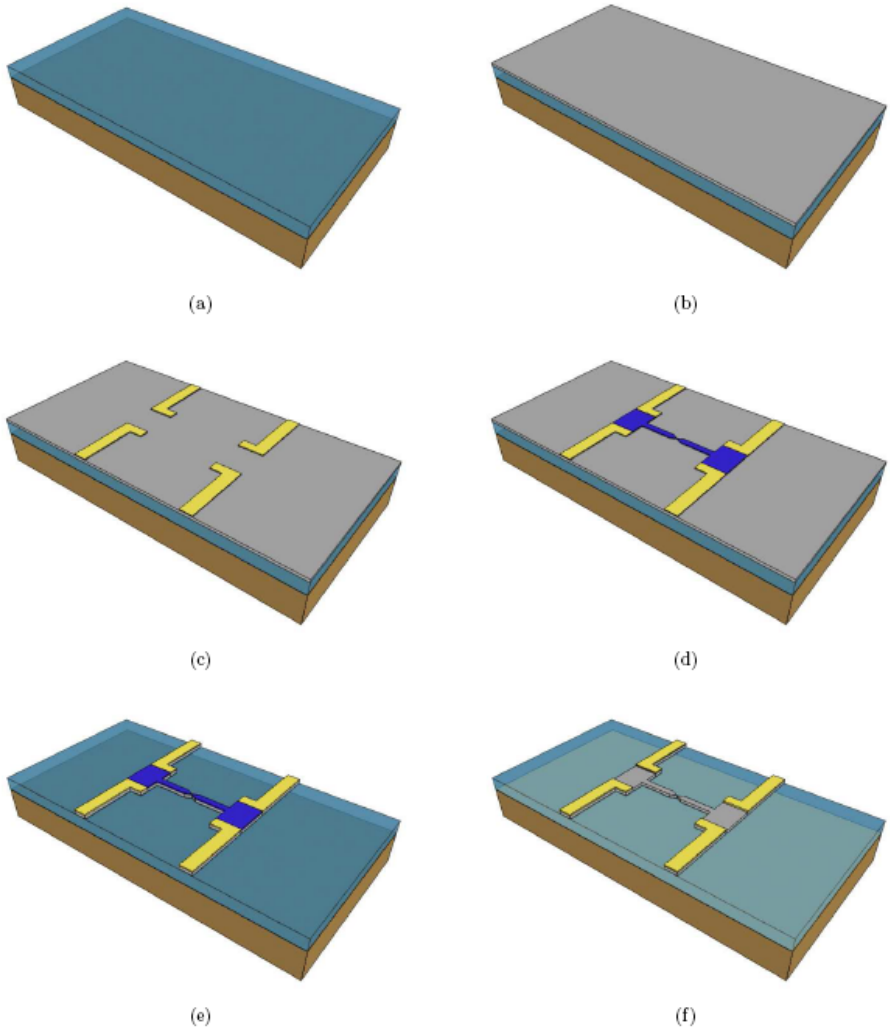

Figure 31: Schematic of the fabrication process of a mechanically controllable break junction. (a) Deposit insulating polyimide layer, (b) sputter Nb onto wafer, (c) pattern Au contact pads, (d) use e-beam lithography to pattern Al etch mask, (e) anisotropically dry etch Nb, (f) remove etch mask and isotropically dry etch the polyimide to free the bridge.

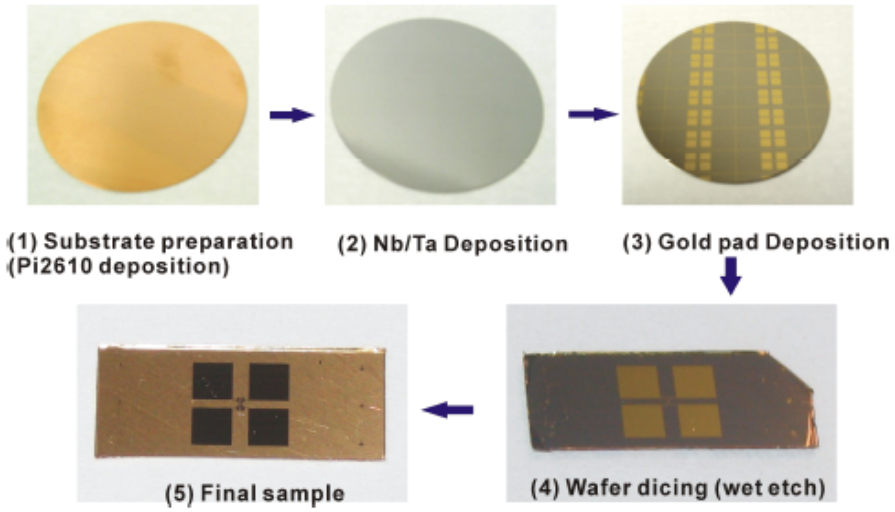

Figure 32: Outline of microfabrication procedure of mechanically controllable break junction. As the procedures outlined in figure 31 are followed the actual results will follow the illustrated sequence.

exposed in a mask aligner. The wafer then was placed for 20 minutes into a chlorobenzene bath that hardened the surface layer of the photoresist. This step allows for a cleaner liftoff.

Next, the wafer was developed in Microposit MF-315 developer for 70 seconds. 15nm of titanium was evaporated onto the sample, acting as an adhesion layer, followed by 135nm of gold to act as contact pads. The unwanted metal was lifted off by soaking the wafer in heated Microposit 1165 remover for 2 hours.

Since the smallest dimension of the bridge is approximately 200nm, the junction must be patterned using e-beam lithography. PMMA/MMA bilayer was spun over the sample at which point the junction was exposed in a modified SEM/EBL tool after which the pattern was developed in 1:3 MIBK/IPA. Aluminum was evaporated over the sample and lifted off in an acetone bath. This was done in order to protect the bridge region while the unwanted metal was removed (*i.e.*, an aluminum dry etch mask was patterned over the junction using e-beam lithography).

The filament evaporator was used to deposit 75nm of aluminum over the surface of the wafer. Lifting off in acetone was followed by dry etching *via* RIE. In order to enable a more uniform subsequent etch, the oxidized portions of the sample were etched away. Using

SF_6 precursor gas, niobium was removed, followed by removal of the aluminum etch mask by a combination of BCl_3 and Cl_2 gas. In the final step, oxygen plasma, under high RIE pressure, was used in order to isotropically dry etch the polyimide in order to free the break junction.

3.3 Circuitry

As previously mentioned, the circuitry of the experimental setup must allow measurement of the IV characteristics of our samples along with higher order derivatives of current with respect to potential. By applying a large DC bias current with an adjunct small AC signal, the resulting voltage across the junction and differential conductance of the junction can be measured.

While measurement of the voltage across the junction requires no explanation, that of the differential conductance may. In response to the small AC bias current that initially was driven across the junction, a small AC voltage develops across the junction. A lock-in amplifier is used to measure the resulting signal.

Since the AC signal is small, it should come as no surprise that a Taylor expansion about the DC bias current (I_0) is performed:

$$V(I) = V(I_0) + (\frac{dI}{dV})_{I_0}(I - I_0) + (\frac{d^2V}{dI^2})_{I_0}(I - I_0)^2 + ... \tag{86}$$

By noting that the difference between the total current (I) and the DC bias current is small, it becomes apparent that all terms of second order or higher will make inconsequential contributions to the voltage. Thus if the reference frequency of the lock-in amplifier is that of the applied AC signal, the first term of the series can be eliminated and the output of the lock-in amplifier is dV.

The sample bias resistance is much larger than that of the mechanically controllable break junction's resistance, and thus dI may be expressed as:

$$|dI| = \frac{|V_{AC}|}{R_{mcbj} + R_b} \approx \frac{|V_{AC}|}{R_b}. \tag{87}$$

By dividing our expression for dI by the output voltage obtained from the lock-in amplifier, we can determine the differential conductance.

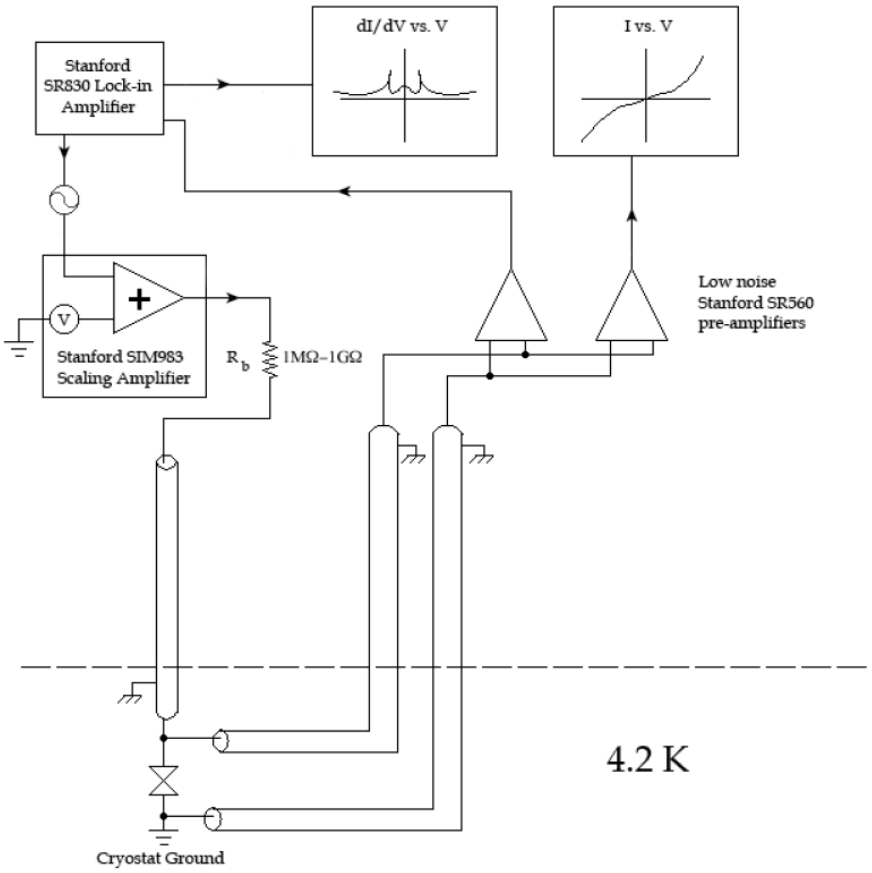

Figure 33: The measurement circuit for IV and differential conductance vs voltage measurements. The DC bias is provided by a low frequency triangular wave generated by a SRS DS 345 function generator. The Stanford Research Systems SR830 lock-in amplifier was used to generate the low amplitude AC bias that is needed for differential conductance measurements. The SRS SIM963 scaling amplifier is used in order to add both of the signals that feed to the sample through a resistor of comparatively high resistance, thus causing the sample to be effectively current biased. The two battery operated SRS SR560 preamplifiers, one in DC mode for IV measurements and one in AC mode for conductance measurements, amplify and filter the sample[52].

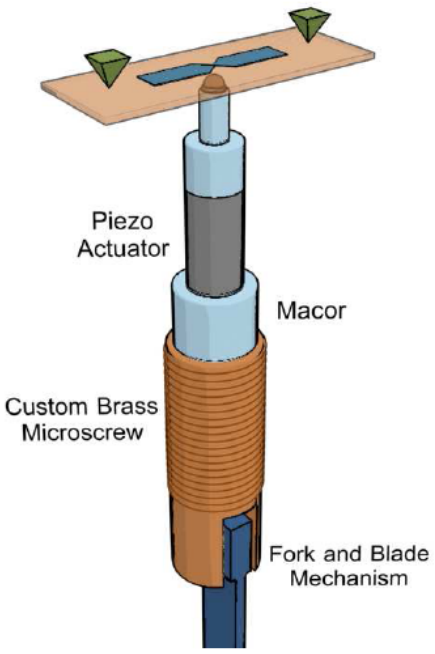

Figure 34: Schematic (three dimensional view) of the bending system. Inside of the vacuum chamber the sample can be adjusted by the 1/2"40 custom made microscrew. The screw is brass while the nut is stainless steel in order to insure that the actuator does not jam after cryogenic temperatures have been reached. The piezo tube is used in order to insure that the bending of the substrate is not only exceedingly small, but also reproducible and controllable.

3.4 Mechanical Measurements

Having described the process of retrieving information about conductance, voltage, and differential conductance, our next step is to determine how to control the physical separation between the contacts. For this process a piezo tube is used as an actuator, as illustrated in fig. 34. We note that a Macor ceramic piece is used to act as an electric insulator between the piezo actuator and other components of the bending system.

The elongation, as determined by the manufacturer, may be expressed as:

$$\Delta L = \frac{|d_{31}| \times L}{t} \times V, \tag{88}$$

where ΔL is the elongation of the piezo tube, d_{31} is the elongation constant for PZT-5A at 4.2K ($-0.031\frac{nm}{V}$), L is the tube length, and t is the wall thickness of the piezo.

Bearing in mind that the elongation of the piezo tube is not equal to the separation between the contacts, next we must calibrate our system. The separation between contacts

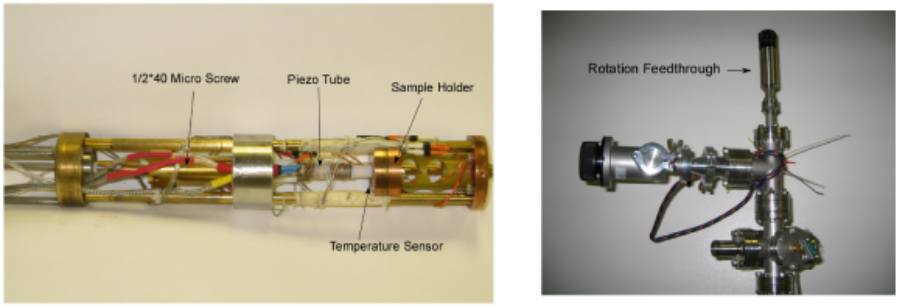

Figure 35: A picture of the bending system and the top manifold showing electrical, mechanical and vacuum feedthroughs. The left panel pictures the manifold that is attached to the top of the dipstick in order to ensure access to all the various components. The right panel pictures the bending system illustrated in figs. 34 and 27.

is less than the elongation of the piezo tube and, as a result, allows for measurement of extremely small contact separation. The reduction ratio between the elongation of the piezo tube and the contacts is given by:

$$r_d = \frac{\hbar}{2\sqrt{2m}} \frac{\alpha}{\sqrt{\phi_{eV}}}, \tag{89}$$

where r_d is the reduction ratio, ϕ_{eV} is the materials work function[88] in electron-volts. α is defined as:

$$\alpha \equiv \frac{\partial \ln(R)}{\partial v}, \tag{90}$$

where R is the resistance that is dependent on the separation between tunneling points and is thus given by:

$$R \propto \exp[\frac{2}{\hbar}\sqrt{2m\phi} \times \delta, \tag{91}$$

in which δ is related to the actuator voltage. This implies that α may be expressed as:

$$\alpha = \frac{2}{\hbar}\sqrt{2m\phi} \times r_d, \tag{92}$$

which yields, upon a linear fit, a value of $\alpha = 0.0042$. Thus our ratio may be expressed numerically as:

$$r_d = 1.96 \times 10^{-4} \frac{nm}{V}. \tag{93}$$

Although this method makes the assumption that the work function value is that of a clean and smooth surface, the model is still used for our elongation calibration. This

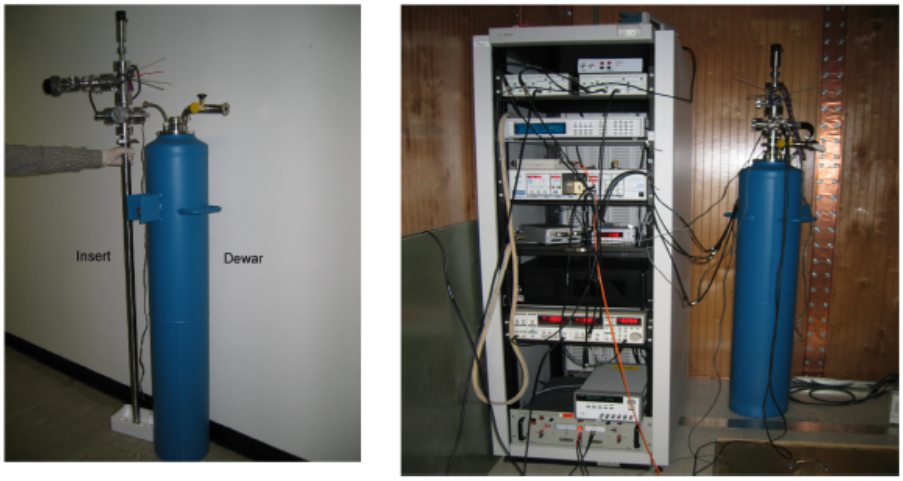

Figure 36: The custom made dipstick is used for housing the sample and is then inserted into the liquid helium dewar when the experiments are performed, as illustrated in the right panel.

assumption, most likely, leads to a value of sample elongation that is somewhat larger than the actual value. Since our primary purpose for the piezo is to determine the general characteristics of the conductance as the contacts are separated, this technique is adequate. The results allow us to determine when we have moved from the bulk contact regime to that of atomic point contact and subsequently the tunneling regime.

3.5 Cryogenic Setup

Having covered the mechanical controls for the contact separation, our procedure for determining the IV characteristics as well as differential conductance of the sample and the process of fabrication of the sample, the last requirement is to provide an environment of superconducting temperatures for our samples. In addition to the requirement of superconducting temperatures, our sample region must be under ultra-high vacuum ($\approx 10^{-7} Torr$) in order to avoid contamination of the metallic surfaces.

In order to house the sample, electronics, and bending mechanisms for the mechanically controllable break junction, a custom built dipstick refrigerator was constructed. A manifold is attached to the top of the dipstick in order to ensure access to all the various components. This allows easier access to mechanical and electrical feedthroughs that are necessary to pump down, actuate, and measure the sample.

First, the sample must be evacuated, and a base pressure achieved. Once this vacuum state has been reached, the cooling process must begin. Using a separate dewar than that in which the experiments will be conducted, the sample is cooled to liquid nitrogen temperatures.

After liquid nitrogen temperature has been reached, the dipstick is inserted into a liquid helium grade, super-insulated, nitrogen-free dewar. This allows the the dipstick to continue to cool until it reaches 4.2K, and our experiments to be conducted in an environment anywhere from 4.2K to 10K. Since the critical temperature of niobium is 9.3K and that of tantalum is above 4.2K, our experimental range is covered by this cryogenic setup.

CHAPTER IV

DOUBLE POINT CONTACT SPECTROMETER

At this point a brief review of all of the apparently disjointed material we have covered is in order. Chapter 1 introduces the reader to important concepts in superconductivity, namely quasi-particles and Cooper pairs, for the sake of their future importance in charge transport. Chapter 2 shows how the Josephson effect is altered by external fields and radiation and as a result can be used to reproduce the spectrum of incident radiation. Chapter 3 demonstrates how the experiments, needed to obtain these crucial results, namely IV and differential voltage versus current plots, are conducted. These preliminary chapters provide the foundation so that the experimental technique used in this chapter will appear crystal clear to the reader.

In Chapter 2 we noted that the Josephson effect could be used to generate radiation of frequency $\omega_J (= \frac{2eV}{\hbar})$, which is particularly useful due to the extremely small value of Plank's constant. The radiation that the junction generates falls in the GHz to lower THz range. Since sources of radiation that fall in the lower THz range are few and unreliable, the usefulness of the Josephson effect is readily apparent. This characteristic, coupled with our ability to use the change in IV characteristics to determine the spectrum of radiation incident upon a Josephson junction, hints at a usefulness in the realm of spectroscopy.

If a single molecule, placed between the tips of the atomic point contacts (see fig. 37), was irradiated, the change in IV characteristics of the junction would indicate the spectrum of radiation, between the GHz and lower THz range, absorbed by the molecule. Our ability to control the radiation source, by adjusting the voltage across the source junction, provides the perfect conditions for a new technique of molecular absorption spectroscopy.

Before covering the technique of double contact spectrometry *via* the Josephson effect, we felt it would be advantageous to cover the fundamentals of absorption spectroscopy and a few of the techniques of single molecule absorption spectroscopy. This may help, by

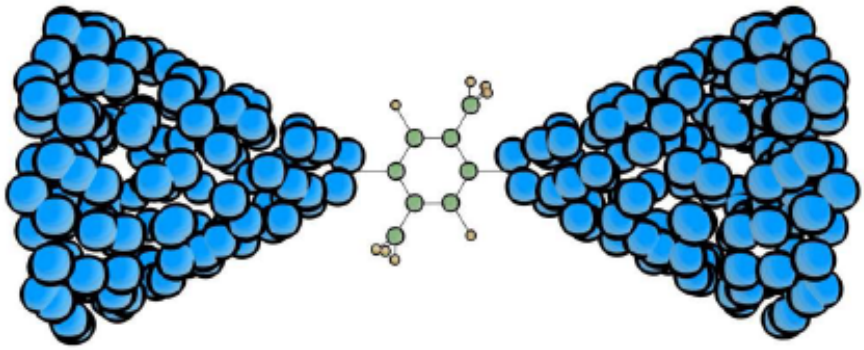

Figure 37: Point contact junction which is bridged with an organic molecule. The absorption spectrum of the molecule is determined by analyzing the change in the samples IV characteristics and then performing a Hilbert transform on the results.

providing a reference that highlights some of the advantages and drawbacks of our technique.

4.1 Absorption Spectroscopy

The technique of absorption spectroscopy is reliant on the quantization of energy levels of molecules. Due to this quantization, only certain amounts of energy can be absorbed by a given molecule. Since this energy is provided in the form of radiation, this subsequently quantizes the wavelength of radiation that the molecule can absorb, and this spectrum of radiation is unique to a given molecule. As a result of each molecules unique spectrum, we are provided with a way of determining the presence of a given chemical in a sample solution.

The internal energy of a molecule can be looked at as consisting of three parts: electronic, vibrational, and rotational. Consequently the total energy may be expressed as[115]:

$$E_{int} = E_{el} + E_{vib} + E_{rot} \tag{94}$$

Absorption of radiation of sufficient wavelength will result in a change in the electronic state accompanied by a small change in both vibrational and rotational energies. The presence of rotational and vibrational energies leads to a broadening of the line that would result if only electronic transitions were allowed. Moreover the appearance of absorption *bands* will be observed during absorption spectroscopy. A graph of absorption versus wavelength

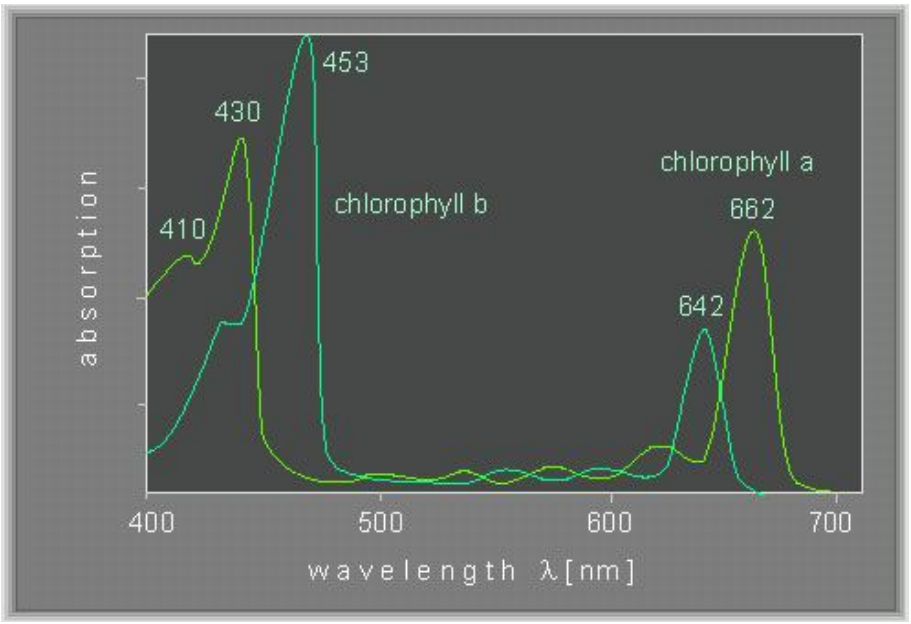

Figure 38: Absorption spectra of chlorophyll a and chlorophyll b. Note the broad width of the peaks due to vibrational and rotational motion. If only electronic transitions were allowed the peaks would have no width and would resemble delta functions at 410nm, 430nm, 453nm, 642nm, and 662nm.

would consist of Gaussian functions as opposed to delta functions as illustrated in fig. 38.

What must be kept in mind is that the graph of absorption versus wavelength is representative of not only the molecule present, but also the solvent, concentration, and temperature. Thus for absorption spectroscopy, resultant characteristics of the molecule under observation are mixed with those characteristics of the environment. The presence of a given molecule in solution can still be detected, and in this capacity absorption spectroscopy finds much of its use.

Absorption spectra are normally measured with devices consisting of three major parts. First a radiation source is needed. Next we need an optical system consisting of a spectral apparatus, a sample compartment, and a radiation detector. Finally a system for data acquisition and processing is needed. Various techniques of absorption spectroscopy have been illustrated in fig. 39, but the fundamentals of the technique are the same for each.

Continuum sources of radiation are normally employed for absorption spectroscopy, such as tungsten-halogen, deuterium, and xenon arc-lamps. As far as the sample compartment is concerned, shape, absorption path length, window thickness, volume, and cross section

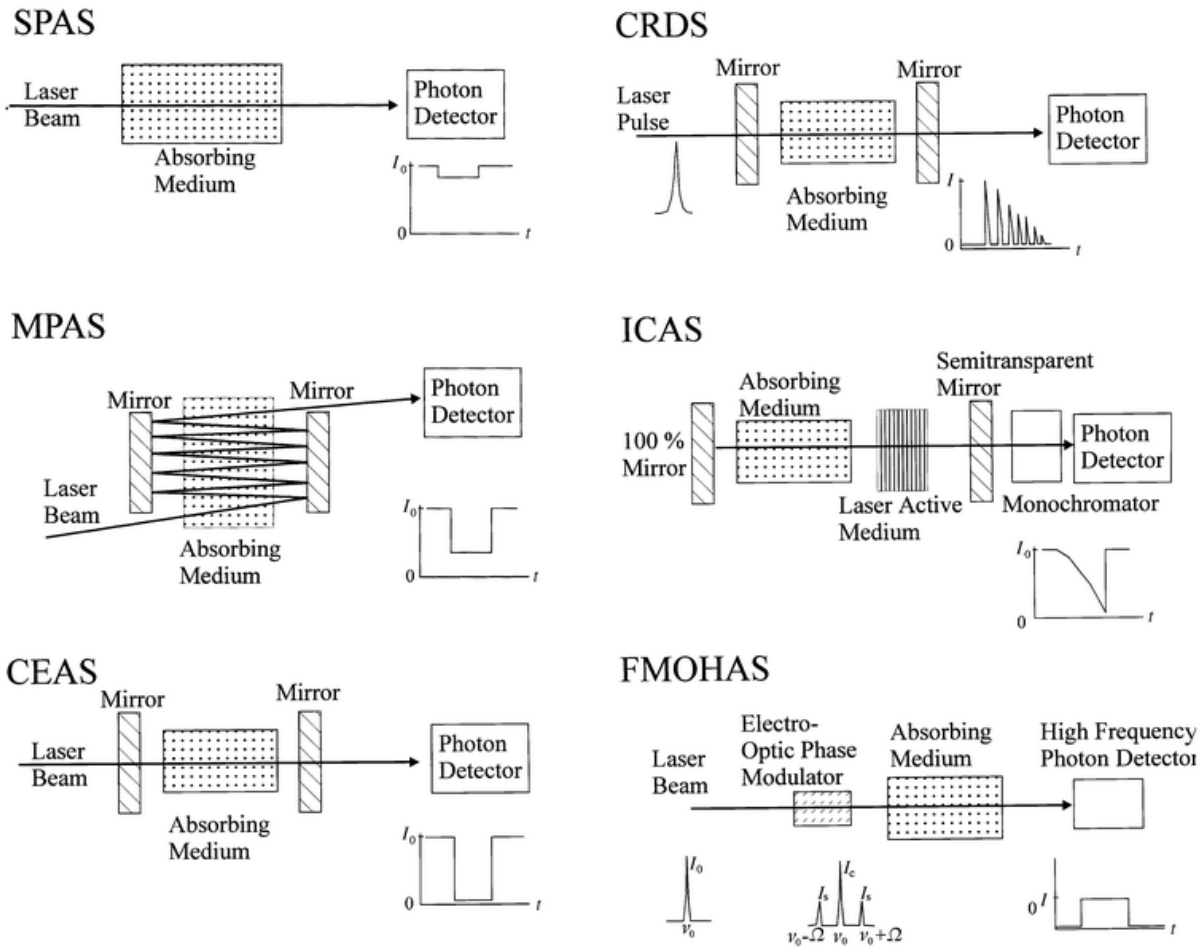

Figure 39: Illustrated are various techniques of absorption spectroscopy. Although the details of each technique vary slightly, as can be seen from the general outline of the figures, each follows the general procedure indicated in the text. Therefore a detailed treatise on each technique is avoided.

are important factors. Normally one cell contains the solvent *sans* the sample is used as a reference in which to compare the cell with the sample. The simplest processing consists of the transmittance or absorbance in an analog or digital form.

The measuring techniques used in absorption spectroscopy fall into two primary categories: qualitative and quantitative. Qualitative analysis involves identifying the presence of a given molecule in a sample. Identification is accomplished by comparing the absorption spectra with graphs or tables of solvents with similar concentrations and temperatures.

For quantitative measurement the Beer-Lambert law must be employed:

$$A = -\log_{10}(\frac{\Phi_t}{\Phi_0}) = \varepsilon cb, \tag{95}$$

where A is the absorbance, Φ_t is the monochromatic radiant power transmitted by the absorbing medium, Φ_0 is the monochromatic radiant power incident on the medium, ε is the molar absorption coefficient, c is the amount concentration, and b is the absorption path length. Using the Beer-Lambert law, the concentration of a known analyte is determined by measuring the absorbance at various wavelengths. If the Beer-Lambert Law holds, then a graph of absorbance versus concentration will result in a straight line which passes through the origin as illustrated in fig. 40. For high concentrations, the graph becomes nonlinear. This region is not illustrated in fig. 40.

If n absorbing analytes are present in the solution, then using the Beer-Lambert law and measuring the absorbance at various (k) wavelengths, the absorbance may be determined. For a given wavelength λ_a the total absorbance is:

$$A(\lambda_a) = b\sum_{i=1}^{n} \varepsilon_i(\lambda_a)c_i. \tag{96}$$

Use of the Beer-Lambert law will result in k simultaneous linear equations from which the n concentrations can be determined. The effects of impurities in the sample are minimized by measuring the absorbance at different wavelengths. Minimization may be achieved by repetitively switching from one wavelength to another.

In cases in which the Beer-Lambert law does not hold true a method called absorbance matching often is employed. Then, a sample will be diluted with a solvent until the absorbance matches the absorbance of a known concentration of the analyte in a reference

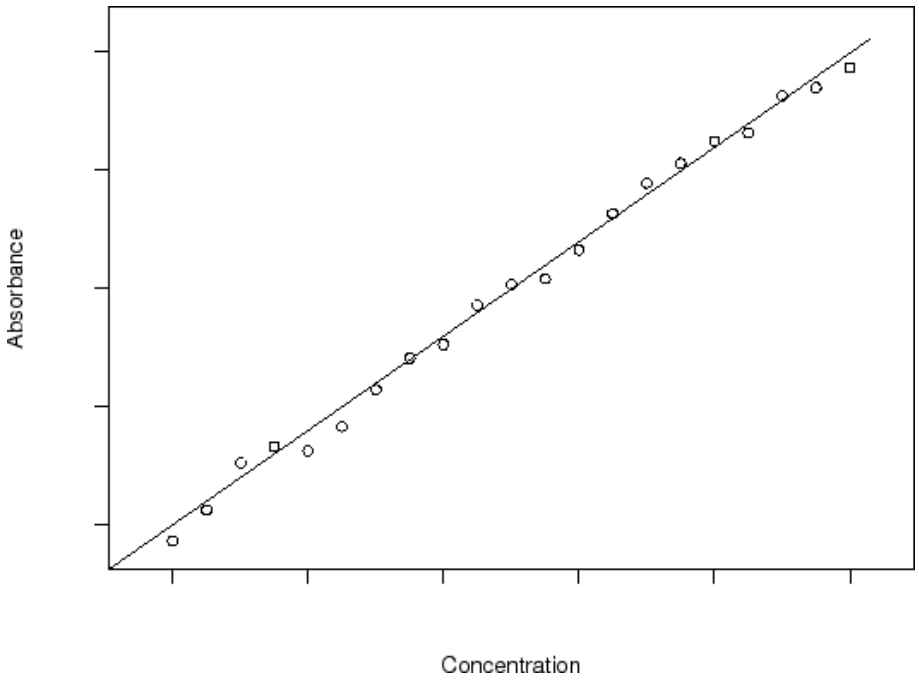

Figure 40: The curve of the absorption versus concentration must be a straight line if the the Beer-Lambert law holds. For high concentrations the graph becomes nonlinear, thus if the axes were extended, the slope of the line would begin to increase and resemble the IV curve of a light bulb.

cell.

In our description of absorption spectroscopy, we were able to use the technique for determination of the presence and concentration of a given molecule, yet little information, aside from the internal energy resulting in the given molecules spectra, about dynamic properties of the material was gained. In order to gain more insight into the dynamic (vibrational and rotational) properties of the molecule, we must veer from our practice of analyzing the behavior of bulk materials and focus on single molecules.

4.2 Single Molecule Absorption Spectroscopy

Our previous description of absorption spectroscopy dealt with the absorption spectra of samples consisting of many of the investigated molecules, as illustrated in fig. 39. The resultant spectrum is due to an ensemble averaging of the characteristics of the observed molecules. Recall that the ensemble averaging technique implicit in quantum mechanics hides the effects that the phase of a particle has in normal metals. The only time the effects

of the phase could present themselves was when dealing with superconductors in which the phase was shared by the entire metal. In a similar vein, the effects of ensemble averaging of the absorption of a given molecule may hide some of the characteristics that would be present were we able to isolate a single molecule and investigate its absorption spectra.

An example will illustrate this point. Green fluorescent protein when observed in an ensemble appears to continuously radiate green light. When a single molecule of green fluorescent protein is isolated and observed, the molecule exhibits a tendency not towards a continuous fluorescence of green light, but rather a blinking of emitted radiation. This effect is covered up when looking at an ensemble of green fluorescent protein, for only if all of the proteins happened to be in phase would there exist a time in which no radiation was emitted from the entire sample.

[As a side note, it may be apparent that many of the examples used in this chapter have a strong biological character (*i.e.*, chlorophyll b, green fluorescent protein etc.). The reason for this abrupt shift in focus is that ultimately our experiments will be conducted on biological molecules and therefore comparable techniques in chemistry and biology were investigated painstakingly.]

Another advantage associated with investigating single molecules, as opposed to an ensemble, presents itself when dealing with sequential dynamics. When looking at a population of molecules undergoing a series of events, these molecules tend to become out of phase. Due to the large number of particles present in the sample, details of the dynamic process's (*eg.*, linear polymerization) individual steps are lost. By investigating a single molecule, such phase discrepancies are removed. The final advantage of investigating a single molecule, as opposed to an ensemble, is our ability to measure mechanical and electrical properties of that single molecule. These measurements can include binding forces, torque, bond strength, and conductivity.

The *modus operandi* for single molecule spectroscopy is to match the fluorescence amplitude with some physical parameter such as movement, binding, or state changes. The energy associated with such physical changes generally can be modeled, and, as a result, experimental data may be used in order to determine the true value of given parameters.

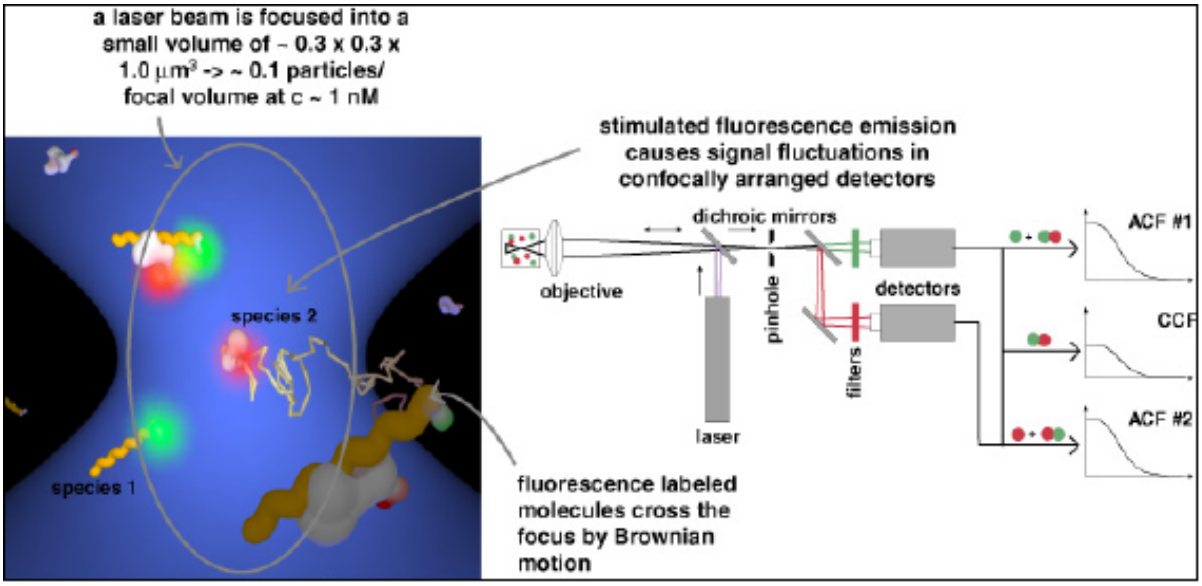

Figure 41: Illustrated diagram of a confocal microscope. The laser beam is passed through an aperture and reflected from a dichromatic mirror at which point the reflected light is directed towards the sample. The sample absorbs the light and emits radiation in all directions, a fraction of which is collected by the objective lens. *Note the small cross sectional area of the beam allows very few molecules to be excited. Ideally the area will be small enough to allow one molecule to be excited.

Before examining various methods of single molecule spectroscopy, we must mention that this technique also finds applicability in the realm of extremely sensitive imaging. Our first technique, confocal microscopy, finds some of its usefulness in this realm.

4.2.1 Confocal Microscopy

A description of some of the techniques of single molecule absorption spectroscopy may serve to illustrate the utility of the Josephson effect as an alternative approach. The technique of single molecule spectroscopy with a confocal microscope uses the three dimensional image obtained from a confocal microscope in order to determine the radiation spectrum of a single molecule[194].

In confocal microscopy, the laser beam is passed through an aperture and reflected from a dichromatic mirror. The reason to use this mirror is its ability to reflect light of a single wavelength while allowing all other light to pass through. The reflected light is directed towards the sample. Because of the small size of the initial aperture and the monochromatic

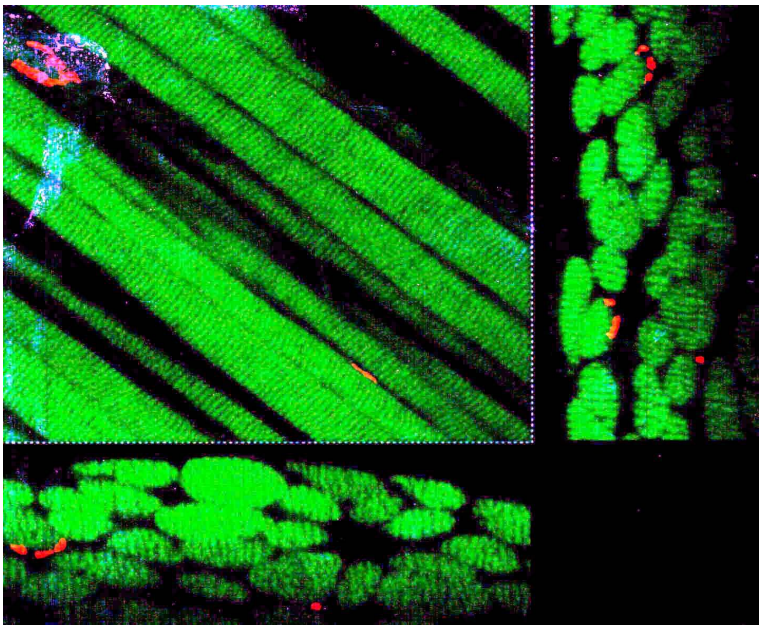

Figure 42: Illustrated in a confocal microscope image of a glycerol embedded specimen.

nature of the light incident upon the sample, we know that only a single molecule absorbs the light and that the absorbed light was monochromatic, as illustrated in fig. 41.

After the sample absorbs the light, the sample will emit radiation in all directions. A fraction of the emitted photons will be collected by the microscope objective and imaged onto the detector. A pinhole is placed in front of the detector in order to block all out-of-focus light. The resolution of this technique is due to the blocking of light coming from all out-of-focus planes.

After one run a single section of the sample will have been imaged. To obtain an entire three dimensional image of the sample either the sample must be rotated or the laser must be rotated and the above imaging process repeated. Due to the flexible nature of biological molecules, the latter technique usually is adopted, in order to minimize blurring. Thus the laser normally is used to scan the sample in order to generate a high resolution three dimensional image of the sample.

The most important part of the confocal microscope is the objective, which is used for illumination of the sample and light collection. Thereofore the most critical restriction of this technique is based on the abberations caused by the lens. The various kinds of

corrections (achromatic, apochromatic, fluorite, planachromat, and planapochromat) allow this technique to be useful in various parts of the spectrum when a particular correction is adopted.

The next limitation arises from the scanning process of the sample. As previously mentioned, due to the ability to image only a small section of the sample per run coupled with the flexibility of the sample, the laser must be rotated. Even with this technique we suffer from the natural limitations of serial data collection. These limitations consist of compromising between the rate of image acquisition, spatial resolution of the raster scan, and the signal-to-noise ratio.

For the detection process there are also limitations which are limited by the use of either a photo multiplier tube, avalanche photo diode or a charge coupled device. These techniques operate within the same range but vary in their quantum yield and signal-to-noise ratio.

4.2.2 Laser Absorption Scanning Tunneling Microscopy

Because of the lack of infinite absorption capability of a single molecule, the technique of confocal microscopy is plagued with the problem of an often inadequate signal-to-noise ratio. By combining the atomic resolution of scanning tunneling microscopy with the chemical selectivity of optical spectroscopy, headway can be made into overcoming this limitation.

While laser assisted scanning tunneling microscopy overcomes the limitations inherent in fluorescence and near field scanning microscopy, namely the lack of applicability in the strongly quenching surface environment and limited spatial resolution, respectively, laser heating has been a recurring problem. This problem arises because, "As long as the system absorbs light and heats up, atomic registration is easily lost when comparing laser-driven signals to nonilluminated signals."[17]

Laser absorption scanning tunneling microscopy combines several techniques of reducing noise that, while insufficient by themselves, when used in conjunction produce a tolerable signal-to-noise ratio. While a diode laser is used for photoexcitation of the tip sample junction, the sample is positioned to allow total internal reflection as one means of overcoming the problems inherent in tip-sample heating (illustrated in fig. 43).

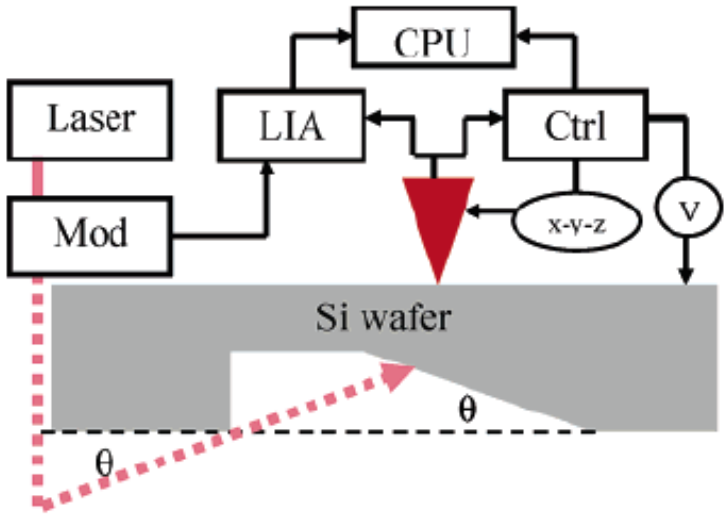

Figure 43: The experimental setup of laser absorption STM experiment is illustrated. The diode laser is modulated by an optical chopper (MOD) and illuminates the junction from the rear of the silicon. The optically modulated current is monitored by the lock-in amplifier (LIA) while the control electronics (Ctrl) apply the bias voltage to the sample using feedback current to adjust the tip height so as to maintain constant current[17].

For laser absorption scanning tunneling microscopy the sample molecule is placed on a transparent silicon substrate. The transparency condition is required since the controlled radiation sources act on the sample from below the substrate in order to reduce tip heating. As another means of reducing heating, the laser light is modulated with a mechanical chopper.

Next a lock-in amplifier is used to filter out mechanical and electronic noise. The lock-in amplifier switches on and off at the same rate as the laser and as a result the absorbed energy causes a change of shape in the electron density of the sample molecule. The scanning tunneling microscope then measures the subsequent change in shape due to its spacial dependence on the overlap of atomic wave functions on the tip and substrate/surface [17].

The modulation frequency must be chosen so as to avoid driving the system at any of the intrinsic acoustic modes. These can be determined for a given tip with the aid of a spectrum analyzer. Similar to the technique of confocal microscopy the image is constructed by scanning the sample. Raster scanning in constant current mode is run simultaneously

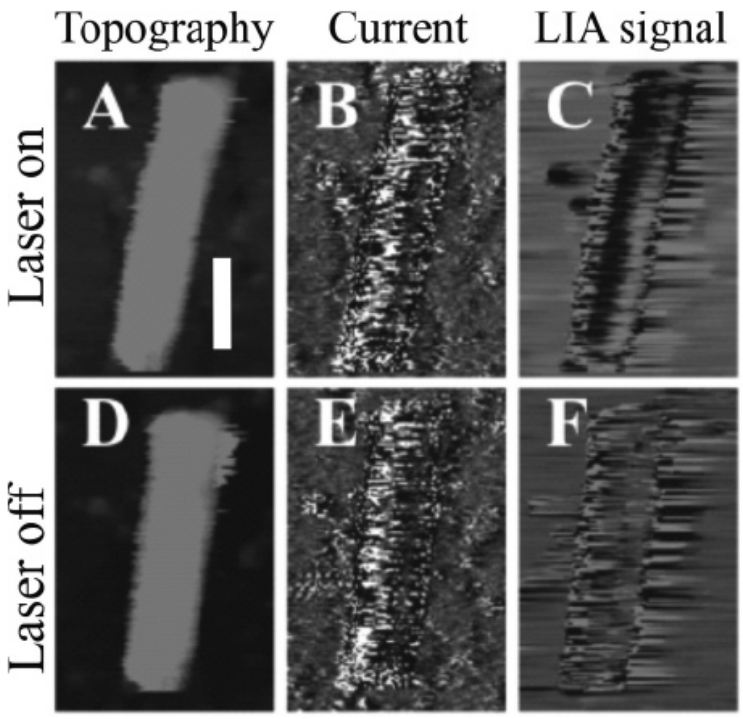

Figure 44: Carbon nanotube images. Figures A-C were acquired with the laser modulation on, while figures D-F were acquired with the laser modulation off. Figures A and D are topographic images, B and E are feedback current images, and C and F are lock-in amplifier images. Note the lock-in amplifier signal's images shows an optical signal along the backbone of the carbon nanotube[17].

while saving topography, lock-in amplification, and feedback current.

The images resulting from laser absorption scanning tunneling microscopy of a carbon nanotube are illustrated in fig. 44. We first note the difference between the topographic image and the lock-in amplifier signal when the illuminating laser is on. The latter of the two shows an optical signal along the backbone of the carbon nanotube, which is neither present in the topographic image nor in the lock-in amplifier signal with the illuminating laser off.

One source of the laser on lock-in amplifier signal is driven mechanical vibrations at the junction. This is caused by the temperature dependent expansion of the substrate. When the laser is turned off and the mechanical vibrations are simulated by electronic tip height modulation, the resulting signal has much less contrast than that resulting from the laser on signal. This discrepancy of contrast implies there is another mechanism at work than

just driven mechanical vibrations at the junction.

The difference in signals is attributed to electronic changes in the carbon nanotube from absorption. We note that as long as the excitation frequency of the laser exceeds the carbon nanotube band gap, optical absorbance will be nonzero. This absorption may result in either an increase or decrease in photoconductivity depending on the alignment of the carbon nanotube and the substrate's energy bands. In either case, increasing or decreasing photoconductivity, the optical absorbance of the carbon nanotube directly modulates the scanning tunneling microscopes current and thus provides the lock-in amplifier signal.

The prominent horizontal black/white stripes on the vertical sides of the carbon nanotube are due to noise. This noise occurs whether the illuminating laser is on or off and can be seen in fig. 45. The mean deviation from zero is large at the center of the carbon nanotube when the laser is on, and is close to zero when the laser is off. The standard deviation is maximized whether the laser is on or off.

The carbon nanotube was scanned from left-to-right. This fact, coupled to the fact that the deviation is higher along the left edge of the tube, hints at a source of the noise. As may be anticipated, the standard deviation is always greater on the leading edge of a scan. Also, the deviation from setpoint current always is greater along the leading edge due to the nonlinearity of the current with respect to the tip-sample distance, and as a result leads to the conclusion that the noise along the edges is due to transient feedback current peaks.

4.3 Double Point Contact Spectrometer

In the first section of this chapter we mentioned that the energy of a given molecule may be expressed as:

$$E_{int} = E_{el} + E_{vib} + E_{rot}. \tag{97}$$

In investigating the absorption of a single molecule, as opposed to a pure substance, using the Josephson effect, the consequences of vibration of the molecule are much more pronounced.

We first note that the appearance of current in the subgap region of the IV plot was attributed to Andreev reflection. If, as opposed to looking at the IV characteristics of the sample, we investigate the differential conductance ($\frac{dI}{dV}$) vs. potential characteristics

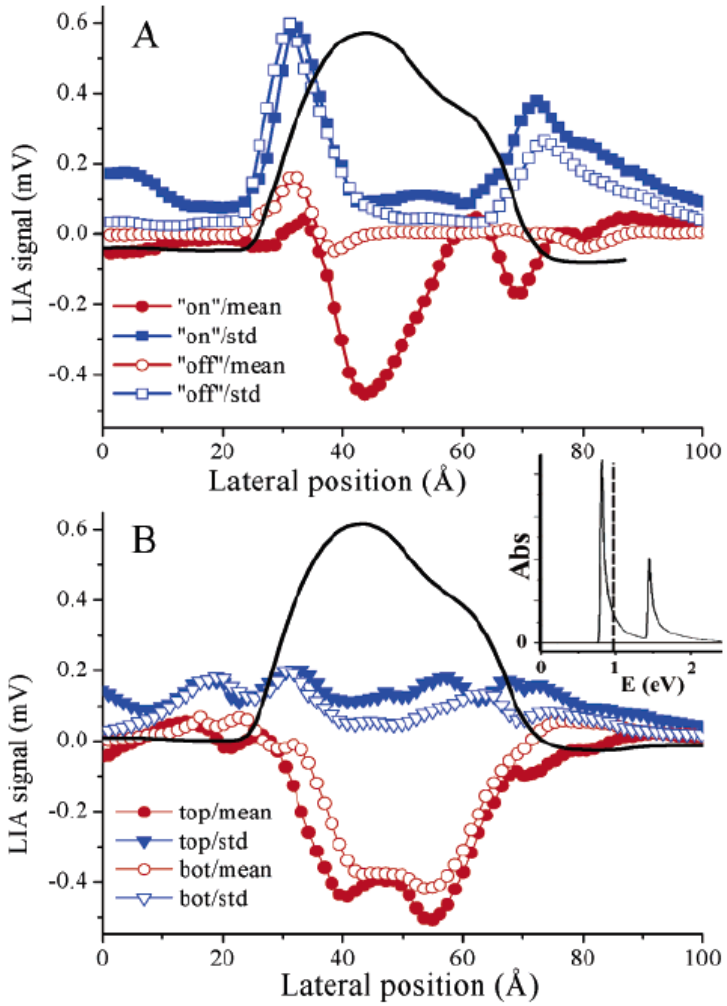

Figure 45: Illustrated are the lock-in amplifier buffer statistics. (A) The squares are standard deviation (noise) of the cross section statistics, and the circles are the background-subtracted mean signal. (B) The triangles are the standard deviation of the signal, and the circles are the background subtracted mean. The standard deviation is higher along the left edge of the tube that is due to the leading edge of the scan. From these results we find that the noise is a result of the transient feedback current peaks[17].

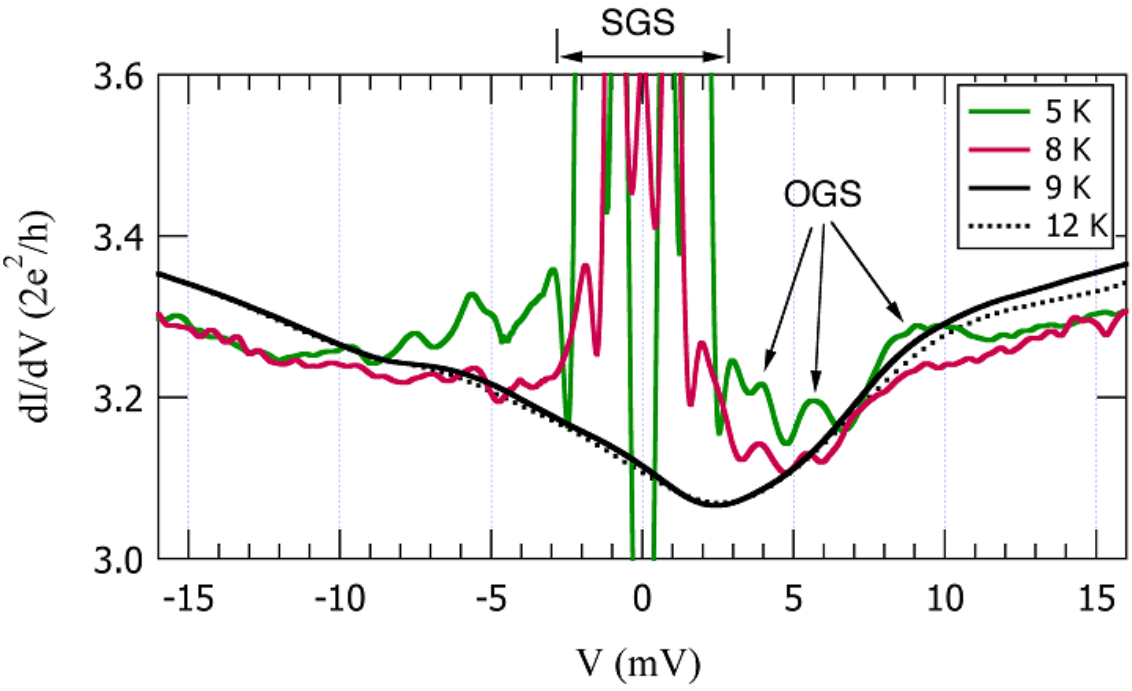

Figure 46: Illustrated are three differential conductance traces for the same contact at different temperatures. Above the critical temperature, the peaks disappear indicating that the existence of the over the gap structure and the subgap structure are superconducting phenomena. While the subgap structure is a consequence of Andreev reflection, the over the gap structure is a consequence of the resonant interaction between the Josephson current and the vibrational modes of the material between the tips of the junction[24].

of the sample, we will observe a few distinct features when the sample is below its critical temperature (T_c), as illustrated in fig. 46.

At temperatures above the critical temperature, there is a smooth somewhat symmetric decline upon approaching a voltage of zero from either direction of polarity. At temperatures below the critical temperature, the graph is not as well behaved. The large peaks centered about the zero voltage mark are a consequence of Andreev reflection and may be interpreted as the subgap structure (SGS) that results in the differential conductance versus potential curves.

The peaks that occur in the subgap structure occur at voltages equal to $\frac{2\Delta}{ne}$. Due to the temperature dependence of the energy gap (Δ), the positioning of each of these peaks would be expected to change upon altering the temperature of the sample. As previously mentioned, when the temperature of the sample is increased, the gap energy of the junction

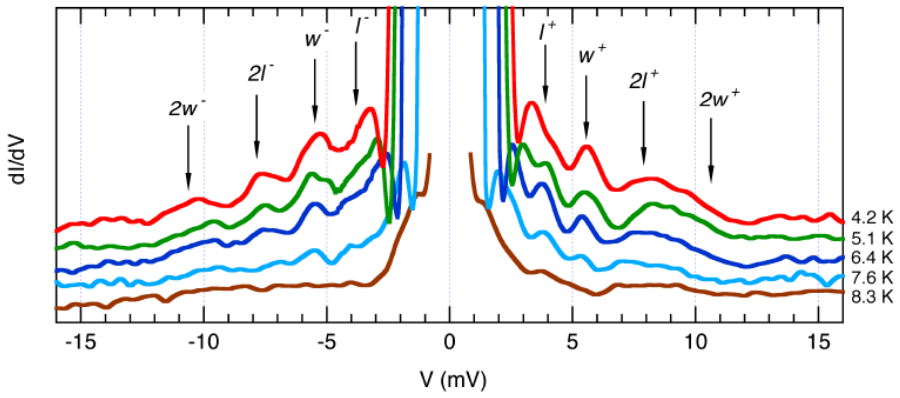

Figure 47: Illustrated are differential conductance traces for the same contact at different temperatures below the critical temperature. Note the spread of the sub-gap structure as the temperature decreases, where as the over-the-gap structure maintains its same position while increasing in magnitude. The letters l and w stand for longitudinal and wagging modes, referring to the motion of the molecule between the tips responsible for the given peak.

decreases and a narrowing of the subgap structure should result; as if the curve would approach a delta function when the critical temperature were reached.

The two less pronounced spikes on either side of the SGS are referred to as the the *over-the-gap structure*. By increasing the temperature of the sample until the critical temperature is reached, it will be noted that the position of the constituent peaks that make up the over-the-gap structure remain unaltered, as illustrated in figure 47. There magnitudes decrease until the the critical temperature is reached and the smooth symmetric curve is recovered, but their positions are not altered by changing temperature.

Alternatively, as the temperature of the sample is decreased, the subgap structure appears to become broader. As this temperature decreases, the spread of the subgap structure extends into the region of the over-the-gap structure. Since this broadening of the subgap structure is accompanied by an increase in the magnitude of the peaks of the over-the-gap structure, the effects of the latter are still apparent.

For a physical interpretation of the over-the-gap peaks we must recall that, in terms of tip separation, a junction may fall into three categories. When the tips are close enough together for the phases of each of the superconductors to lock-up, the junction acts as a single superconductor and tunneling occurs. When the separation between the tips is large,

the phases of the superconductors not only cease to lock-up, but also they cease to interact entirely with one another. This region is the bulk point contact regime as opposed to the previously described tunneling regime.

Our experiments are conducted in the small window that exists between these two regimes. For tip separation that falls in this window, the phases of the superconductors do not lock-up but they do interact with one another. The difference between the phases of the adjacent superconductors causes Josephson current. It is in this regime where the over-the-gap structure occurs at definite voltages.

Experiments on the system when the separation between the point contacts is large enough to fall into the bulk point contact regime (*i.e.*, $G \geq 5G_0$) find that, as opposed to peaks, there are stepwise drops in the differential conductance curve. These steps are attributed to the phonon modes of the materials lattice. As mentioned in Chapter one, phonon modes are associated with vibrational motion of a given atom or molecule. (Note, from our section on the Fiske effect[74], that the steps that occurred in the IV curve of a junction in which a field was applied were attributed to the interaction between the Josephson current density waves and the electromagnetic fields in the junction that acted as a resonator.)

Consequently, the appearance of a peak at these same voltages when we are between the bulk point contact and tunneling regime implies some mechanism of interaction with the vibrational mode of our molecule. As this voltage corresponds to a definite Josephson current oscillation, the appearance of peaks in the over-the-gap structure is attributed to resonance between the vibrational eigenmodes of the molecule between the contacts and the Josephson current oscillations[124].

As a rudimentary example the situation can be likened to a father pushing a child on a swing. The father plays the part of the driving Josephson current and the child that of the vibrating molecule in between the contacts. If the father pushes the child in the swing at the exact time the child moves passed him, in the proper direction, the child will swing higher and higher with each pass (*i.e.*, resonance). If, on the other hand, the father pushes the child at different parts of the motion, then the effect will be at times to make the child

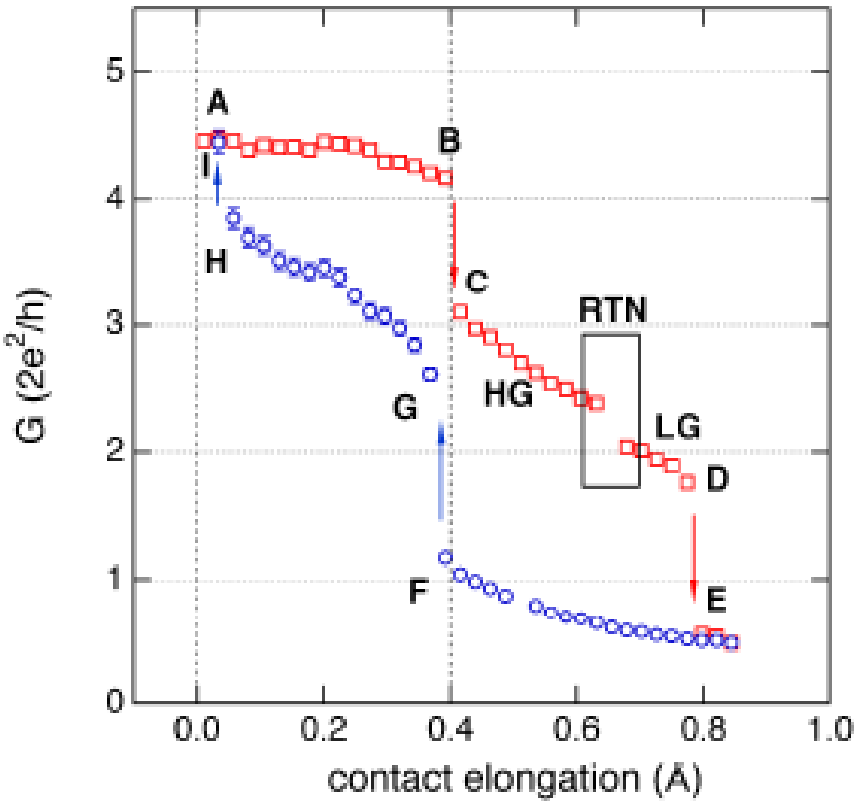

Figure 48: Illustrated is conductance versus contact elongation at 4.2K. We note the three regions corresponding to bulk contact, point contact, and tunneling regimes. The high conductance (HG) region corresponds to a shorter tip separation and a symmetric orientation of the molecule between the tips. The low conductance (LG) region corresponds to a greater tip separation and an asymmetric orientation of the molecule between the tips. The random telegraph noise (RTN) region is the separation distance in which switching between the two orientations is observed. Data points from A to D were taken during contact elongation, whereas those from E to H where taken during contact contraction.

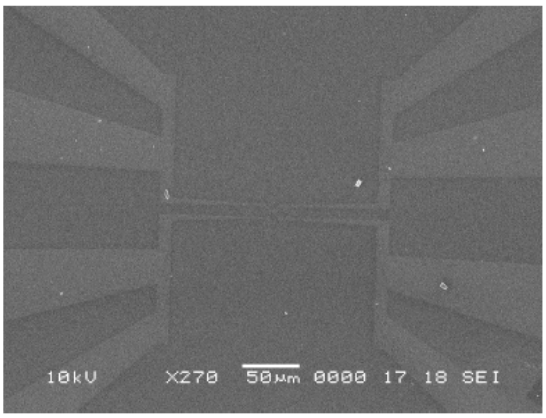

(a)

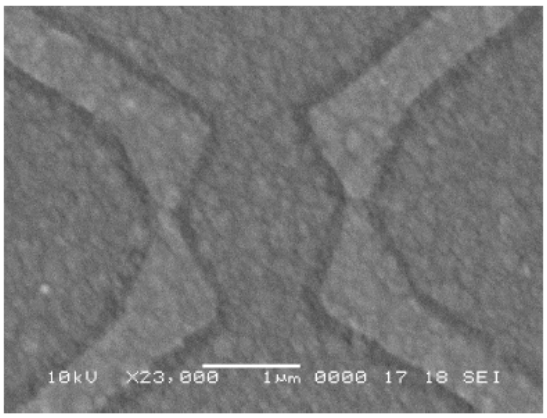

(b)

Figure 49: STM image of double point contact spectrometer. (a) Shows a zoomed out image of the device which includes the contact pads. (b) Shows a zoomed in image of the point contacts. The left point contact, consisting of niobium, acts as the radiation source, while the right atomic point contact, which contains the embedded molecule, absorbs a fraction of the radiation that thus alters its IV characteristics. Analysis of this change allows a determination of the absorption spectrum of the embedded molecule.

swing higher and at times to swing lower. (For a detailed description of the motion of the niobium dimer between the two contacts see Appendix D)

Similar to the technique of single molecule absorption spectroscopy *via* confocal microscopy in which the spectrum obtained was matched with physical parameters such as movement, binding, or state changes, the frequencies of the corresponding peaks in the over-the-gap structure are matched with physical parameters. This is done by modeling the system using first principles density functional theory. The frequencies, which fall in the terahertz region, correspond to the vibrational modes of the molecule between the contacts. Thus the spikes, which are not a result of Andreev reflection, result from a resonance between the Josephson current oscillations of the junction and the vibrational eigenmodes of the molecule. The disappearance of the peaks once the critical temperature is reached lends itself to the aforementioned explanation of the over-the-gap structure.

For the double point contact spectrometer, the response of the sample to a known spectrum of radiation is determined. As illustrated in fig. 49, one junction acts as a source of Josephson radiation at a frequency described by the Josephson relation, namely $\omega_J (= \frac{2eV}{\hbar})$. This radiation falls in the terahertz range and may cause vibration of the sample. In order

to determine which radiation was absorbed by the sample, a Hilbert transform is applied to the IV curve of the sample. By investigating the differential conductance vs. potential curve of the sample, the vibrational eigenmodes of the sample can be determined by investigating the over-the-gap structure.

4.4 Fabrication of Double Point Contact Spectrometer

The fabrication of the double point contact is similar to that of the mechanically controllable break junction with the exception that as opposed to a bronze wafer, silicon is used. The use of silicon is due to our not needing to investigate the conductance of the junction as a function of tip-to-tip separation.

1μm of SiO_2 was grown by plasma enhanced chemical vapor deposition onto the polished silicon substrate at a temperature of 250 degrees Celsius, a temperature of 900 mTorr, a power of 25W, a flow rate of 400sccm, and a N_2O flow rate of 900sccm. Following the laying of the oxide layer, a 100nm layer of niobium is magnetron sputtered onto the sample using an *in situ* cold trap to reduce the amount of contaminants, including water, in the vacuum chamber. Evaporation was avoided due to the high melting point of niobium as well as sputtering's ability to limit the amount of radiation incident on the oxide layer.

After sputtering, Shipley 1813 photoresist was spun onto the sample, baked, and then exposed in a mask aligner. The wafer was then placed for 15 minutes into a chlorobenzene bath that hardened the surface layer of the photoresist. This hardening allows for a cleaner liftoff.

The wafer was subsequently developed in Microposit 354 developer for 70 seconds. 15nm of titanium was evaporated onto the sample, acting as an adhesion layer, followed by 135nm of gold to act as contact pads. The unwanted metal was lifted off by soaking the wafer in heated Microposit 1165 remover for an hour.

Since the smallest dimension of the bridge is approximately 200nm, the junction must be patterned using e-beam lithography. PMMA/MMA bilayer was spun over the sample at which point the junction was exposed in a modified SEM/EBL tool after which the pattern was developed in 1:3 MIBK/IPA for 60 seconds and IPA for 20 seconds. Aluminum was

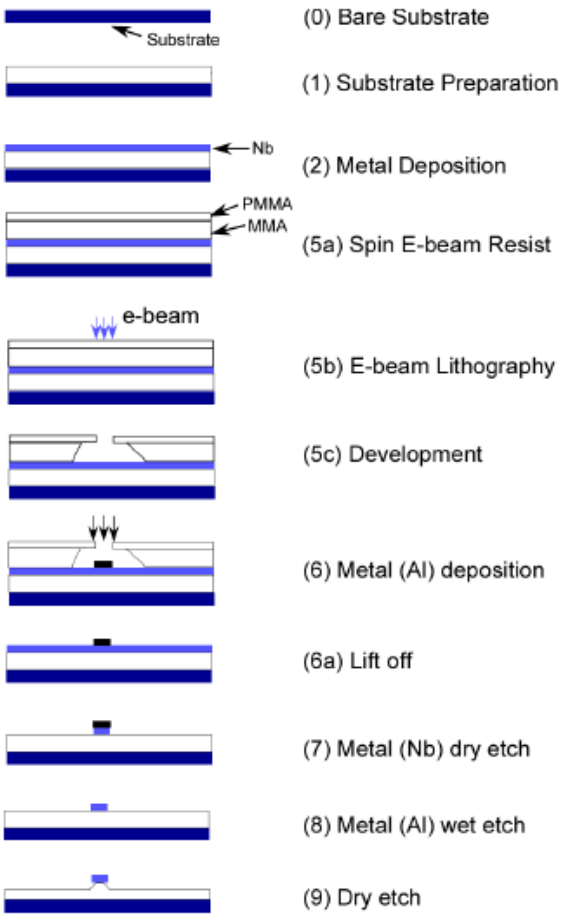

Figure 50: Step by step procedure of the fabrication process (side-view). (0) Start with silicon substrate (1) SiO_2 is grown on the silicon substrate. (2) Niobium is magnetron sputtered onto the sample. (5a) Shipley 1813 photoresist is spun onto sample; (5b) e-beam lithography is used for patterning; and (5c) Microposit 354 developer is used. (6) Filament evaporator is used to deposit aluminum over the surface of the wafer followed by: (6a) acetone liftoff, (7) dry etching of niobium, (8) etching to remove aluminum, and (9) oxidized portions.

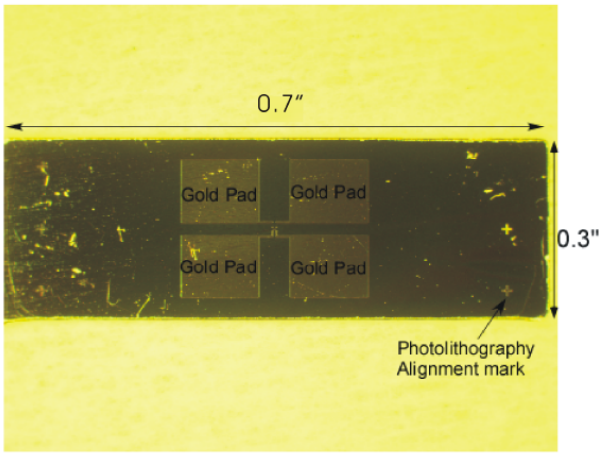

Figure 51: As the procedures outlined in fig. 50 and fig. 52 for the double point contact spectrometer are completed, the pictured sample will result.

evaporated over the sample and lifted off in an acetone bath. This was done in order to protect the bridge region while the unwanted metal was removed (*i.e.*, an aluminum dry etch mask was patterned over the junction using e-beam lithography).

The filament evaporator was used to deposit 75nm of aluminum over the surface of the wafer. Lifting off in acetone for 30 minutes was followed by dry etching *via* RIE. In order to enable a more uniform subsequent etch, the oxidized portions of the sample were etched away. Using SF_6 precursor gas, niobium was removed, followed by removal of the aluminum etch mask by a combination of BCl_3 and Cl_2 gas.

4.5 Future Work

Due to the Josephson junction's ability to act as a controllable source of electromagnetic radiation that falls within the THz gap, the door is open for future research in a regime as yet untouched. The vast majority of technology and scientific instrumentation falls below the THz gap while photonics is the dominant technology above the THz gap. Since many properties of molecules may be investigated only by probing with frequencies that fall within the THz gap region, not only will future research provide immediate application in the field of nanotechnology, but also research will increase our fundamental understanding of unexplained physical properties.

One fundamental application in the realm of biology that immediately lends itself to

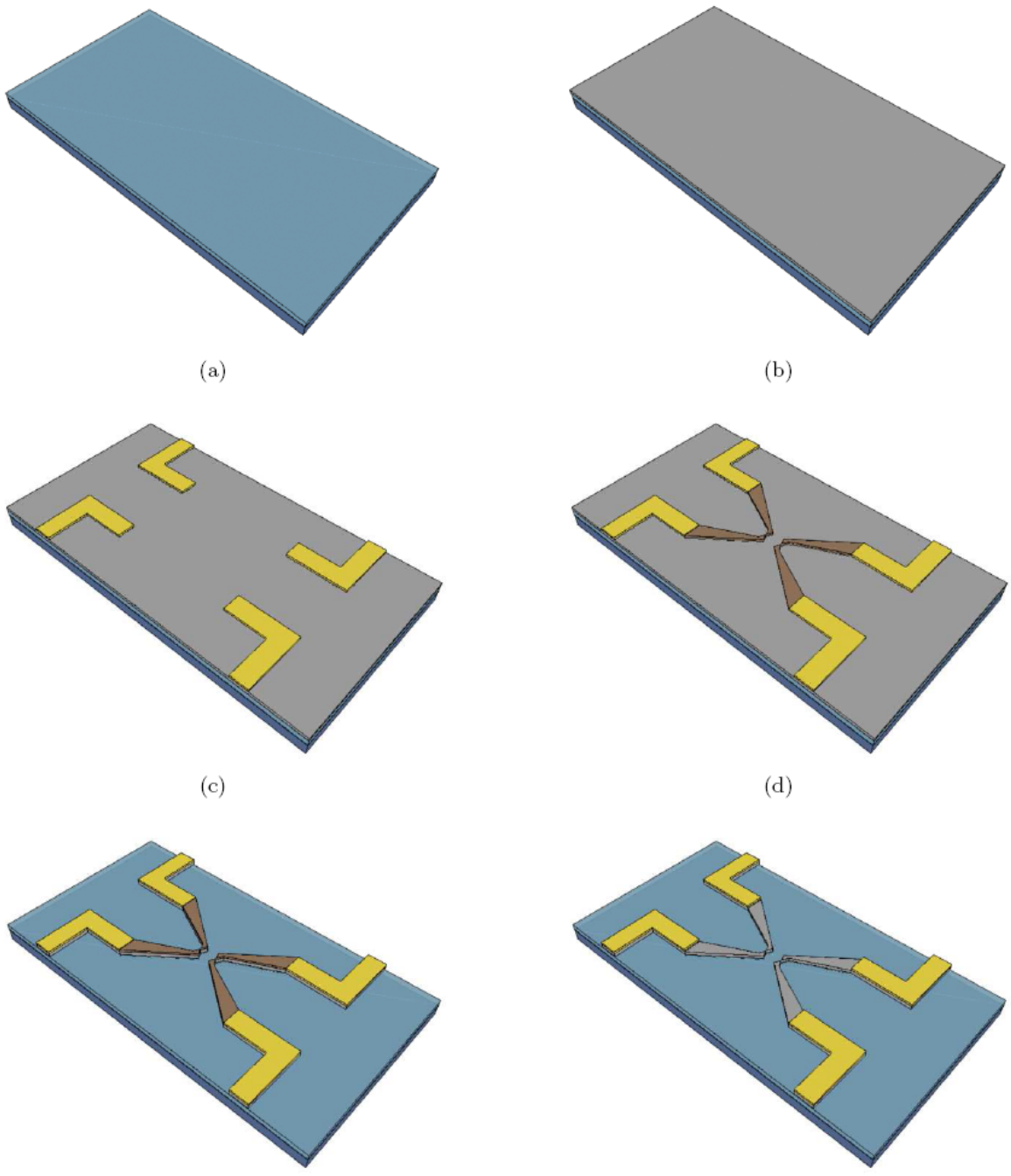

Figure 52: Two junction spectrometer fabrication. (a) A layer of PECVD silicon dioxide is first grown on the silicon substrate. (b) This is followed by DC magnetron sputtering of a niobium layer. (c) Next, gold contact pads are patterned onto the niobium. (d) An aluminum etched mask is fabricated. (e) The niobium is dry etched to pattern the device area. (f) The etched masked is removed.

double point contact spectrometry is investigation of protein alpha helixes. Though once believed to be inconsequential to enzymatic activity, experimental results indicated that fluctuations in the femtosecond and picosecond range are the origin of slow conformational changes[13, 67]. Many computer simulations of molecular dynamics are used to predict the vibrational frequencies of protein, but the lack of convincing experimental results (Raman and infrared spectroscopy, microwave absorption, inelastic neatron scattering, *etc.*) to verify the simulations is a major hindrance. Since the environment of proteins effects the damping of oscillations and not the frequency, double point contact spectrometry may be used to verify (or discard) experimentally any frequency predictions lying between 1 GHz and 10 THz.

To improve cancer diagnoses, imaging agents have been used for contrast enhancement in techniques such as magnetic resonance imaging (MRI) and laser photo therapy. While showing promise, these techniques have lagged with the lack of imaging agents. Since the human body is a natural source of THz radiation, this suggest potential application of double point contact spectrometry in non-invasive medical imaging.

APPENDIX A

BCS GROUND STATE

The BCS reduced Hamiltonian

$$H = \sum_{k,\sigma} \varepsilon_k c^{\dagger}_{k,\sigma} c_{k,\sigma} + \sum_{k,k',q,\sigma} \boldsymbol{V}_{k,k'} c^{\dagger}_{k,\sigma} c^{\dagger}_{-k,-\sigma} c_{-k',-\sigma} c_{k',\sigma} \tag{98}$$

takes into account only those properties of a system that are responsible for superconductivity. Having verified that an attractive interaction between electrons allows those electrons experiencing such interaction to occupy energy levels that were once forbidden, one may wonder how many of the system's quasi-particles experience this force.

From section 2 of Chapter 1 we saw that all electrons whose energy deviated from that of the Fermi energy an amount $E < \hbar\omega_q$ experienced an attractive force from electrons of opposite spin and momentum. The interaction of these electrons creates Cooper pairs, whose very presence lowers the energy of the system. As a result, the question of paramount importance would be, "What is the ground state energy of the system"? The question is answered by use of a variational principle.

Given the BCS reduced Hamiltonian of the system, a ground state wave function of the form:

$$|\psi> = \prod_{\boldsymbol{k}} (u_{\boldsymbol{k}} + v_{\boldsymbol{k}} c^{\dagger}_{\boldsymbol{k},\uparrow} c^{\dagger}_{-\boldsymbol{k},\downarrow}) |0> \tag{99}$$

was assumed. $v_{\boldsymbol{k}}$ is the probability that both states $|\boldsymbol{k},\uparrow>$ and $|\boldsymbol{k},\downarrow>$ are occupied, while $u_{\boldsymbol{k}}$ is the probability that at least one of the states is vacant. This physical interpretation immediately gives us a relation between $v_{\boldsymbol{k}}$ and $u_{\boldsymbol{k}}$, namely $u^2_{\boldsymbol{k}} + v^2_{\boldsymbol{k}} = 1$.

By allowing the BCS reduced Hamiltonian to operate on the above wave function an energy eigenvalue equation results. A variational method applied to this energy acts to determine the minimum energy of the system. This procedure results in the following two relations:

$$2u_{\boldsymbol{k}} v_{\boldsymbol{k}} = \frac{\Delta_{\boldsymbol{k}}}{E_{\boldsymbol{k}}}, \tag{100}$$

and

$$v_{\boldsymbol{k}}^2 - u_{\boldsymbol{k}}^2 = -\frac{\xi_{\boldsymbol{k}}}{E_{\boldsymbol{k}}}. \tag{101}$$

The term Δ_k satisfies the recurrence relation:

$$\Delta_k = -\frac{1}{2}\sum_{k'}(\frac{\Delta_k'}{E_{k'}})\boldsymbol{V}_{k'k}, \tag{102}$$

whereas $E_{\boldsymbol{k}}$ is given by:

$$E_{\boldsymbol{k}} = (\Delta_{\boldsymbol{k}}^2 + \xi_{\boldsymbol{k}}^2)^{\frac{1}{2}}. \tag{103}$$

In this expression $\xi_{\boldsymbol{k}}$ is the deviation of the energy from the Fermi energy ε_f.

APPENDIX B

CURRENT

In this section we will to develop an expression for the current, using a simple qualitative model. Once this expression is obtained, we will express the quantum mechanical equivalent form of the expression for current. This expression for current will allow us to introduce the Landauer scattering model to find an expression for the current, and ultimately the conductivity, in terms of what we call the transmission coefficients. The values are the coefficients, unique to each junction, and may be used to describe a particular junction. The set of transmission coefficients is called the PIN code of the junction.

We must mention in advance that while this formalism coupled with our ability to determine the PIN code of the junction allows us to completely describe the system, the formalism is somewhat incomplete. This may be evident by the fact that the system is not described fully in terms of fundamental constants. Although this formalism lacks the rigor of a theory based on first principles, it does serve the purposes of the authors group as well as the readers for two reasons. The author's group are able to determine the PIN code of the system with relative ease and therefore the simpler formalism provides enough insight for us to fully analyze our system. The readers see the Landauer formalism coupled with the concept of multiple Andreev reflection as much more of an intuitive picture than a first principles formalism.

To determine the current across an extremely small contact, we first model the system as two reservoirs separated by a channel with discrete energy levels. The energy levels of the reservoirs form energy bands as a result of their relatively large size. At equilibrium we assume the chemical potential of both of the reservoirs are the same. At absolute zero all energy levels below the chemical potential are filled, and all of those above the chemical potential are empty.

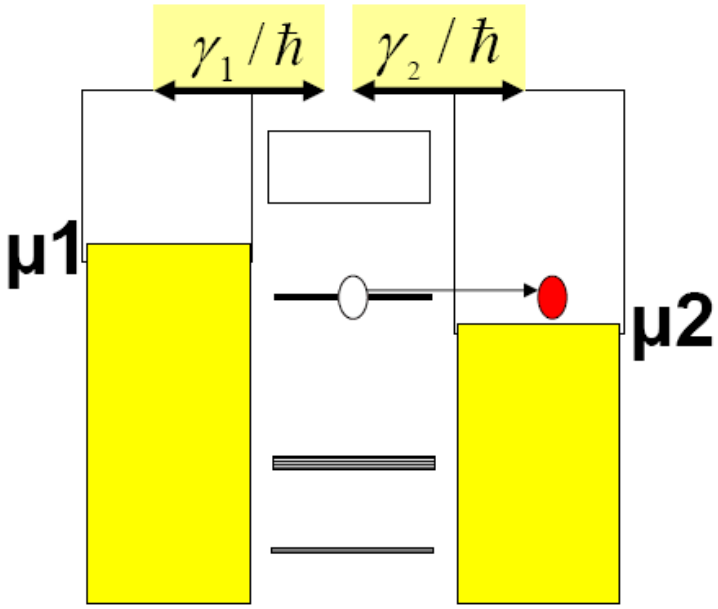

Figure 53: The left reservoir, whose chemical potential is μ_1 wishes to keep the energy level of the channel filled; while the right reservoir, chemical potential μ_2, wishes to keep this channel empty. As one reservoir supplies an electron to this available energy level, the other reservoir removes the electron. This continuous process creates current between the reservoirs.

Current arises when the reservoirs are not in equilibrium. This condition can be accomplished by applying a voltage difference across the reservoirs. The applied voltage will cause the two reservoirs to have different chemical potentials. Which reservoir has a greater chemical potential is not germane to the discussion. All that matters (almost all that matters) is that there is an energy difference between the reservoirs.

In order for current to flow between the reservoirs the channel must have an energy level between the chemical potentials of the reservoirs. The different objectives of each reservoir create the current. One reservoir wishes to keep the energy level of the channel filled, while the other reservoir wishes to keep the channel empty. As one reservoir supplies an electron to this available energy level, the other reservoir removes the electron. Thus we have current[55].

Although the qualitative discussion is interesting in and of itself, we wish to use this picture to develop the expression for the current used in equation (2). Our starting point is

the Fermi function, which will give us the average number of electrons in any energy level.

$$f(E-\mu) = \frac{1}{1+e^{(E-\mu)/k_BT}}. \tag{104}$$

At $T = 0K$, energy levels below μ have an occupancy of 1, and those above μ have an occupancy of 0. As the temperature is raised, energy levels slightly above μ begin to have an occupancy greater than 0, and those slightly below μ will have an occupancy slightly less than 1.

Each reservoir will have its own fermi function

$$f_1(E-\mu_1) = \frac{1}{1+e^{(E-\mu_1)/k_BT}}, \tag{105}$$

and

$$f_2(E-\mu_2) = \frac{1}{1+e^{(E-\mu_2)/k_BT}}. \tag{106}$$

Initially we expect a transient state as current starts flowing. Once we pass this and reach a steady state, the occupancy of the channel's energy level is N. The current flowing between the first reservoir and the channel will be proportional to the difference between the occupancy of the reservoir $f(E-\mu)$ and N. Therefore

$$I_1 = K_1(f_1 - N). \tag{107}$$

The current flowing between the channel and the second reservoir also may be expressed as:

$$I_2 = K_2(f_2 - N). \tag{108}$$

By noting that once the steady state is reached, we have

$$I_1 = -I_2, \tag{109}$$

and we dispense with the subscript and label the current I. By eliminating N from our two previous current equations, we see that:

$$I = \frac{K_1K_2}{K_1+K_2}[f_1 - f_2]. \tag{110}$$

Consequently we see that the current will be proportional to the difference in the Fermi functions of the reservoirs.

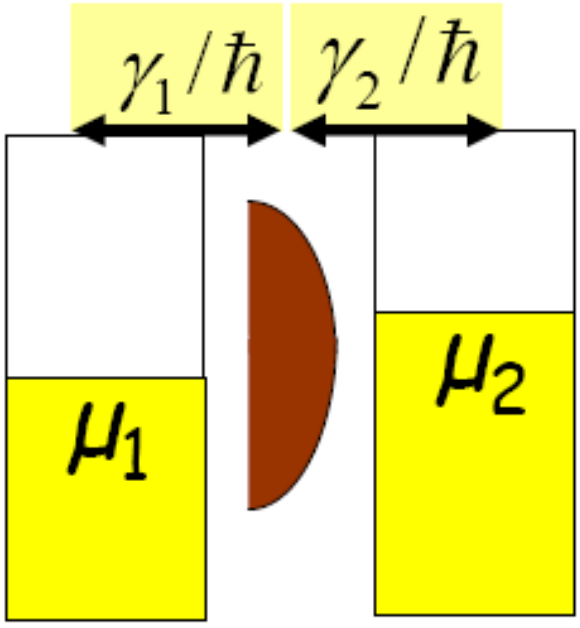

Figure 54: The left reservoir, whose chemical potential is μ_1, wishes to keep the energy band of the channel essentially empty; while the right reservoir, of chemical potential μ_2, wishes to keep this band practically filled. The broadening of the energy level to that of an energy band limits the total current that can pass between the reservoirs. Integration over the entire band will still give us one, the only difference is that this probability is not confined to a single energy (*i.e.*, a delta function) but is spread over a finite energy spectrum like that of a Gaussian.

The constants K_1 and K_2 are related to the coupling of the channel and the reservoirs. The expression that we have should lead us to the conclusion that the greater the coupling of the channel with the reservoir, the greater the current, with no apparent limit. From experiments we know that the maximum current that can be transmitted through a one level system is not infinite. We must take into account all the results of the coupling of the channel and the reservoirs.

To make the transition to the real situation, we note that the assumption that the channel has just one available energy level no longer holds true. The coupling of the channel with the reservoirs causes a broadening of the channels energy level. If we were to integrate over this broadened function we would still obtain 1, but not all of the levels may be between the chemical potentials of the two reservoirs[56].

Since the possible energy level is continuous, we expect that in order to express the current running through the channel we need to integrate the above expression over all energy levels between the chemical potential of the two reservoirs. As a consequence we obtain as expression of the form

$$I(t) = K \int_{\mu 1}^{\mu 2} dE(f_1 - f_2), \tag{111}$$

which is similar in form to equation (2), for a quantum system. The constant K in front of the integral must be related to the type of charge carriers we have along with the rate at which current is flowing across the channel.

APPENDIX C

CONTACT CAPACITANCE SIMULATIONS

In order to determine the capacitance of an atomic point contact "theoretically", we should be able to use Maxwell's equations coupled with boundary value conditions to determine the relationship between the charge on the contacts and the potential difference between the contacts. Due to the geometry of the problem, in practice this is much more difficult. Whereas a coaxial cable has symmetry that allows for the utilization of Legendre's polynomials, the atomic point contact has no such symmetry. We are forced to use computer simulations to determine the capacitance of the atomic point contact.

Our purpose is to learn how to operate COMSOL software in order to solve electromagnetic problems with extremely complicated geometries (i.e. difficult boundary conditions). We start off by testing COMSOL's ability to solve the most elementary of physics problems, the magnetic field created by a long straight current carrying wire. We want to use the software to draw the magnetic field lines of the current carrying wire. After this is complete we will move to slightly more difficult geometry, that of an open wire loop. COMSOL will be used in this situation to find the flux of the magnetic field through loop, which will help us find the inductance of loop. From the loop we then move to our primary objective, finding the magnetic field and ultimately the induction of a tantalum shunted junction, to determine if our shunted junction model in equation (70) is valid.

C.1 Case 1: Infinite Wire

C.1.1 Theoretical Expectation

All introductory physics textbooks cover the example of finding the magnetic field created by an infinite wire. This is usually done to show the usefulness of Ampere's Law.

$$\oint \boldsymbol{B} \cdot d\boldsymbol{l} = \mu_0 I. \tag{112}$$

By using this equation, we find that the magnetic field due to an infinite wire is

$$B = \frac{\mu_0 I}{2\pi r}. \tag{113}$$

The direction of the field is tangent to concentric circles drawn around the wire. The magnetic field lines due to an infinite wire are concentric circles whose center is the wire.

C.1.2 COMSOL Simulation

When using COMSOL we first must determine the dimensions of the problem and the module we wish to use to solve the problem. Although our infinite wire is a 3 dimensional problem, because the wire extends uniformly to infinity in the direction of its axis, we essentially have a 2 dimensional problem.

1. In the Model Navigator click on the New tab.
2. Select 2D in the Space Dimension list.
3. In the list of application modes, open the Electromagnetics module folder and then the Quasi-Statics, Magnetic folder. Double-click perpendicular induction current, vector potential.

This will send us to the drawing board. From here we must draw a cross sectional view of the wire.

1. Click the Circle/Elliptical button on the Draw toolbar. To draw a circle click the cross hair at the center of the drawing area and drag the cross hair to an adjacent diagonal grid and right click.
2. Click the Rectangle/Square button on the top of the Draw toolbar. Draw an arbitrary rectangle that contains the circle that we just drew. To do this we click in the drawing area and drag the mouse to another grid point, then right click.
3. Press Ctrl A.
4. Click Difference button on the draw toolbar.

Now that the geometry for our problem is set, we must specify the physical properties (*i.e.*, conduction properties):

1. Select the menu Physics ⇒ Boundary Settings.
2. Hold Ctrl button and select the three regions, by right clicking the mouse, that makes up the circumference of the circle on the draw screen.
3. Set boundary conditions to Surface Current.
4. For Surface Current density, enter 1.
5. Click OK.

Next we specify how we want our solution plotted. We have the option of streamlines, particle tracing, etc. Since we want the field lines plotted, we must choose streamlines.

1. Select the menu Postprocessing ⇒ Plot Parameters.
2. Select General tab.
3. Check streamline and Boundary boxes.
4. Uncheck the Slice box.
5. Click OK.
6. Select the menu Solve ⇒ Solve Problem.

C.2 Case 2: Wire Loop

C.2.1 Theoretical Expectation

In order to keep the COMSOL simulation simple we use the default dimensions. By doing this our wire loop has a length of 0.1 meters. This is essentially the length of a laboratory solenoid. Moreover we may determine the field of our loop by determining the field of a solenoid. By using Amperes Law and knowing some characteristics of a solenoid, we find that the magnitude of the magnetic field inside the loop is proportional to the current. In

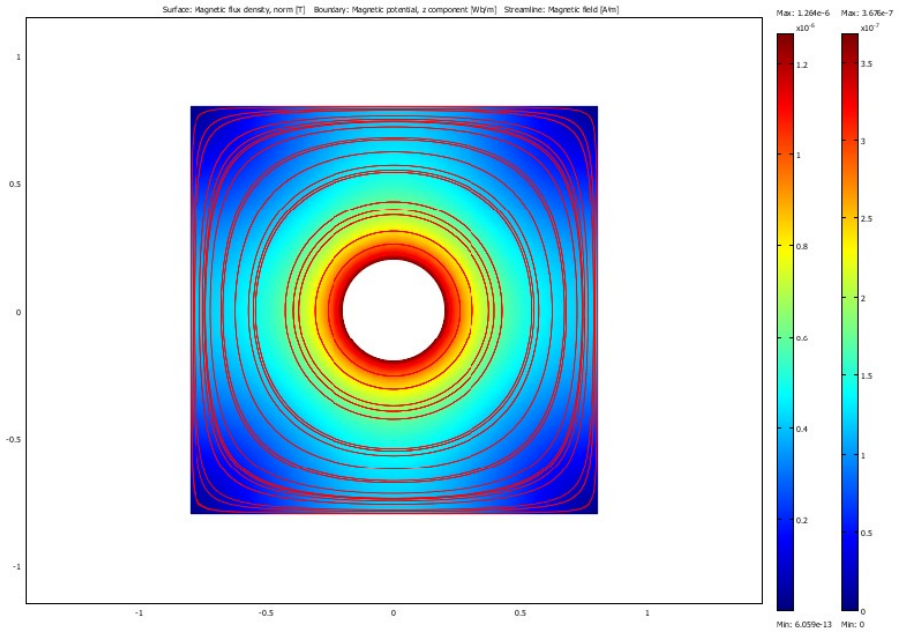

Figure 55: The simulated magnetic field lines due to an infinite wire carrying current.

our simulation we will be setting the voltage difference across the open ends of the open loop. The current, and thus the magnitude of the magnetic field, will be proportional to this potential difference. The most important feature of the wire loop is not the magnitude of the magnetic field, but of the fields resemblance to that of a permanent magnet. Thus in our COMSOL simulation we are looking for a magnetic field that resembles the magnetic field of a dipole whose north pole is perpendicular to the plane of the loop.

C.2.2 COMSOL Simulation

For the wire loop we must use a 3D work space. The drawing of the object will be similar to that of the infinite wire.

1. In the Model Navigator click on the New tab.
2. Select 3D in the Space Dimensions list.
3. In the list of application modes, open the Electromagnetics module folder and then the Quasi-statics, Electromagnetic folder. Double-click Electric and Induction Currents.

In order to draw the loop we must go to the work plane. This is a 2 dimensional space.

1. Select the menu Draw ⇒ Work Plane Settings.
2. Enter 0.05 for the z-coordinate and click OK.
3. Select menu Option ⇒ Axis/Grid Settings.
4. Select Grid tab and remove check from Auto box.
5. Enter 0.1 for x-spacing and 0.1 for y-spacing and click OK.
6. Select Ellipse/Circle (Centered) on the toolbar.
7. Click at center (0,0) and drag mouse to (0.6,0.6).
8. Draw another circle whose radius is 0.7 and concentric with the first circle.
9. Press Ctrl A.
10. Select Difference from the toolbar.

This should give us a flat loop. In order to create a current flow we will cut a small section out and apply a potential difference across the ends of the loop.

1. Select the menu Option ⇒ Axis/Grid Settings.
2. Enter 0.025 for both the x and y-spacing and click OK.
3. Zoom in on the lower part of the loop by clicking on the magnifying glass with a positive sign in the middle. Do this twice and scroll down.
4. Select Rectangle/Square from the toolbar.
5. Click at (-0.025,-0.575) and drag mouse to (0.025,-0.7).
6. Press Ctrl A.
7. Select Difference from the toolbar.
8. Zoom out back to original setting by clicking on the magnifying glass with the negative sign in the middle.

9. Return grid spacing back to 0.1.

Then we turn our 2 dimensional loop into a 3 dimensional loop. In order to be able to view the magnetic field lines, we will need to place our wire loop into a box.

1. Select the menu Draw ⇒ Extrude.
2. Enter 0.1 as the distance and click OK.
3. Select Block from the toolbar.
4. Select Center for the Base and enter 4 for the X, Y, and Z length.
5. Click OK.
6. Zoom out so that the entire block can be seen.
7. Press Ctrl A.
8. Select Difference from toolbar.
9. Select the menu Edit ⇒ Undo Difference.
10. Select menu Draw ⇒ Create Composite Object.
11. In Set Formula section replace the plus sign with a minus sign and click OK.

Next, since the geometry of our problem is set, we need to specify the physical characteristics of the wire loop. We will be using the default settings for the majority of the material.

1. Select the menu Physics ⇒ Boundary Settings.
2. Click Electric Parameters tab.
3. In Boundary selection choose 12 and for Boundary condition choose Electric potential.
4. Enter 10 for Electric potential.
5. In Boundary selection choose 15 and for Boundary conditions choose Electric potential.

6. Enter -10 for Electric potential.

7. For boundaries 6-11, 13-14, 16-17 choose electric insulation as the boundary condition.

8. Click OK.

9. Select the menu Options ⇒ Suppress ⇒ Suppress Boundaries.

10. Press Ctrl and select boundaries 1-5 and 18.

11. Click OK.

Finally we solve the problem. Before we can do this, we must specify how we want our solution plotted.

1. Select the menu Postprocessing ⇒ Plot Parameters.

2. Click General tab.

3. Check box for Streamline and Boundary.

4. Uncheck box for Slice.

5. Click OK.

6. Select the menu Solve ⇒ Solver Parameters.

7. Select Symmetric for Matrix Symmetry.

8. Click OK.

9. Select the menu Solve ⇒ Solve Problem.

C.3 Case 3: Circuit Element

The magnetic field from our previous examples are well known theoretically, so using COMSOL was similar to using a sledge hammer to kill an ant. The true power of COMSOL can be seen when we attempt to solve an electromagnetics problem whose geometry makes the boundary conditions difficult to solve for. The circuit element in fig. 1 falls into this category. We wish to find the magnetic field created by running current through this element, as well as the elements induction.

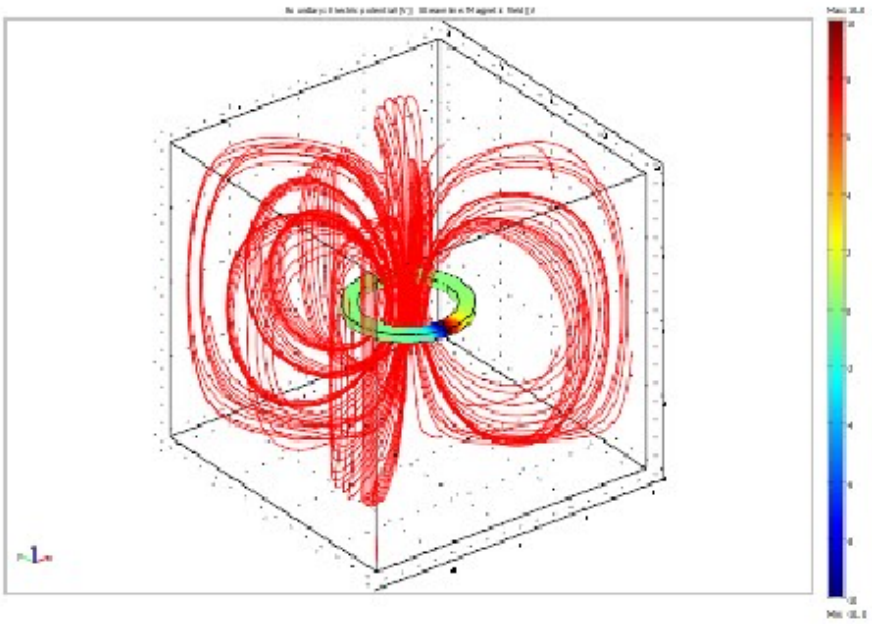

Figure 56: The simulated magnetic field lines from a ring carrying current.

C.3.1 COMSOL Simulation

Finding the magnetic field of the circuit element is similar to finding the magnetic field due to the wire loop. The main difference is that the size of the circuit element is about 6 orders of magnitude smaller.

1. In the Model Navigator click on the New tab.
2. Select 3D in the Space Dimensions list.
3. In the list of application modes, open the Electromagnetics module folder and then the Quasi-statics, Electromagnetic folder. Double-click Electric and Induction Currents.

We again go to the work plane. This is a 2 dimensional space which will make drawing the circuit element much easier. Before we begin to draw the object, we zoom in until the spacing in the work plane is 0.5 e-6. The key to this step is to make sure that the origin of the space, (0,0), stays on the screen.

1. Select the menu Draw ⇒ Work Plane Settings.
2. Enter 0.5e-7 for the z-coordinate and click OK.

3. Zoom in until spacing on the work plane is 0.5 e-6.

4. Select the menu Option ⇒ Axis/Grid Settings.

5. Select Grid tab and remove check from Auto box.

6. Enter 0.25e-6 for x-spacing and y-spacing and click OK.

7. Select line on the toolbar.

8. Draw a line from (-2e-6,7e-6) to (2e-6,7e-6) to (2e-6,5e-6) to (1.25e-6,5e-6) to (1.25e-6,-5e-6) to (2e-6,-5e-6) to (2e-6,-7e-6) to (2.5e-7,-7e-6) to (2.5e-7,-5e-6) to (1e-6,-5e-6) to (1e-6,5e-6) to (-1e-6,5e-6) to (-1e-6,-5e-6) to (-2.5e-7,-5e-6) to (-2.5e-7,-7e-6) to (-2e-6,-7e-6) to (-2e-6,-5e-6) to (-1.25e-6,-5e-6) to (-1.25e-6,5e-6) to (-2e-6,5e-6) to (-2e-6,7e-6).

This should give us a 2D view of the face of the circuit element. We will need to extrude this model by 1 e-7 in the z-direction.

1. Select the menu Draw ⇒ Extrude.

2. Enter 1e-7 as the distance and click OK.

3. Select Block from the toolbar.

4. Select Center for the Base and enter 8e-5 for the X, Y, and Z length.

5. Click OK.

6. Zoom out so that the entire block can be seen.

7. Press Ctrl A.

8. Select Difference from toolbar.

9. Select the menu Edit ⇒ Undo Difference

10. Select menu Draw ⇒ Create Composite Object.

11. In Set Formula section replace the plus sign with a minus sign and click OK.

The geometry of our problem is set, then we specify the physical characteristics of the circuit element.

1. Select the menu Physics ⇒ Boundary Settings.
2. Click Electric Parameters tab.
3. In Boundary selection choose 20 and for Boundary condition choose Electric potential.
4. Enter 10 for Electric potential.
5. In Boundary selection choose 7 and for Boundary conditions choose Electric potential.
6. Enter -10 for Electric potential.
7. For boundaries 6, 8-19, 21-27 choose electric insulation as the boundary condition.
8. Click OK.
9. Select the menu Options ⇒ Suppress ⇒ Suppress Boundaries.
10. Press Ctrl and select boundaries 1-5 and 28.
11. Click OK.

Before we solve the problem, we specify the material -titanium- of our circuit element.

1. Select the menu Physics ⇒ Subdomain Settings.
2. In the Subdomain Selection highlight 1.
3. Click the Load button.
4. Scroll down to Ti, highlight Ti and click OK.
5. Click OK.

Finally, we solve the problem after we specify how we want our solution plotted.

1. Select the menu Postprocessing ⇒ Plot Parameters.

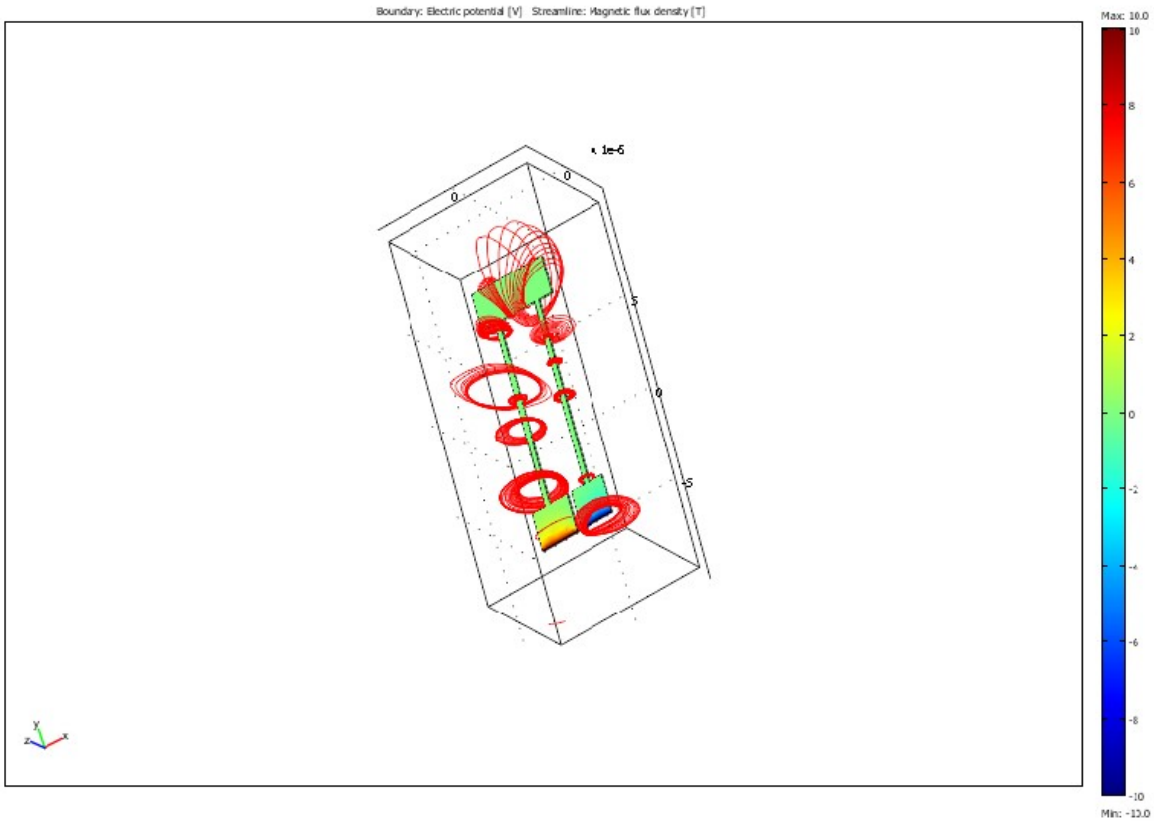

Figure 57: The simulated magnetic field lines from a single Tantalum shunt.

2. Click General tab.

3. Check box for Streamline and Boundary.

4. Uncheck box for Slice.

5. Click OK.

6. Select the menu Solve ⇒ Solver Parameters.

7. Select Symmetric for Matrix Symmetry.

8. Click OK.

9. Select the menu Solve ⇒ Solve Problem.

APPENDIX D

CONTACT STRUCTURAL AND DYNAMIC PROPERTIES

While our ability to determine the vibrational spectrum of the molecule between the contacts is based on the electric properties of the system, the question may arise as to whether these electronic properties are related to the structure of the molecule between the contacts. An answer in the affirmative would appear to be justified on the grounds that the electronic properties of a given atom are dependent on its valence electrons, and it is these electrons that are responsible for the chemical bonds, be they covalent or ionic, that form molecules. For example, the valence of fluorine is responsible for the atom's only forming single bonds and its ability to conduct electricity in a solution of aqueous hydrogen fluoride.

Aside from this apparent hand-waving justification, proof to the claim may be found in a comparison of the stiffness vs. contact elongation plot and conductance vs. contact elongation plot as illustrated in fig. 58. Since the stiffness of the contact is dependent on the arrangement of atoms between the contacts, a comparison of the two plots should make the claim of a relation between the electronic properties of the system and the configuration of molecule between the contacts plausible.

In fig. 58, the various steps in the stiffness plot are due to molecular rearrangements. Each of the steps corresponds to a step in the conductance plot of equal electrode displacement magnitude. This hints at a relation between the atomic configuration between the electrodes, and the transport properties of the junction. Therefore an investigation into the atomic configuration of the molecule between the contacts would be justified due to its effect on the transport properties of our junction.

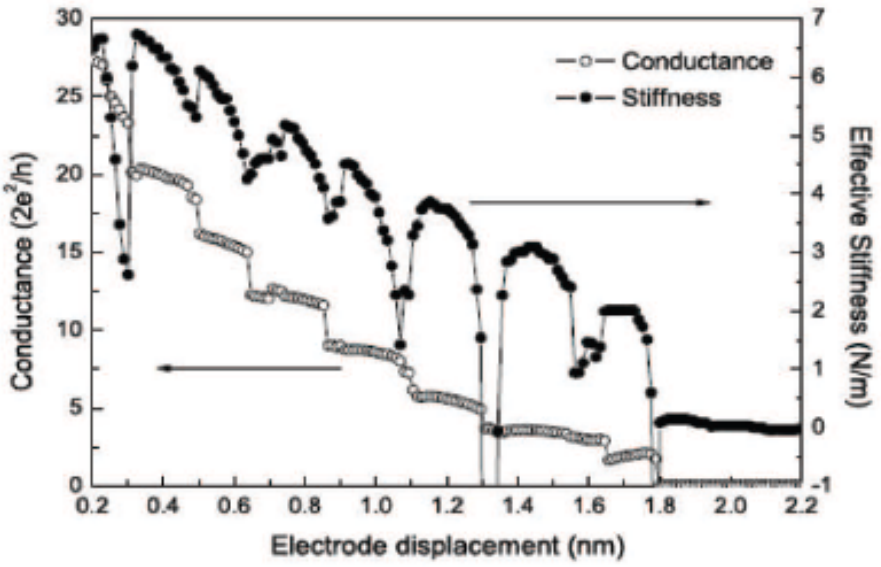

Figure 58: Illustrated is a simultaneous plot of stiffness vs. contact elongation and conductance vs. contact elongation. Each step in the stiffness plot is due to molecular rearrangement. The correspondence of steps on each plot implies that atomic structural rearrangements effect the transport properties of the junction.

D.1 Determination of the Niobium Dimer

A detailed plot of the conductance vs. contact elongation is illustrated in fig. 59. The previous comparison of the stiffness vs. contact elongation plot and conductance vs. elongation plot (*i.e.* fig. 58) lead to the conclusion that the abrupt jumps in conductance were due to atomic rearrangement between the contacts. The region of the plot labeled random telegraph noise (RTN) is where switching between two states of the system occurs. In order to obtain this region of the plot a time average of the two level fluctuations was taken.

For contact separation less than 0.33Å the system is in the high conductance (HG) state while for contact separation greater than 0.4Å the system is in the low conductance (LG) state. The high conductance state always has at least two conductance channels whose transmission coefficient is greater then 0.6, whereas the low conductance state only has one channel whose transmission coefficient is greater than 0.6. Although the LG state only has one conductance channel whose transmission coefficient is greater than 0.6, this transmission coefficient is always greater than that of any of the HG states transmission coefficients.

While fig. 59 sheds light on the existence of different states of the system, the plot

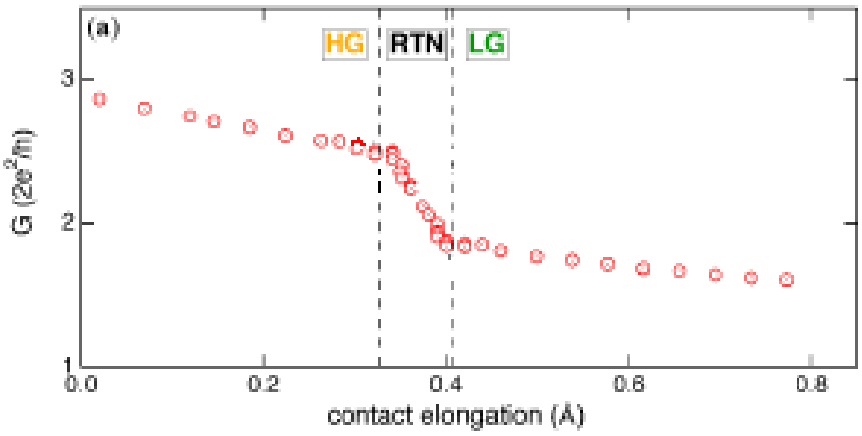

Figure 59: Illustrated is conductance versus contact elongation. We note the three regions corresponding to bulk contact, point contact, and tunneling regimes. The high conductance (HG) region corresponds to a shorter tip separation and a symmetric orientation of the molecule between the tips. The low conductance (LG) region corresponds to a greater tip separation and an asymmetric orientation of the molecule between the tips. The random telegraph noise (RTN) region is the separation distance in which switching between the two orientations is observed.

is less illuminating in concerns to details about the physical nature of these states. In order to determine the physical nature of the two states, density functional theory (DFT) structure simulations[20] coupled with non- equilibrium Green's function (NEGF) transport simulations[44] were used. The DFT/NEGF simulations resulted in one system reproducing the experimental results. This was that of a niobium dimer between the contacts. The LG state corresponded to an asymmetric positioning of the dimer between the contacts, whereas the HG state was due to the symmetric placing of the niobium dimer between the contacts. These results were also verified by use of SIESTA simulations [25].

Having established the existence of a niobium dimer between the contacts and its positioning during the two distinct states of the conductance vs. contact elongation plot, it remains to investigate the motion of the niobium dimer. We are compelled to do so on the assumption that the spectrum of the system will be dependent on not only the dimers positioning, but also its subsequent dynamical properties.

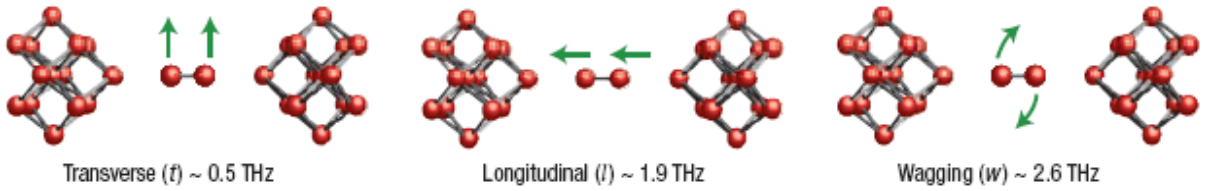

Figure 60: Illustrated are the three lowest vibrational frequencies of the niobium dimer between the contacts. The frequencies $f_t = 0.5$ THz (transverse mode), $f_l = 1.9$THz (longitudinal mode), and $f_w = 2.6$THz (wagging motion), would be expected to experience resonant coupling at voltages of 1.0mV, 3.9mV, and 5.4mV respectively.

D.2 Eigenmodes of the Niobium Dimer

In the primary text we likened the motion of the dimer between the contacts to that of child being pushed on a swing. The motion of the swing, in this ideal situation, is extremely confined, for the swing may only move back and forth. The motion of the dimer between the contacts is less constricted and thus more complicated.

By use of density functional theory calculations of the high conductance states, it was determined that the three lowest vibrational frequencies of the niobium dimer between the contacts are $f_t = 0.5$ THz (transverse mode), $f_l = 1.9$THz (longitudinal mode), and $f_w = 2.6$THz (wagging motion) as illustrated in fig. 60. The contact separation used for this simulation was 8.42Å. Adjustment of the contact separation to 7.73Å resulted in values for the three lowest vibrational frequencies of $f_t = 0.3$ THz, $f_l = 2.2$THz, and $f_w = 2.6$THz. This implies that the dimer's vibrational frequencies are not strongly dependent on the contact spacing.(Note: These three vibrational frequencies represent translational motion of the dimer and not intradimer stretching. The lowest frequency of intradimer stretching is 11.1THz.)

Since the peaks in the over-the-gap structure of the differential conductance vs. voltage plot are due to resonance between the Josephson current, whose frequency is $\omega_J (= \frac{2eV}{\hbar})$, and the vibrational frequencies of the niobium dimer, the three lowest resonance voltages should occur at 1.0mV, 3.9mV, and 5.4mV. The peaks that are observed in the differential conductance vs. voltage plot of fig. 47 correspond to the coupling of the Josephson current oscillations and the first and second harmonics of the longitudinal and wagging modes

of the dimer. (The peaks that would correspond to resonance between the Josephson current oscillations and the transverse mode are difficult to discern due to the second order multiple Andreev reflection peak located at 1.14mV.) That these peaks disappear once the temperature of the system is above the critical temperature leaves us confident with the resonance picture.

REFERENCES

[1] Abrikosov, A. *Zh. Eksp. Teor. Fiz.*, vol. 32, p. 1442, 1957.

[2] Abrikosov, A. *Sov. Phys. JETP*, vol. 5, p. 1174, 1957.

[3] Abrikosov, A. A., "On the magnetic properties of superconductors of the second group," *Sov. Phys. JETP*, vol. 5, pp. 1174–1182.

[4] Abrikosov, A., *Fundamentals of the Theory of Metals*. Amsterdam: North Holland, 1 ed., 1988.

[5] Abrikosov, A., Gor'kov, L., and Dzyaloshinski, I., *Methods of Quantum Field Theory in Statistical Physics*. Englewood Cliffs: Prentice Hall, 1 ed., 1963.

[6] Adkins, C., "Two-particle tunnelling between superconductors," *Philos. Mag.*, vol. 8, pp. 1051–1061, 1963.

[7] Agrait, N., Untiedt, C., Rubio-Bollinger, G., and Vieira, S., "Electron transport and phonons in atomic wires," *Chem. Phys.*, vol. 281, pp. 231–234, 2002.

[8] Agrait, N., Untiedt, C., Rubio-Bollinger, G., and Vieira, S., "Onset of dissipation in ballistic atomic wires," *Phys. Rev. Lett.*, vol. 88, p. 216803, 2002.

[9] Agrait, N., Yeyati, A. L., and van Ruitenbeek, J., "Quantum properties of atomic-sized conductors," *Phys. Rep.*, vol. 377, pp. 81–279, 2003.

[10] Ambegaokar, V. and Baratoff, A., "Tunneling between superconductors," *Phys. Rev. Lett.*, vol. 10, p. 486, 1963.

[11] Anderson, P. and Rowell, J., "Probable observation of the josephson superconductive tunneling effect," *Phys. Rev. Lett.*, vol. 10, pp. 230–232, 1963.

[12] Andreev, A. F. *Zh. Eksp. Teor. Fiz.*, vol. 46, p. 1823, 1964.

[13] Ansari, A., Berendez, J., Browne, S. F., Frauenfelder H., Iben, I. E. T., Sauke, T. B., Shyamsunder, E. and Young, R. D. "Protein States and Proteinquakes," *Proc. Natl. Acad. Sci USA*, vol. 82, pp. 5000–5004, 1985.

[14] Arnold, G., "Superconducting tunneling without the tunneling hamiltonian," *J. Low Temp. Phys.*, vol. 59, pp. 143–183, 1985.

[15] Ashcroft, N. and Mermin, N., *Solid State Physics*. Massachusetts: Brooks Cole, 1 ed., 1976.

[16] Averin, D. and Bardas, A., "Ac josephson effect in a single quantum channel," *Phys. Rev. Lett.*, vol. 75, p. 1831, 1995.

[17] Ballard, Joshua B., Carmichael, Erin S., and Shi, Dongxia, Lyding, Joseph W., Gruebele, Martin "Laser Absorption Scanning Tunneling Microscopy of Carbon Nanotubes," *Nano Letters*, vol. 6, pp. 45–49, 2006.

[18] Bardeen, J., Cooper, L. N., and Schrieffer, J. R., "Microscopic theory of superconductivity," *Phys. Rev.*, vol. 106, pp. 162–164, 1957.

[19] Bardeen, J., Cooper, L. N., and Schrieffer, J. R., "Theory of superconductivity," *Phys. Rev.*, vol. 108, p. 1175, 1957.

[20] Barnett, R. and Landman, U., "Born-oppenheimer molecular-dynamics simulations of finite systems: Structure and dynamics of $(H_2O)_2$," *Phys. Rev. B*, vol. 48, p. 2081.

[21] Beenakker, C., "Josephson current through a superconducting quantum point contact shorter than the coherence length," *Phys. Rev. Lett.*, vol. 66, pp. 3056–3059, 1991.

[22] Beenakker, C., "Three universal mesoscopic josephson effects," in *Proceedings of the 14th Taniguchi International Symposium on Transport Phenomena in Mesoscopic Systems* (Fukuyama, H. and Ando, T., eds.), pp. 235–253, Berlin: Springer, 1992.

[23] Beenakker, C., *Quantum Mesoscopic Phenomena and Mesoscopic Devices in Microelectronics*, pp. 51–60. NATO Science Series C559, Dordrecht: Kluwer, 2000.

[24] Berberich, P., Buemann, R., and Kinder, H., "Monochromatic phonon generation by the Josephson effect," *Phys. Rev. Lett.*, vol. 49, p. 1500–1503, 1982.

[25] Bidasaria, S., *Electronic and Mechanical Properties of Chemically Functionalized Nanowires*. PhD thesis, Georgia Institute of Technology, 2008.

[26] Binnig, G. and Rohrer, H., "Scanning tunneling microscopy," *IBM J. Res. Dev.*, vol. 30, p. 4, 1986.

[27] Binning, G., Quate, C. F., and Gerber, C., "Atomic force microscope," *Phys. Rev. Lett.*, vol. 56, p. 930, 1986.

[28] Blaney, T. G. and Bradley, C. C., "The josephson junction as a frequency analyser and mixer of submillimetre radiation sources," *J. Phys. D*, vol. 5, pp. 180–184.

[29] Blaney, T. G., Cross, N. R., and Knight, D. J. E., "Harmonic mixing and frequency measurement at 2.5 thz using josephson junctions," *J. Phys. D*, vol. 9, pp. 2175–2180, 1976.

[30] Blaney, T. G., Cross, N. R., Knight, D. J. E., Edwards, G. J., and Pearce, P. R., "Frequency measurement at 4-25 thz (70.5 μ) using a josephson harmonic mixer and phase-lock techniques," *J. Phys. D*, vol. 13, pp. 1365–1370, 1980.

[31] Blaney, T. G. and Knight, D. J. E., "Direct 825th harmonic mixing of a 1 ghz source with an hcn laser in a josephson junction," *J. Phys. D*, vol. 7, pp. 1882–1886, 1974.

[32] Blonder, G., Tinkham, M., and Klapwijk, T., "Transition from metallic to tunneling regimes in superconducting microconstrictions: Excess current, charge imbalance, and supercurrent conversion," *Phys. Rev. B*, vol. 25, pp. 4515–4532, 1982.

[33] Bogachek, E., Scherbakov, A., and Landman, U., "Magnetic switching and thermal enhancement of quantum transport through nanowires," *Phys. Rev. B*, vol. 53, p. R13246.

[34] Bogoliubov, N. *Nuovo Cimento*, vol. 7, p. 794, 1958.

[35] Born, M. and Oppenheimer, R., "On the quantum theory of molecules," *Annalen der Physik*, vol. 84, pp. 457–484, 1927.

[36] Brandbyge, J., Mozos, J., Ordejon, P., Taylor, J., and Stokbro, K., "Density-functional method for nonequilibrium electron transport," *Phys. Rev. B*, vol. 65, p. 165401.

[37] Brandbyge, M., Kobayashi, N., and Tsukada, M., "Conduction channels at finite bias in single-atom gold contacts," *Phys. Rev. B*, vol. 60, p. 17064.

[38] Brandbyge, M., Sorensen, M., and Jacobsen, K., "Conductance eigenchannels in nanocontacts," *Phys. Rev. B*, vol. 56, p. 14956.

[39] Brandbyge, M., Mozos, J.-L., Ordejon, P., Taylor, J., and Stokbro, K., "Density-functional method for nonequilibrium electron transport," *Phys. Rev. B*, vol. 65, p. 165401.

[40] Bratus, E., Shumeiko, V., Bezuglyi, E.V. and Wendin, G., "DC-current trasport and AC Josephson effect in quantum junctions at low voltages," *Phys. Rev. B*, vol. 55, pp. 12666–12677, 1997.

[41] Bratus, E., Shumeiko, V., and Wendin, G., "Theory of subharmonic gap structure in superconducting mesoscopic tunnel contacts," *Phys. Rev. Lett.*, vol. 74, pp. 2110–2113, 1995.

[42] Buttiker, M., Imry, Y., Landauer, R., , and Pinhas, S., "Generalized many-channel conductance formula with application to small rings," *Phys. Rev. B*, vol. 31, p. 6207, 1985.

[43] Chalmers, J. and Griffiths, P., *Handbook of Vibrational Spectroscopy*. Chichester: Wiley, 1 ed., 2002.

[44] Chang, C. and Landman, U. *to be published*.

[45] Chauvin, M., "Superconductingcting atomic contacts under microwave irradiation," *Phys. Rev. Lett.*, vol. 97, p. 067006, 2006.

[46] Cooper, L., "Bound electron pairs in a degenerate fermi gas," *Phys. Rev.*, vol. 104, pp. 1189–1190, 1956.

[47] Cron, R., *Atomic Contacts: A Testbed for Mesoscopic Superconductivity*. PhD thesis, University of Paris VI, 2001.

[48] Cuevas, J., Martin-Rodero, A., and Yeyati, A. L., "Hamiltonian approach to the transport properties of superconducting quantum point contacts," *Phys. Rev. B*, vol. 54, pp. 7366–7379, 1996.

[49] Cuevas, J., Yeyati, A. L., and Martin-Rodero, A., "Microscopic origin of conducting channels in metallic atomic-size contacts," *Phys. Rev. Lett.*, vol. 80, pp. 1066–1069, 1998.

[50] Dai, Z. and Marchenkov, A., "Subgap structure in resistively shunted superconducting atomic point contacts," *Appl. Phys. Lett.*, vol. 88, p. 203120.

[51] Dai, Z., Zhang, C., Barnett, R., Marchenkov, A., and Landman, U., "Structural and transport properties of niobium nanowires," *Phys. Stat. Sol. A*, vol. 204, pp. 1712–1720.

[52] Dai, Z., *Coherent and Dissipative Transport in Metallic Atomic-Size Contacts*. PhD thesis, Georgia Institute of Technology, 2006.

[53] Datta, S., "Nanoscale device simulation: The green's function method," *Superlattices and Microstructures*, vol. 28, pp. 253–278.

[54] Datta, S., "Non-equilibrium green's function (negf) formalism: An elementary introduction," *Proceedings of the International Electron Devices Meeting (IEDM).*

[55] Datta, S., *Electronic Transport in Mesoscopic Systems.* Combridge Universit Press: Cambridge, 1 ed., 1995.

[56] Datta, S., *Quantum Transport: Atom to Transistor.* Combridge Universit Press: Cambridge, 1 ed., 2005.

[57] de Bruyn Ouboter, R., "Superconductivity: Discoveries during the early years of low temperature research at leiden," *IEEE Trans. on Mag.*, vol. 23, pp. 355–370, 1987.

[58] de Gennes, P., *Superconductivity of Metals and Alloys.* Colorado: Westview Press, 2 ed., 1999.

[59] Deutscher, G. and de Gennes, P. G., *Superconductivity.* New York: Marcel Dekker, 1 ed., 1969.

[60] Dirac, P., "The quantum theory of emission and absorption of radiation," *Proc. Roy. Soc. London A*, vol. 114, pp. 243–265, 1927.

[61] Divin, Y. Y., Polyanski, O. Y., and Shul'man, A. Y. *Sov. Tech. Phys. Lett.*, vol. 6, pp. 454–457.

[62] Divin, Y. Y., Pavlovshi, V. V., Volkov, O. Y., Schulz, H., Poppe, U., Klein, N., and Urban, K., "Hilbert-transform spectral analysis of millimeter- and submillimeter-wave radiation with high t_c josephson junctions," *IEEE Trans. Appl. Super.*, vol. 7, pp. 3426–3429.

[63] Donehoo, B., *A Superconducting Investigation of Nanoscale Mechanics in Niobium Quantum Point Contacts.* PhD thesis, Georgia Institute of Technology, 2008.

[64] Djukic, D., Thygesen, K. S., Untiedt, C., R. H. M. Smit, K. W. J., and van Ruitenbeek, J., "Stretching dependence of the vibration modes of a single-molecule pth[sub 2]pt bridge," *Phys. Rev. B*, vol. 71, pp. 161402–161404, 2005.

[65] Dobbs, J. N., Anderson, A. C., Metzger, T. H., and Wipf, H., "Low temperature thermal expansion of niobium containing trapped hydrogen," *Phys. Rev. B*, vol. 30, pp. 6168–6169.

[66] Dobroiu, A., Yamashita, M., Ohshima, Y. N., Morita, Y., Otani, C., and Kawase, K., "The backward wave oscillator as a radiation source in terahertz imaging," in *Infrared and Millimeter Waves, 2004 and 12th International Conference on Terahertz Electronics*, 2004.

[67] Dornmair, K., Jahnig, F., "Internal dynamics of lactose permease," *Proc. Natl. Acad. Sci. USA*, vol. 86, pp. 9827–9831 1989.

[68] Dreizler, R. and Gross, E., *Density Functional Theory*. Plenum Press: New York, 1 ed., 1995.

[69] Eigler, D., Lutz, C., and Rudge, W., "An atomic switch realized with the scanning tunnelling microscope," *Nature*, vol. 352, p. 600.

[70] Feynman, R. P., Leighton, R., and Sands, M., *The Feynman Lectures on Physics*, vol. 3, pp. 21–14. Massachusetts: Addison-Wesley, 1965.

[71] Finnemore, D. K., Stromberg, T. F., , and Swenson, C. A., "Superconducting properties of high purity niobium," *Phys. Rev.*, vol. 149, pp. 231–243.

[72] Fiolhais, C., Nogueira, F., and Marques, M., *A Primer in Density Functional Theory*. Springer-Verlag, 1 ed., 2003.

[73] Fiske, Milan D., "Temperature and Magnetic Field Dependence of the Josephson Tunneling Current," *Review of Modern Physics*, vol. 36, pp. 221-222, 1964.

[74] Coon, D. D., Fiske, Milan D., "Josephson ac and Step Structure in the Supercurrent Tunneling Characteristic," *Physical Review*, vol. 138, pp. A744-A746, 1965.

[75] Fossheim, K. and Sudbo, A., *Superconductivity: Physics and Applications*. New York: Wiley, 1 ed., 2007.

[76] Furusaki, A., "A unified theory of clean josephson junctions," *Physica B*, vol. 165, pp. 967–968, 1990.

[77] Galperin, M., Ratner, M., and Nitzan, A., "Molecular transport junctions: vibrational effects," *J. Phys: Conden. Matter*, vol. 19, p. 103201, 2007.

[78] Gimzewski, J. K., Moller, R., Pohl, D., and Schlittler, R., "Transition from tunneling to point contact investigated by scanning tunneling microscopy and spectroscopy," *Surf. Sci.*, vol. 189/190, p. 15.

[79] Gimzewski, J. and Moller, R., "Transition from the tunneling regime to point contact studied using scanning tunneling microscopy," *Physica B*, vol. 36, pp. 1284–1287, 1987.

[80] Gronbeck, H., Rosen, A., and Andreoni, W., "Structural, electronic, and vibrational properties of neutral and charged Nb_n(n=8,9,10) clusters," *Phys. Rev. A*, vol. 58, p. 4630.

[81] Haberkorn, W., Knauer, H., and Richter, J., "A theoretical study of the current-phase relation in josephson contacts," *Phys. Stat. Sol.*, vol. 47, pp. K161–K164, 1978.

[82] Hahn, A. and Humpfner, K., "Nonequilibrium in normal-conductor/superconductor microconstrictions," *Phys. Rev. B*, vol. 51, p. 3660.

[83] Hahn, J., Lee, H., and Ho, W., "Electronic resonance and symmetry in single-molecule inelastic electron tunnelling," *Phys. Rev. Lett.*, vol. 85, pp. 1914–1917, 2000.

[84] Hakkinen, H., Barnett, R., Scherbakov, A., and Landman, U., "Nanowire gold chains: Formation mechanisms and conductance," *J. Phys. Chem. B*, vol. 104, p. 9063.

[85] Hansma, P., *Tunneling Spectroscopy.* Plenum Press, New York, 1 ed., 1982.

[86] Heinzel, T., *Mesoscopic Electronics in Solid State Nanostructures.* New York: Wiley, 1 ed., 2007.

[87] Hekking, F. W. J., Schn, G., and Averin, D. V. in *Proceedings of the NATO Advanced Research Workshop on Mesoscopic Superconductivity*, 1994.

[88] Hopkins, B. J. and Ross, K. J., "The contact potential difference between tungsten and niobium," *J. Appl. Phys.*, vol. 15, pp. 89–92, 1964.

[89] Hu, B. B. and Nuss, M. C., "Imaging with terahertz waves," *Opt. Lett.*, vol. 20, p. 1716, 1995.

[90] Humphreys, K., Loughran, J. P., Gradziel, M., Lanigan, W., Ward, T., Murphy, J., and OSullivan, C., "Medical applications of terahertz imaging: a review of current technology and potential applications in biomedical engineering," in *Proceedings of the 26th Annual International Conference of the IEEE EMBS*, pp. 1302–1305, 2004.

[91] Jackson, B. and Klapwijk, T., "The current status of low-noise thz mixers based on sis junctions," *Physica C*, vol. 372–376, pp. 368–373, 2002.

[92] Jansen, A., van Gelder, A., and Wyder, P., "Point contact spectroscopy in metals," *J. Phys. C*, vol. 13, pp. 6073–6118, 1980.

[93] Josephson, B., "Possible new effects in superconductive tunneling," *Phys. Lett.*, vol. 1, pp. 251–253, 1962.

[94] Josephson, B., *Superconductivity*, vol. 1, ch. Weakly Coupled Superconductors. New York: Marcel Dekker, 1969.

[95] Kanter, H., Vernon Jr., F.L., "High-Frequency Response of Josephson Point Contacts," *J. Appl. Phys.*, vol. 43, pp. 3174-3182, 1972.

[96] Kim, Y. B., Hempstead, C., and Strnad, A., "Flux flow resistance in type ii superconductors," *Phys. Rev.*, vol. 139, pp. 1163–1172, 1965.

[97] Kittel, C., *Introduction to Solid State Physics*. New York: Wiley, 8 ed., 2004.

[98] Klapwijk, T., "Proximity effect from an andreev perspective," *J. Supercond.: Incorporating Novel Magnetism*, vol. 17, pp. 593–611, 2004.

[99] Klapwijk, T., Blonder, G., and Tinkham, M., "Explanation of subharmonic energy gap structure in superconducting contacts," *Physica B*, vol. 109, pp. 1657–1664, 1982.

[100] Kohanoff, J., *Electronic Structure Calculations for Solids and Molecules: Theory and Computational Methods*. Cambridge University Press, 1 ed., 2006.

[101] Kohn, W. and Sham, L. J., "Self-consistent equations including exchange and correlation effects," *Phys. Rev.*, vol. 140, pp. A1133–A1138.

[102] Kolesnychenko, O. Y., S., I., O., and van Kempen, H., "Calibration of the distance between electrodes of mechanically controlled break junctions using field-emission resonance," *Rev. Sci. Instrum.*, vol. 70, pp. 1442–1446, 1999.

[103] Kooi, J., Chan, M., Bumble, B., LeDuc, H., Schaffer, P., and Phillips, T., "230 and 492 ghz low-noise sis waveguide receivers employing tuned nb/alox/nb tunnel junctions," *Int. J. IR MM Waves*, vol. 16, p. 2049, 1995.

[104] Kosarev, E. L., Shulman, A. Y., A.Tarasov, M., and Lindstrom, T., "Deconvolution problems and superresolution in hilbert transform spectroscopy based on ac josephson efect," *Modern Trends in Computational Physics*.

[105] Kulik, I., "Macroscopic quantization and the proximity effect in s-n-s junctions," *Sov. Phys. JETP*, vol. 30, pp. 944–950, 1970.

[106] Kulik, I., Omel'yanchuk, A., and Shekhter, R., "Electrical conductivity of point microbridges and phonon and impurity spectroscopy in normal metals," *Sov. J. Low Temp. Phys.*, vol. 3, pp. 740–748, 1977.

[107] Landau, L., "The theory of a fermi liquid," *Sov. Phys. JETP*, vol. 3, pp. 920–925, 1957.

[108] Landau, L., "On the theory of a fermi liquid," *Sov. Phys. JETP*, vol. 8, pp. 70–74, 1959.

[109] Landauer, R., "Spatial variation of currents and fields due to localized scatterers in metallic conduction," *IBM J. Res. Dev.*, vol. 1, pp. 223–231, 1957.

[110] Landman, U., Luedtke, W., Burnham, N., and Colton, R., "Atomistic mechanisms and dynamics of adhesion, nanoindentation, and fracture," *Science*, vol. 248, pp. 454–461, 1990.

[111] Landman, U., Luedtke, W., Salisbury, B., and Whetten, R., "Reversible manipulations of room temperature mechanical and quantum transport properties in nanowire junctions," *Phys. Rev. Lett.*, vol. 77, p. 1362, 1996.

[112] Lang, N. D., "Resistance of a one-atom contact in the scanning tunneling microscope," *Phys. Rev. B*, vol. 36, p. 8173.

[113] Langenberg, D. N., Parker, W. H., and Taylor, B. N., "Experimental test of the Josephson frequency-voltage relation," *Phys. Rev.*, vol. 150, p. 186–188, 1966.

[114] Lanigan, W., Murphy, J., May, R., Mahon, R., McAuley, I., Markham, C., Humphries, K., Ward, T., and Withington, S., "Quasi-optical millimetre-wave imaging with bio-medical applications," in *IRMMW-THz*, 2005.

[115] Laqua, K., Melhuish, W.H., and Zander, M., "Molecular Absorption Spectroscopy, Ultraviolet and Visible (UV/VIS)," *IUPAC*, vol. 191, pp. 485–504, 1988.

[116] LeRoy, B. J., Lemay, S. G., Kong, J., and Dekker, C., "Electrical generation and absorption of phonons in carbon nanotubes," *Nature*, vol. 432, pp. 371–374, 2004.

[117] Likharev, K., "Superconducting weak links," *Rev. Mod. Phys.*, vol. 51, pp. 101–159, 1979.

[118] Likharev, K., *Dynamics of Josephson Junctions and Circuits*. Russia: Gordon and Breach Publishers, 1 ed., 1986.

[119] Lindsay, S. M. and Ratner, M. A., "Molecular transport junctions: Clearing mists," *Adv. Mat.*, vol. 19, pp. 23–31, 2007.

[120] London, F. and London, H., "The electromagnetic equations of the supraconductor," *Proc. R. Soc. London A*, vol. 149, pp. 71–88, 1935.

[121] Ludolph, B., "Multiple Andreev reflection in single atom niobium junctions," *Phys. Rev. B*, vol. 61, p. 8561–8569, 2000.

[122] Ludolph, B., Devoret, M., Esteve, D., Urbina, C., and van Ruitenbeek, J., "Evidence for saturation of channel transmission from conductance fluctuations in atomic-size point contacts," *Phys. Rev. Lett.*, vol. 82, p. 1530.

[123] Marchenkov, A., Dai, Z., Zhang, C., Barnett, R., and Landman, U., "Atomic dimer shuttling and two-level conductance fluctuations in Nb nanowires," *Phys. Rev. Lett.*, vol. 98, 046802, 2007.

[124] Marchenkov, A., Dai, Z., Donehoo, B., Barnett, R., and Landman, U., "Alternating current josephson effect and resonant superconducting transport through vibration nb nanowires," *Nature Nanotech.*, vol. 2, pp. 481–485.

[125] Marder, M., *Condensed Matter Physics*. New York: Wiley, 1 ed., 2000.

[126] Martin, T. and Landauer, R., "Wave-packet approach to noise in multichannel mesoscopic systems," *Phys. Rev. B*, vol. 45, p. 1742, 1987.

[127] Martin-Rodero, A., Garcia-Vidal, F., and Yeyati, A. L., "Microscopic theory of josephson mesoscopic constrictions," *Phys. Rev. Lett.*, vol. 73, pp. 554–557, 1994.

[128] Martinis, J. M., Devoret, M. H., and Clarke, J., "Experimental tests for the quantum behavior of a macroscopic degree of freedom: The phase difference across a josephson junction," *Phys. Rev. B*, vol. 35, pp. 4682–4698, 1987.

[129] Maslov, D. L., Barnes, C., and Kirczenow, G., "Ballistic transport in a disordered environment: Why is conductance quantization observable?," *Phys. Rev. Lett.*, vol. 70, p. 1984.

[130] Mattheiss, L. F., "Electronic structure of niobium and tantalum," *Phys. Rev. B*, vol. 1, pp. 373–380.

[131] Mattis, D. and Bardeen, J., "Theory of the anomalous skin effect in normal and superconducting metals," *Phys. Rev.*, vol. 111, pp. 412–417, 1958.

[132] McCumber, D. E., "Effect of AC Impedance on DC Voltage-Current Characteristics of Superconductor Weak-Link Junctions," *Jour. of Appl. Phys.*, vol. 39, pp. 3113–3118, 1968.

[133] McDonald, D. G., Evenson, K. M., Wells, J. S., , and Cupp, J. D., "High-frequency limit of the josephson effect," *J. Appl. Phys.*, vol. 42, pp. 179–181, 1971.

[134] McDonald, D. G., Evenson, K. M., Wells, J. S., and Cupp, J. D., "High-frequency limit of the josephson effect," *J. Appl. Phys.*, vol. 42, pp. 179–181, 1971.

[135] Meissner, W. and Ochsenfeld, R., "Ein neuer effekt bei eintritt der supraleifahigkeit," *Naturwiss.*, vol. 21, pp. 787–788, 1933.

[136] Milliken, F. P., Rozen, J. R., Keefe, G. A., and Koch, R. H., "50 ohm characteristic impedance low-pass metal powder filters," *Rev. Sci. Instrum.*, vol. 78, p. 024701, 2007.

[137] Minin, I. and Minin, O., "Recent developments in active millimeter/thz waves high-quality 3d imaging for scientific, medical and homeland secuttry applications," in *5th IEEE - Russia Conference: MEMIA'2005*, 2005.

[138] Moreland, J. and Ekin, J., "Electron tunneling experiments using nb-sn break junctions," *J. Appl. Phys.*, vol. 58, pp. 3888–3895, 1985.

[139] Morkoc, H., *Advanced Semiconductors and Organic Nano-Techniques.* Academics Press, New York, 1 ed., 2003.

[140] Muller, C., van Ruitenbeek, J., and de Jongh, L., "Conductance and supercurrent discontinuities in atomic-scale metallic constrictions of variable width," *Phys. Rev. Lett.*, vol. 69, pp. 140–143, 1992.

[141] Muller, C., van Ruitenbeek, J., and de Jongh, L., "Experimental observation of the transition from weak link to tunnel junction," *Physica C*, vol. 191, pp. 485–504, 1992.

[142] Naidyuk, Y. and Yanson, I., *Point-Contact Spectroscopy*. Springer, New York, 1 ed., 2004.

[143] Negele, J. and Orland, H., *Quantum Many-Particle Systems*. Massachusetts: Addison Wesley, 1 ed., 1988.

[144] Nguyen, C., Kroemer, H., and Hu, E. L., "Anomalous andreev conductance in InAs-AlSb quantum well structures with Nb electrodes," *Phys. Rev. Lett.*, vol. 69, p. 2847.

[145] Octavio, M., Tinkham, M., Blonder, G., and Klapwijk, T., "Subharmonic energy-gap structure in superconducting constrictions," *Phys. Rev. B*, vol. 27, pp. 6739–6746, 1983.

[146] Ohnishi, H., Kondo, Y., and Takayanagi, K., "Quantized conductance through individual rows of suspended gold atoms," *Nature*, vol. 395, p. 780.

[147] Onnes, H. K. Comm. Leiden, 1908. 108.

[148] Onnes, H. K., "The disappearance of the resistivity of mercury," *Comm. Leiden*, May 1911.

[149] Onnes, H. K., "On the sudden change in the rate at which the resistance of mercury disappears," *Comm. Leiden*, November 1911.

[150] Onnes, H. K., "The resistance of pure mercury at helium temperatures," *Comm. Leiden*, April 1911.

[151] Osakabe, N., Matsuda, T., Kawasaki, T., Endo, J., Tonomura, A., Yano, S., and Yamada, H., "Experimental confirmation of aharonov-bohm effect using a toroidal magnetic field confined by a superconductor," *Phys. Rev. A*, vol. 34, pp. 815–822, 1986.

[152] Pannetier, B. and Courtois, H., "Andreev reflection and proximity effect," *J. Low Temp. Phys.*, vol. 118, pp. 599–615, 2000.

[153] Parr, R. G. and Yang, W., *Density-Functional Theory of Atoms and Molecules*. Oxford University Press, New York, 1 ed., 1989.

[154] Phillips, P., *Advanced Solid State Physics*. Colorado: Westview Press, 1 ed., 2003.

[155] Pobell, F., *Matter and Methods at Low Temperatures*. New York: Springer, 2 ed., 2002.

[156] Pothier, H., *Coulomb Blockade and Single Electron Transfer*. PhD thesis, University of Paris VI, 1991.

[157] Rodrigues, V. and Ugarte, D., "Real-time imaging of atomistic process in one-atom-thick metal junctions," *Phys. Rev. B*, vol. 63, p. 073405.

[158] Rubio-Bollinger, G., Bahn, S. R., Agrait, N., Jacobsen, K. W., and Vieira, S., "Mechanical properties and formation mechanisms of a wire of single gold atoms," *Phys. Rev. Lett.*, vol. 87, p. 026101.

[159] Rubio-Bollinger, G., Joyez, P., and Agrat, N., "Metallic adhesion in atomic-size junctions," *Phys. Rev. Lett.*, vol. 93, p. 116803.

[160] Scheer, E., Agrait, N., Cuevas, J., Yeyati, A. L., Ludoph, B., Martín-Rodero, A., Bollinger, G. R., van Ruitenbeek, J., and Urbina, C., "Theory of subharmonic gap structure in superconducting mesoscopic tunnel contacts," *Phys. Rev. Lett.*, vol. 74, pp. 2110–2113, 1995.

[161] Scheer, E., Agrait, N., Cuevas, J., Yeyati, A. L., Ludoph, B., Martin-Rodero, A., Bollinger, G. R., van Ruitenbeek, J., and Urbina, C., "The signature of chemical valence in the electrical conduction through a single-atom contact," *Nature*, vol. 394, pp. 154–157, 1998.

[162] Scheer, E., Joyez, P., Esteve, D., Urbina, C., and Devoret, M., "Conduction channel transmissions of atomic-size aluminum contacts," *Phys. Rev. Lett.*, vol. 78, pp. 3535–3538, 1997.

[163] Schrieffer, J. and Wilkins, J., "Two-particle tunneling processes between superconductors," *Phys. Rev. Lett.*, vol. 10, pp. 17–20, 1963.

[164] Shapiro, S. "Josephson currents in superconducting tunneling: The effect of microwaves and other observations," *Phys. Rev. Lett.*, vol. 11, p. 80, 1963.

[165] Sharvin, Y. *Sov. Phys. JETP*, vol. 21, p. 655, 1965.

[166] Shul'man, A.Ya., Kosarev, E.L., Tarasov, M.A., "Hilbert-Transform Spectroscopy Based on the a.c. Josephson Effect. Theory and Computational Technique," *Journal of Communications Technology and Electronics*, vol. 48, pp. 1124-1136, 2003.

[167] Smith, D. P. E., "Quantum point contact switches," *Science*, vol. 269, p. 371, 1995.

[168] Stalder, A. and Durig, U., "Study of yielding mechanics in nanometer-sized au contacts," *Appl. Phys. Lett.*, vol. 68, p. 637.

[169] Stipe, B. C., Rezaei, M. A., and Ho, W., "Single-molecule vibrational spectroscopy and microscopy," *Science*, vol. 280, pp. 1732–1735, 1998.

[170] Swihart, J. C., "Field Solution for a Thin-Film Superconducting Strip Transmission Line," *J. Appl. Phys*, vol. 32, pp. 461–469, 1961.

[171] Taylor, B. and Burstein, E., "Excess currents in electron tunneling between superconductors," *Phys. Rev. Lett.*, vol. 10, pp. 14–17, 1963.

[172] Taylor, J., Guo, H., and Wang, J., "Real-time imaging of atomistic process in one-atom-thick metal junctions," *Phys. Rev. B*, vol. 63, p. 073405.

[173] Terabe, K., Hasegawa, T., Nakayama, T., and Aono, M., "Quantized conductance atomic switch," *Nature*, vol. 433, p. 47.

[174] Tinkham, M., *Introduction to Superconductivity.* New York: Dover, 2 ed., 1996.

[175] Trauble, H. and Essman, U., "Flux-line arrangement in superconductors as revealed by direct observation," *J. Appl. Phys.*, vol. 39, pp. 4052–4059.

[176] Tucker, J. R., "Quantum limited detection in tunnel junction mixers," *IEEE J. Quant. Elec.*, vol. 15, pp. 1234–1258, 1979.

[177] Untiedt, C., Bollinger, G. R., Vieira, S., and Agrait, N., "Quantum interference in atomic-sized point contacts," *Phys. Rev. B*, vol. 62, pp. 9962–9965.

[178] Valatin, J. *Nuovo Cimento*, vol. 7, p. 843, 1958.

[179] Valkering, A. M. C., Mares, A. I., Untiedt, C., Gavan, K. B., Oosterkamp, T. H., and van Ruitenbeek, J. M., "A force sensor for atomic point contacts," *Rev. Sci. Instrum.*, vol. 76, p. 103903.

[180] van der Post, N., Peters, E., Yanson, I., and van Ruitenbeek, J., "Subgap structure as function of the barrier in atom-size superconducting tunnel junctions," *Phys. Rev. Lett.*, vol. 73, pp. 2611–2613, 1994.

[181] van Duzer, T. and Turner, C., *Superconductive Devices and Circuits*. New Jersey: Prentice Hall, 1 ed., 1999.

[182] van Wees, B., van Houten, H., Beenakker, C., Williamson, J., Kouwenhoven, L., van der Marel, D., and Foxon, C., "Quantised conductance of point contacts in a two-dimensional electron gas," *Phys. Rev. Lett.*, vol. 60, pp. 848–850, 1988.

[183] Vanneste, C, Chi, C.C., Brown, K.H., Callegari, A.C., Chen, M.M., Greiner, J.H., Jones, H.C., Kim, K.K., Kleinsasser, A.W., Notarys, H.A., Proto, G., Wang, R.H. and Yogi, T., "*IV* characteristics of microwave-driven Josephson junctions in the low-frequency and high-damping regime," *Phys. Rev. B*, vol. 31, pp. 4230–4233, 1985.

[184] Walmsley, D. G. and Tomlin, J. L., "Compilation of inelastic electron tunnelling spectra of molecules chemisorbed on metal oxides," *Prog. Surf. Sci.*, vol. 18, p. 247, 1985.

[185] Wang, W., Lee, T., Kretzschmar, I., and Reed, M. A., "Inelastic electron tunnelling spectroscopy of alkanedithiol self-assembled monolayers," *Nano. Lett.*, vol. 4, pp. 643–646, 2004.

[186] Westbrook, P. S. and Javan, A., "Finite-bias resistance peaks in nanoscale superconductor-normal metal ta-w point contacts," *Phys. Rev. B*, vol. 59, pp. 606–611.

[187] Wu, P., Wang, H., Cheng, Q., and Xu, W., "Harmonic frequency mixing at millimeter waveband using high tc josephson junction and its applications," *Physica C*, vol. 282–287, pp. 399–402, 1997.

[188] Xiong, P., Xiao, G., and Laibowitz, R. B., "Subgap and above-gap differential resistance anomalies in superconductor-normal-metal microjunctions," *Phys. Rev. Lett.*, vol. 71, p. 1907.

[189] Yannouleas, C., Bogachek, E., and Landman, U., "Energetics, forces, and quantized conductance in jellium-modeled metallic nanowires," *Phys. Rev. B*, vol. 57, p. 4872.

[190] Yanson, A., Rubio-Bollinger, G., van der Brom, H., Agrait, N., and van Ruitenbeek, J., "Formation and manipulation of a metallic wire of single gold atoms," *Nature*, vol. 395, p. 783.

[191] Yanson, I., "Nonlinear effects in the electric conductivity of point junctions and electron-phonon interaction in metals," *Zh. Eksp. Teor. Fiz.*, vol. 74, pp. 1035–1050, 1966.

[192] Yeyati, A. L., Martin-Rodero, A., and Vidal, F. G., "Self-consistent theory of superconducting mesoscopic weak links," *Phys. Rev. B*, vol. 51, pp. 3743–3753, 1995.

[193] Zhitenev, N. B., Meng, H., and Bao, Z., "Conductance of small molecular junctions," *Phys. Rev. Lett.*, vol. 88, p. 226801, 2002.

[194] Zoon, P. D., "Single Molecule Spectroscopy with Confocal Microscopy," *Universiteit van Amsterdam*, 2002.

VITA

Brooks Howard was born in Dallas Tx. September 7, 1977. He began undergraduate studies at Morehouse College in 1995. He received a B.S. in mathematics and chemistry in 2000. In 2001 he entered graduate school at The Georgia School of Technology in physics. Currently, Mr. Howard is teaching undergraduate physics at Morehouse College.